New Platforms for Terahertz Silicon Waveguides and Their Application in Absorption Spectroscopy

by

Hadi Amarloo

A thesis
presented to the University of Waterloo
in fulfillment of the
thesis requirement for the degree of
Doctor of Philosophy
in
Electrical and Computer Engineering

Waterloo, Ontario, Canada, 2018

Examining Committee Membership

The following served on the Examining Committee for this thesis. The decision of the Examining Committee is by majority vote.

External Examiner	Goutam Chattopadhyay Professor
Supervisor	Safieddin Safavi-Naeini Professor
Internal Member	Simarjeet Saini Professor
Internal Member	Amir Hamed Majedi Professor
Internal-external Member	James Martin Professor

I hereby declare that I am the sole author of this thesis. This is a true copy of the thesis, including any required final revisions, as accepted by my examiners.

I understand that my thesis may be made electronically available to the public.

Abstract

Waveguides—components which convey electromagnetic waves between points—are essential building blocks within miniaturized systems for all ranges of frequency and applications, including those in the Terahertz (THz) frequency gap. Although metallic THz waveguides have been available since a few decades ago and have been used extensively for THz applications, dielectric waveguides appear to be a more promising choice for THz systems that need to be low cost and compact. Silicon-on-Glass (SOG) technology, a relatively recent concept, has demonstrated remarkable performance for frequencies up to 1 THz. In this thesis, two new THz dielectric waveguide structures are proposed and investigated theoretically and experimentally: 1) a THz line–defect photonic crystal waveguide based on SOG technology, and 2) a structure which uses benzocyclobutene (BCB) to create a Silicon-BCB-Quartz (SBQ) platform. Such THz dielectric waveguide structures could form the fundamental building blocks for numerous different THz systems. In this thesis research, the application of these waveguide structures for waveguide-based THz absorption spectroscopy is studied and investigated experimentally.

The proposed THz line–defect photonic crystal waveguide advances the state of the SOG technology. Pyrex is the waveguide substrate within this technology. Due to its high material loss when operating in the THz frequency range, pyrex is etched underneath the guiding channel to minimize waveguide loss. However, handling the guiding channel over the etched pyrex is quite challenging. The first advantage of the proposed THz line–defect photonic crystal waveguide is that the photonic crystal structure provides a mechanically stable platform for handling the guiding channel over the etched pyrex. Secondly, the photonic crystal structure provides a suspended platform to integrate other components, such as resonators or couplers, with the waveguide over the etched pyrex substrate. Moreover, the slow wave characteristics of this waveguide could be advantageous for sensing applications at THz frequencies.

The SBQ structure is proposed as an easy-to-fabricate and efficient platform for THz compact systems. Due to the low loss characteristics of quartz at THz frequencies, etching the substrate is not required for the SBQ platform. Therefore, the quartz substrate provides a solid substrate not only for the silicon guiding channel, but also potentially for other components besides the waveguide. The fabrication and experimental characterization of the proposed waveguide are presented. Based on measurement results, this waveguide structure achieved an average attenuation constant as low as 0.026 $\frac{\text{dB}}{\text{mm}}$ over 500 to 580 GHz, among the lowest reported value for THz waveguides in the literature so far.

Two THz slot waveguides with highly confined fields are proposed: SBQ THz slot waveguide and THz plasmonic slot waveguide based on doped-GaAs. In sensing appli-

cations, these waveguide structures could enhance the interaction between the waveguide mode and the sample. The proposed SBQ THz slot waveguide is designed, fabricated, and investigated experimentally. The THz plasmonic waveguide is designed and characterized theoretically.

Despite the fact that free space setups are widely used for spectroscopy of different materials at THz frequencies, waveguide-based spectroscopy could provide a miniaturized setup for material characterization and sensing at this frequency band. To date, various metallic waveguides have been used for this purpose at the THz range. However, this thesis proposes the use of THz dielectric waveguides for absorption spectroscopy applications. The compatibility of the dielectric waveguide structures with available solid-state THz sources, in addition to the advanced fabrication facilities available for silicon based devices, open a pathway toward highly-miniaturized and low-cost THz spectroscopy systems. The performance of the proposed SBQ platform for waveguide-based THz absorption spectroscopy is studied experimentally using an exemplar test sample (lactose powder).

Acknowledgements

I would like to express my deepest gratitude to my supervisor, Professor Safieddin Safavi-Naeini, for his supervision and support during my PhD studies. During the course of this research, he supported me in many ways and provided me with great opportunities.

My sincere thanks to Professor Goutam Chattopadhyay who attended my defence session as the external examiner. I express my acknowledgement to my internal committee members, Professor James Martin, Professor Simarjeet Saini, and Professor Amir Hamed Majedi for their helpful comments and suggestions.

I specially thank Dr. Milad Khoshnegar and Dr. Nazy Ranjkesh whose experience in fabrication techniques helped me significantly. I express my acknowledgement to Dr. Nathan Nelson-Fitzpatrick and Brian Goddard from Quantum NanoFab Centre at the University of Waterloo, and Harlan Kuntz and Dr. Edward Huaping Xu from Nano Fabrication Centre at the University of Toronto for their help during fabrication steps of my PhD research.

Many thanks to all of my colleagues at the Centre for Intelligent Antenna and Radio Systems (CIARS), who provided me with such a motivating and friendly research environment. Special thanks to Dr. Mohsen Raeis-Zadeh, Dr. Behrooz Semnani, Dr. Naeimeh Ghafarian, Dr. Aidin Taeb, Dr. Mohammad-Reza Nezhad-Ahmadi, Dr. George Shaker, and Dr. Arash Rohani for their collaborations, fruitful discussions, and support.

I would like to express my heartfelt appreciations to my family for their endless love and support.

Dedication

To my parents

To my family

Table of Contents

List of Tables

List of Figures

Chapter 1

Introduction

The terahertz (THz) gap is a part of the electromagnetic spectrum existing between the microwave and infrared ranges of frequency. Although there are no unique frequency limits for the THz gap, it commonly refers to the 300 GHz to 3 THz range of frequencies, as shown in Fig. 1.1. The number of applications that utilize this range of frequencies is growing rapidly, and includes information and communications technology (ICT), biology and medical sciences, non-destructive evaluation, homeland security, quality control of food and agricultural products, global environmental monitoring, and ultrafast computing [1].

Although there has been ongoing research in the field for decades, THz technolgy has garnered special attention since 1990; the reason may be due to the fact that a reliable source of picosecond THz pulses was demonstrated in the late 1980s [2]. The THz gap is an undeveloped frequency range compared to other ranges of the electromagnetic spectrum. This is mainly due to technology challenges in this frequency range associated with high-power sources, low-loss passive components, and additional components required for THz systems. Many research groups have sought to overcome these difficulties in the past few decades, and have presented new applications for this frequency range.

Further details about THz technology are discussed below. In Section 1.1, an overview of the applications of this technology is presented. Since the focus of this thesis is THz waveguides, an overview of available waveguide technologies for this range of frequencies is presented in Section 1.2. A high power source of THz waves is a predominant challenge when working with this frequency range. An overview of THz sources is presented in Section 1.3. The motivation and objectives of this thesis are presented in Section 1.4. Finally, the structure of the remaining chapters of this thesis is described in Section 1.5.

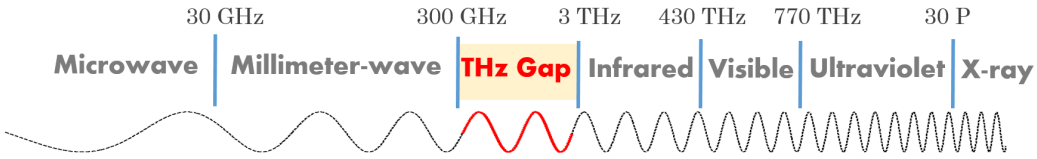

Figure 1.1: THz gap in the electromagnetic spectrum.

1.1 THz Technology Applications

The frequency of vibrational resonances of biological molecules usually falls within the THz gap [1]. The vibrational modes contain the intermolecular dynamics of stretch, bend and torsion between atoms. These resonances create specific "fingerprints" for the molecule. Exploring these resonances using THz waves provides information about the molecule's structure and is used for sensing applications. Common energetic explosives have unique spectral signatures in the THz gap [3–8]. These materials exhibit strong radiation absorption at some frequency bands within the THz gap; this makes it possible to differentiate them from typical covering materials such as clothing and plastic, which are almost transparent at THz frequencies. Molecules in their gas phase exhibit narrow absorption peaks due to rotational motions [9–13]. Each molecule shows these absorption peaks at unique frequencies. The rotational spectra is used to investigate molecular structures in different applications. This method is applied for environmental monitoring, atmospheric remote sensing, and analysis of the interstellar medium

The above mentioned molecules are just few examples from the many materials with significant signatures in the THz frequency range. Given these unique signatures, the THz gap is a rich range of frequencies that can be tapped for pharmaceutical, security, and drug test applications [1].

Many common packaging materials (i.e. paper, plastic, clothing) are opaque in the optical frequency range. However, THz radiation penetrates these materials. Therefore, THz imaging could be used for non-destructive inspection of a sealed package for security purposes [1].

In the THz gap, photon energy is low and non-ionizing; therefore, it would not be harmful to the human body. THz radiation is very sensitive to the water level, a critical measure of normalcy in biological systems [1]. In the field of THz imaging for medical applications, there have been significant advances in using such methods for the accurate detection of dental caries [14–16] and skin cancer [17–21].

There is an ever growing number of applications for the THz range of frequencies, and

the above mentioned applications are few exmaples. More details about the applications of the THz technology can be found in [1, 22].

1.2 THz Waveguide Technologies: An Overview

Emerging applications that take advantage of the THz frequency range have motivated many research groups to work on developing components required for THz systems. THz waveguides are among the main building blocks for many THz systems. The approaches taken to the development of waveguide structures proposed for use at the THz frequency range can be classified into two main groups:

1. Extension of metallic waveguide technologies developed for lower frequency ranges (microwave and millimeter wave; < 300 GHz) to higher frequencies (e.g. THz range; > 300 GHz). The challenges with such waveguide technology extensions are: a) Higher fabrication precision requirement, as the wavelength is orders of magnitude shorter in THz range compared to microwave and millimeter wave ranges, and b) Increase in waveguide loss at higher frequencies, as these technologies are based on metallic parts and the loss of metals increases at the THz frequencies.

2. Tailoring dielectric waveguide technologies developed for the higher frequency ranges (i.e. optical frequencies) for use at THz frequencies. Planar THz waveguides based on high-resistivity silicon (HR-Si) fall into this category. Although the operational principles of these THz waveguides are the same as those for optical waveguides, the waveguide stack-ups and fabrication processes are the unique challenges of these waveguide structures, especially at frequencies above 500 GHz.

1.2.1 THz Metallic Waveguides

Rectangular metallic waveguides are some of the most popular waveguides used for the microwave frequency range. In [23], metallic rectangular waveguides for frequencies up to 4 THz were studied. These waveguides suffer from high losses, around 1 $\frac{\text{dB}}{\text{mm}}$ when used below 1 THz.

Using of Deep Reactive Ion Etching (DRIE) on bulk silicon wafers and then metallization of surfaces using sputtering, constitute a fabrication method for THz metallic

waveguides which has been extensively studied in the literature [24–30]. This method offers high precision and high aspect ratio features in fabrication. In [24], this method was used to fabricate a THz waveguide for the 300 to 500 GHz frequency range which achieved average measured waveguide loss of 0.086 $\frac{\text{dB}}{\text{mm}}$. In the method presented in [24], which utilized DRIE on silicon, titanium was used as an adhesion layer followed by copper and gold as metallization, as shown in Fig. 1.2. The total metal thickness deposited was 7 μm. In [26], a silicon micro-machined waveguide operating at 500 to 750 GHz was presented, Fig. 1.3(a). The average measured loss for their waveguide was 0.15 $\frac{\text{dB}}{\text{mm}}$ at 600 GHz. A silicon micro-machined waveguide compoenent for 500 to 750 GHz was presented in [28]. They also presented a 3 dB hybrid coupler operating from 500 to 600 GHz, Fig. 1.3(b).

Coplanar transmission lines and microstrip transmission lines are among the planar microwave waveguides that also have been studied at THz frequencies [31, 32]. Parallel plate waveguides are metallic waveguides with very low group velocity dispersion, which have also been proposed for use at the THz frequency range [33,34]. A single metal wire is a simple type of metallic waveguide presented for use at the THz frequency range [35, 36]. This simple waveguide, shown with its characterization setup in Fig. 1.4, has very small dispersion and is low loss.

1.2.2 THz Dielectric Waveguides

Dielectric waveguides are commonly used at the optical range of frequencies. Although this type of waveguide was characterized theoretically for the THz frequency range several decades ago [37, 38], experimental studies were only reported more recently [39–42]. Due to its unique characteristics in the THz frequency range, high-resistivity silicon (HR-Si) is used for the guiding medium in these waveguides.

HR-Si is the most transparent and least dispersive dielectric in the THz frequency range [1]. The absorption coefficient of a high purity HR-Si crystal is less than 0.1 $\frac{1}{cm}$ below 3 THz), and variation of its refractive index is less than 10^{-4} in the same frequency range [1]. The effects of free carriers and lattice vibrations on other dielectrics and semiconductors are far greater than those of silicon. Moreover, silicon's mechanical and electrical properties are known in great detail. High purity silicon, produced using the flat zone crystal growth method, has a remarkably low carrier concentration, (less than 4×10^{11} $\frac{1}{\text{cm}^3}$ for n type) and high resistivity (larger than 10 $\text{k}\Omega - \text{cm}$) [1]. Fig. 1.5(a) shows the refractive index and the absorption coefficient of HR-Si over 0.5 to 4.5 THz [1]. The absorption of crystalline sapphire, crystalline quartz, fused silica, germanium, and gallium arsenide (GaAs) is higher than that of silicon, as shown in Fig. 1.5(b).

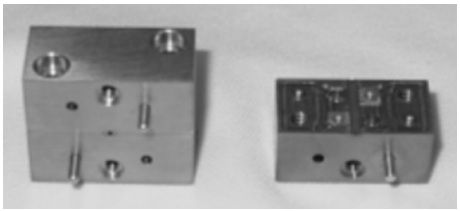

Figure 1.2: Photograph of metal holder block used to hold the silicon waveguide piece for measurement. Object at left is the full block assembled, and object at right is one half of the block, [24]

(a) (b)

Figure 1.3: (a) (left) Schematic drawing of silicon micromachined waveguide, and (right) photograph of completed chip, [26]. (b) (left) Bottom half of silicon micro-machined 3 dB waveguide hybrid coupler, (right) exploded view of the complete test package. [28].

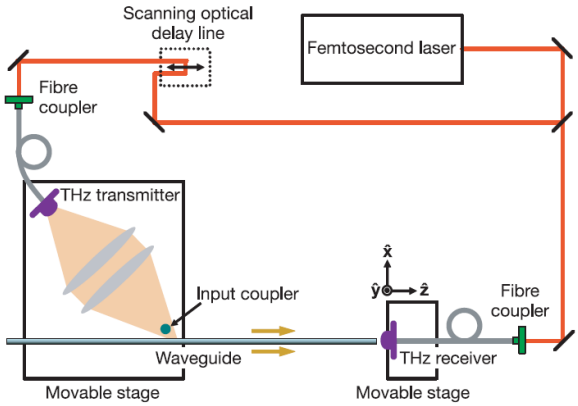

Figure 1.4: Diagram of optical setup for characterizing the propagating electromagnetic mode on a metal wire waveguide (stainless steel wire with diameter of 0.9 mm) [35].

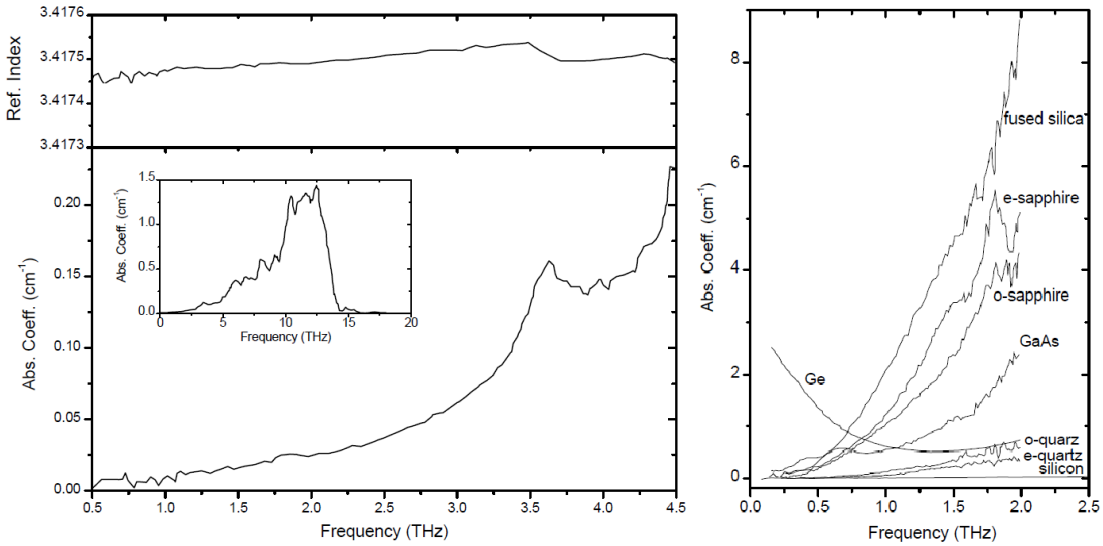

(a) (b)

Figure 1.5: (a) Refractive index and absorption coefficient of high-resistivity silicon [1], (b) Absorption coefficient of several materials at 0.2 to 2 THz frequency range [1].

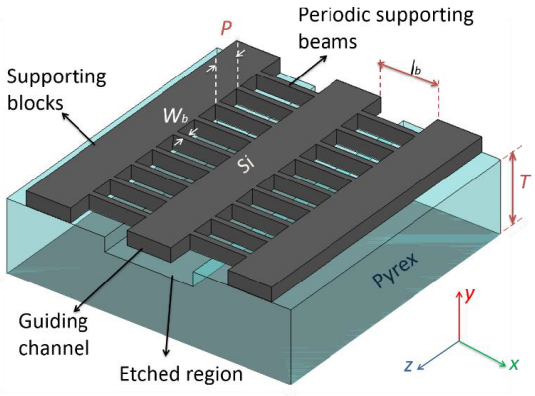

Figure 1.6: SOG waveguide structure [39, 43].

Although a suspended HR-Si waveguide has been experimentally investigated for 220 GHz [44], at THz frequencies, a substrate is mandatory to handle the thin HR-Si film. Silicon-on-glass (SOG) technology, proposed in [39, 43, 45], uses pyrex as the substrate for the HR-Si layer, Fig. 1.6. Anodic bonding, which is a fast bonding process, provides a

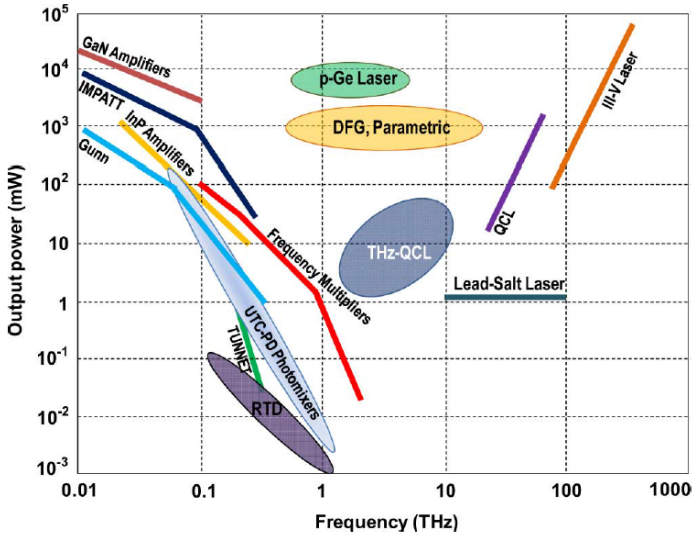

Figure 1.7: Output power of the THz sources as a function of frequency. Solid lines are conventional THz sources. For majority of the sources, the shown power is CW power at room temperature. Power for QCL and IIIV lasers are peak power. THz-QCL power is at cryogenic temperatures. IMPATT diode stands for impact ionization avalanche transit-time diode, MMIC stands for microwave monolithic integrated circuit, and TUNNET stands for tunnel injection transit time [49].

strong connection between the silicon and pyrex [46, 47]. Loss of the pyrex increases with frequency; especially for frequencies above 200 GHz [39, 48]. To reduce the loss of the SOG THz waveguide, etching of the pyrex underneath the guiding channel is proposed in [39]. As shown in Fig. 1.6, a periodic structure is used to support the guding channel over the etched pyrex. The average of loss of such a THz SOG dielectric waveguide over the 440 to 550 GHz frequency range is 0.054 $\frac{\text{dB}}{\text{mm}}$ [39].

1.3 THz Sources: An Overview

Different methods have been proposed and developed for THz generation in the past few decades. These methods can be categorized into three main groups: (1) optical THz generation, (2) THz quantum cascade laser (THZ-QCL), and (3) solid state sources. Fig. 1.7 summarizes the emission power versus frequency for several types of sources [22].

Optical generation of THz radiation is accomplished by generating a photocurrent in

a photoconductive semiconductor, or, through nonlinear optical effects such as difference-frequency generation (DFG). The main nonlinear media used for this application are GaAs and zinc telluride (ZnTe) [22].

In QCL sources, the THz radiation is generated by means of forced electron relaxation between subbands of quantum well due to population inversion. The first QCL source was developed in 1994, generating a frequency of 70 THz [50]. The frequency of a QCL source was reduced to 4.4 THz in 2002 [51] and a QLC with an emission frequency in the THz gap (1.39 and 2.3 THz) was presented in 2006 [52]. The research into this type of THz source is ongoing, with efforts geared towards reducing the lasing frequency and increasing the operational temperature [22].

THz solid state sources use a chain of multipliers to up-convert the generated signal to the THz range. Sources capable of generating frequencies as high as 1500 GHz are available [53]. To achieve this, four cascaded Schottky-barrier varactor doublers are used. The multiplier chain is driven by monolithic-microwave integrated-circuit-based high electron mobility transistor power amplifiers around 95 GHz [53].

1.4 Motivation and Objectives

Although there have been significant advancements made toward realizing the discrete components necessary for THz systems, a technology platform is required onto which all components of a miniaturized THz system could be integrated. THz dielectric waveguides using HR-Si provides highly promising low-loss transmission structures that have been investigated mainly over the lower frequencies of the THz gap. For frequencies above 500 GHz, a dielectric waveguide structure with a proper substrate is a challenge.

SOG technology proposes using pyrex as the substrate. Etching the pyrex substrate underneath the guiding HR-Si channel is required to avoid high material loss at THz frequencies. Although a periodic structure has been proposed to handle the guiding channel over the etched region of the pyrex, a stable handling structure which allows for the integration of other components besides the guiding channel remains a challenge for SOG technology.

A waveguide structure in which etching the substrate is not required would have multiple advantages over the SOG technology. Firstly, the challenge of handling the guiding channel over the substrate would be removed. Secondly, the fabrication process would be easier. Finally, the waveguide substrate will provide a platform for any other potential components to be integrated with the waveguide.

Field confinement for enhanced interaction between a waveguide mode and a material in the proximity of the waveguide is demanded over these frequency ranges. The concept of slot dielectric waveguide has been investigated extensively in the optical frequency range, but not at the THz range of frequencies. Growing sensing and spectroscopy applications of the THz technology require realization of the same waveguide concept for THz frequencies.

THz absorption spectroscopy is one of the unique applications of THz technology. Although free space setup has been used extensively for this purpose, it is a bulky approach which requires a high amount of the material sample in order to achieve measurable interaction between the material and THz signal. Waveguide-based absorption spectroscopy is a promising alternative method, which not only reduces the required amount of sample drastically compared to the free space method, but also opens the pathway towards a miniaturized and integrated spectroscopy device.

Objectives of this Thesis

- Develop a new THz waveguide structure based on SOG technology which can provide a mechanically stable platform for integrating passive components with the waveguide over the etched substrate.
- Develop an efficient and easy-to-fabricate dielectric platform for the miniaturized integrated THz systems, with no requirement for etching the substrate.
- Investigate THz field localization using the concept of slot waveguide, including experimental characterization.
- Experimental investigation of THz on-chip absorption spectroscopy based on the developed dielectric platform.

1.5 Structure of the Thesis

In Chapter 2, a THz line-defect waveguide based on SOG technology is proposed, and simulation results for the 500 to 700 GHz frequency range are presented. The steps taken to fabricate the waveguide are presented. The measurement results of two fabricated THz line-defect waveguides with different lengths are discussed. Waveguide characteristics are extracted from the measurement results. The fabricated waveguide performance is compared with other THz waveguides reported in the literature.

In Chapter 3, a Silicon-BCB-Quartz (SBQ) structure, as an efficient and easy-to-fabricate platform for THz systems, is proposed. A channel waveguide based on this platform is designed for the 500 to 580 GHz frequency range, and simulation results are presented. Fabrication steps are discussed. Several bonding recipes, which were performed experimentally, are presented and compared. Two waveguides with different lengths are fabricated and measured. Waveguide characteristics are extracted from the measurement results.

In Chapter 4, two THz slot waveguides are proposed and investigated. In Section 4.1, an SBQ THz slot waveguide is presented, designed, and investigated experimentally. In Section 4.2, a THz slot plasmonic waveguide is proposed and investigated theoretically.

In Chapter 5, the application of the proposed SBQ THz dielectric waveguide for THz absorption spectroscopy is proposed and investigated experimentally. First, in Section 5.1, an overview of the available THz spectroscopy methods is presented. Then, in Section 5.2, results of free space absorption spectroscopy of test sample (lactose powder mixed with polyethylene powder) are presented. A new method for extracting the absorption of the material under test is proposed, and verified via full-wave simulations. Next, in Section 5.3, the results of the design and fabrication of the several waveguides based on the SBQ platform are presented and the results of the waveguide-based absorption spectroscopy using these waveguides are discussed (the fabricated waveguides are: SBQ channel waveguide, SBQ narrowed channel waveguide, and SBQ spiral long waveguide). Conclusions of this chapter is presented in Section 5.4.

In Chapter 6, a summary of the contributions of this thesis, the conclusions, and the recommendations for future work are presented.

Chapter 2

Terahertz Line–Defect Waveguide Based on Silicon-on-Glass Technology

In this chapter a new THz waveguide based on photonic crystal line–defect concept, implemented in Silicon-on-Glass (SOG) technology, is proposed. The basic configuration is shown in Fig. 2.1. The periodic structure around the guiding channel provides field confinement in the guiding channel over the bandgap frequencies, in xy plane [54, 55]. Total internal reflection at the HR–Si and air interface makes the field confined in the vertical direction, $\hat{z}$. The waveguide has pyrex as the substrate, which makes it a practical waveguide platform and scalable to higher frequencies. The pyrex substrate is etched underneath the guiding channel to reduce the waveguide loss due to the pyrex material loss.

In the proposed waveguide structure, the suspended photonic crystal structure provides a platform for integrating other components, such as resonators or couplers, with the waveguide. In contrast, in the available SOG waveguide (shown in Fig. 1.6) integration of other components with the waveguide is quite challenging because of the specific handling structure. Moreover, in the proposed structure in this chapter, only one-third of the area of the photonic crystal in xy plane is air; therefore, it offers a mechanically stable structure.

The proposed structure is designed for 500 to 700 GHz frequency range, as presented in Section 2.1. The fabrication procedure is presented in Section 2.2. Measurement setup and measurement results are presented and discussed in Section 2.3. Conclusions of this chapter is presented in Section 2.4.

It should be mentioned that some of the results presented in this chapter have been published in [42].

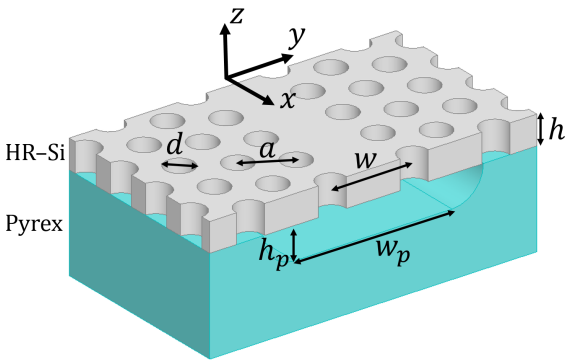

Figure 2.1: Proposed THz line–defect waveguide based on SOG technology. Pyrex underneath the guiding channel is etched to reduce the waveguide loss.

2.1 Design and Simulation

Design of line–defect waveguide starts with designing the photonic crystal structure with bandgap at the desired frequency range. Fig. 2.2(a) shows the photonic crystal structure, which is an array of holes in a silicon slab. Suppose $\hat{z}$ is the direction normal to the slab, the modes of this structure can be classified to TE_z (in which E_x, E_y and H_z are the dominant field components) and TM_z (in which H_x, H_y, and E_z are the dominant field components) [54]. This type of photonic crystal structure provides bandgap for TE_z modes [54]. The TE_z mode of the line–defect waveguide has E_x, E_y and H_z as the dominant field components. By proper excitation, TE_z mode of the line–defect waveguide can be excited, which will not couple to the TM_z modes of the photonic crystal structure due to field mismatch. Therefore, a TE_z bandgap is sufficient to confine this mode of the waveguide inside the guiding channel.

2.1.1 Bandgap Structure Design

It has been shown in [54] that a photonic crystal slab with dimensional ratios of $h = d = 0.6a$ (a is the lattice constant) provides TE_z bandgap for the normalized frequency range of $\frac{\omega a}{2\pi c} = 0.25$ to 0.33. Also, it has been shown in [56–58] that the radiation losses of the leaky modes of a line–defect photonic crystal waveguide reduces by increasing the thickness of the slab (h) and reducing the diameter of the holes (d). Based on these considerations, the dimensions chosen for the THz photonic crystal slab were $a = 150$ μm, $h = 100$ μm, and $d = 90$ μm, to have TE_z bandgap over the desired frequency range. In the proposed line–

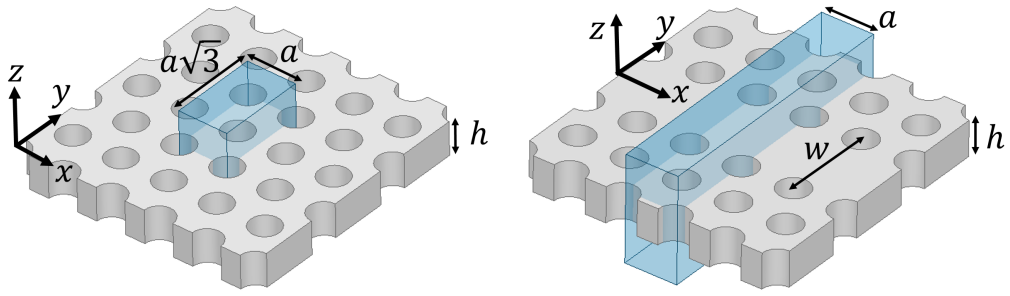

(a) (b)

Figure 2.2: (a) THz photonic crystal slab, which is an array of holes with triangular lattice in a thin silicon film. The box shows the unit cell of the structure. (b) Unit cell of the defected structure.

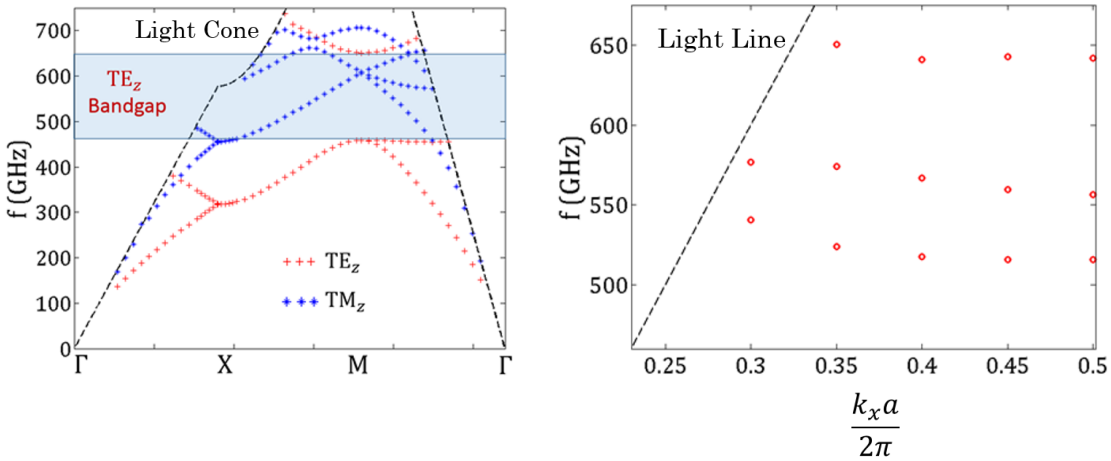

(a) (b)

Figure 2.3: (a) Band diagram of the THz photonic crystal structure shown in Fig. 2.2(a). (b) Dispersion diagrams of the TE_z modes of the line–defect structure shown in Fig. 2.2(b).

defect waveguide structure, pyrex is etched underneath the HR-Si several unit cells away from the guiding channel; therefore, pyrex will not contribute to the characteristics of the photonic crystal structure. For simulation simplicity, pyrex substrate was not included in the bandgap calculations. A simulation was performed using the Finite Element numerical method (FEM) in ANSYS High Frequency Structure Simulator (HFSS) to analyze the structure. The smallest unit cell of the photonic crystal structure shown in Fig. 2.2(a) is a parallelogram with dimension of a by a. For the sake of simulation simplicity, a unit cell

with dimension of a by $a\sqrt{3}$, which has rectangular corners, was considered, as shown by a box in Fig. 2.2(a).

Figure 2.3(a) shows the simulation results for the TM_z and TE_z modes of the photonic crystal structure. As shown, there is a bandgap for TE_z modes from 460 GHz up to 650 GHz, which includes the desired frequency range. Fig. 2.3(b) shows the guided TE_z modes of the defected structure. Fig. 2.4 shows the vector plots of the electric and magnetic fields of the TE_z modes. In these plots two unit cells along the x-direction are included to provide a better visualization.

It should be added that the presented results were verified through simulations performed using Finite Difference Time Domain numerical method (FDTD) in Lumerical simulator.

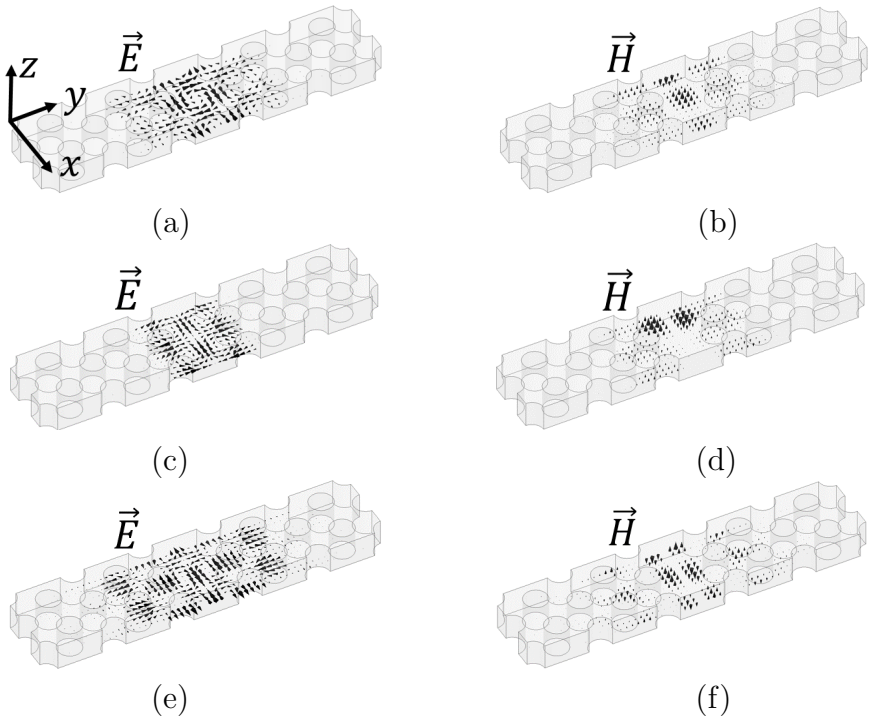

Figure 2.4: Field distributions of the three TE_z modes of the line–defect photonic crystal; first mode (a) and (b), second mode (c) and (d), and third mode (e) and (f).

2.1.2 THz Line–Defect Waveguide Based on the SOG Platform

Line–defect waveguide, as shown in Fig. 2.1, is a slab photonic crystal structure in which one row of holes is removed in x-direction (waveguide width $w = a\sqrt{3}$). HR-Si is modeled as a dielectric with permittivity of 11.69 [1]. Conductivity of HR-Si depends on many factors, including its resistivity value. Table 2.1 summarizes the measured conductivity of HR-Si for few resistivity values presented in [59–61]. In the fabrication step of this work, HR-Si with resistivity of 5 $k\Omega - cm$ is used. Since we were not able to find experimental data for HR-Si conductivity for this resistivity value over the range of frequency of interest, in simulations two different values for the conductivity of HR-Si are considered, $\sigma_1 = 0.01$ $\frac{S}{m}$ and $\sigma_2 = 0.42$ $\frac{S}{m}$, which are the lowest and highest values presented in the Table 2.1.

The waveguide has pyrex as the substrate. Fig. 2.5 shows the conductivity of pyrex versus frequency (extracted from measurement results presented in [48]). To decrease the waveguide loss, pyrex is etched underneath the guiding channel, with depth of $h = 100$ μm and width of $w = 1.5$ mm.

Table 2.1: Conductivities of HR-Si

Silicon Resistivity	Frequency Range	Conductivity
10 $k\Omega - cm$ [59]	up to 1 THz	0.01 ($\frac{S}{m}$)
8 $k\Omega - cm$ [60]	up to 400 GHz	0.12 ($\frac{S}{m}$)
HR-Si [61] (Resistivity value is not provided.)	500 to 750 GHz	0.13 to 0.42 ($\frac{S}{m}$)

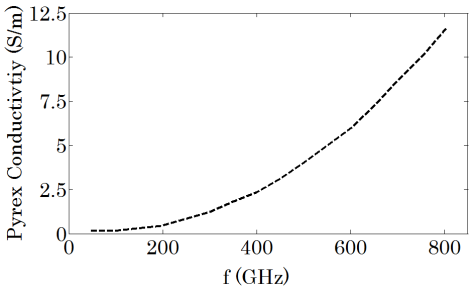

Figure 2.5: Pyrex conductivity at the THz frequencies (extracted from [48]).

To characterize the line–defect waveguide, a back-to-back structure, shown in Fig. 2.6, is considered. As was shown in Fig. 2.4, the dominant mode of the line–defect waveguide matches with the dominant mode of a channel dielectric waveguide; therefore, tapered channel waveguides were used as the transitions between the rectangular metallic waveguides ($WR_{1.5}$) and the line–defect waveguide (length of each taper was $L_t = 0.75$ mm). To match the first mode of the $WR_{1.5}$ waveguides (TE_{10}) to the first mode of the channel waveguides, the longer side of the $WR_{1.5}$ cross section should be along z-direction, as shown in Fig. 2.6 (cross section dimensions of $WR_{1.5}$ are $a_{WR} = 0.381$ mm by $b_{WR} = 0.191$ mm, and its TE_{10} mode cutoff is at 393 GHz).

In order to extract the line–defect waveguide characteristics, the back-to-back structure is simulated for two different lengths of the line–defect waveguide, $L_1^s = 3$ mm and $L_2^s = 3.75$ mm. Fig. 2.7(a) shows the scattering parameters of the back-to-back structure, for both lengths of L_1^s and L_2^s, for conductivity of σ_2 assumed for HR-Si. The average transmission over 540 to 630 GHz frequency range is -1.9 dB for L_1^s and is -2.2 dB for L_2^s. Fig. 2.7(b) shows the magnitude of electric field through the back-to-back structure, at three frequencies, before, inside and after the passband.

Attenuation constant of the line–defect waveguide can be extracted from the scattering parameters of the back-to-back structure with two different lengths of the line–defect waveguide. For this purpose, the method used in [62] is considered. This method will be presented in Section 2.3.1. Fig. 2.8 shows the attenuation constant of the line–defect waveguide versus frequency, for both HR-Si conductivities, σ_1 and σ_2. For σ_1, the attenuation constant varies between 0.10 $\frac{\text{dB}}{\text{mm}}$ and 0.3 $\frac{\text{dB}}{\text{mm}}$ over 540 to 630 GHz frequency range with average of 0.16 $\frac{\text{dB}}{\text{mm}}$. For σ_2, the attenuation constant varies between 0.33 $\frac{\text{dB}}{\text{mm}}$ and 0.52 $\frac{\text{dB}}{\text{mm}}$ over the same frequency range with average of 0.39 $\frac{\text{dB}}{\text{mm}}$.

Although increasing the dimensions of the pyrex etched region will decrease the waveguide loss, it increases the waveguide fragility; therefore, pyrex should be etched as much as it has significant effect on the waveguide loss reduction. The dimensions of the pyrex etch, h_p and w_p, are swept to study their effects on the waveguide attenuation constant. Fig. 2.9 shows the results. As shown, without etching pyrex the waveguide loss will be more than 2 $\frac{\text{dB}}{\text{mm}}$ at some frequencies. The attenuation constant decreases with increasing the etching dimensions, but it does not change significantly when increasing etching depth from 100 μm to 150 μm and etching width from 1.5 mm to 2 mm.

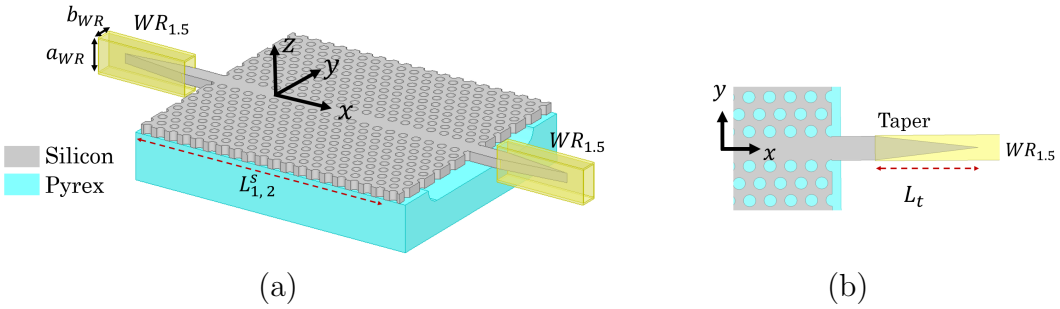

(a) (b)

Figure 2.6: (a) THz line–defect waveguide excited by $WR_{1.5}$ waveguide, in a back-to-back structure, (b) Tapered channel waveguide as a transition from rectangular waveguide to the THz line–defect waveguide.

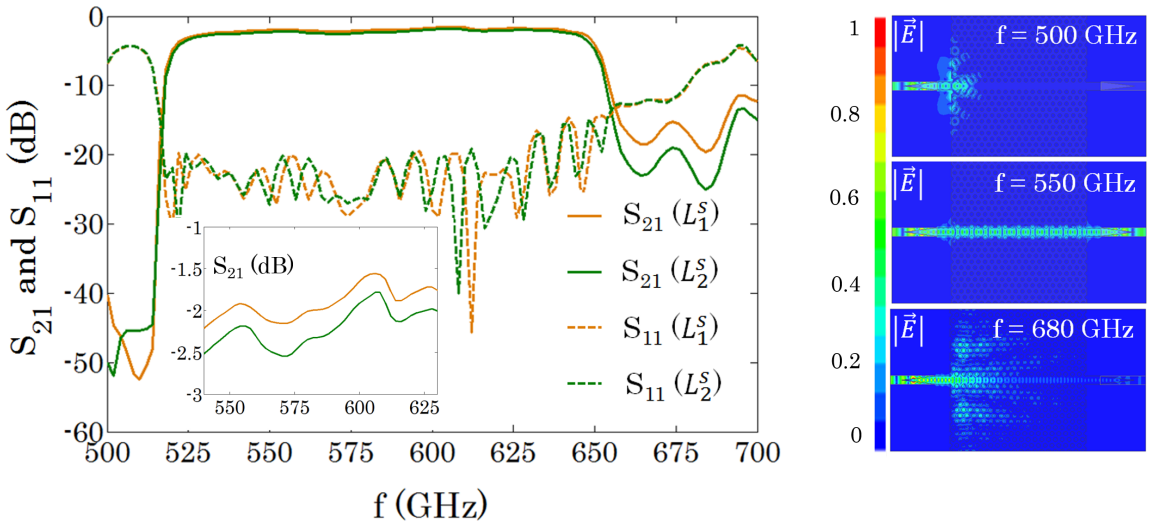

(a) (b)

Figure 2.7: (a) Simulation results for S_{21} and S_{11} of the back-to-back structure for two different waveguide lengths. Inset shows the zoom in of S_{21}over 540 to 630 GHz frequency range. (b) Transmission through the back-to-back structure shown in Fig. 2.6, at three frequencies: before (500 GHz), inside (550 GHz), and after (680 GHz) the transmission band of the THz line–defect waveguide.

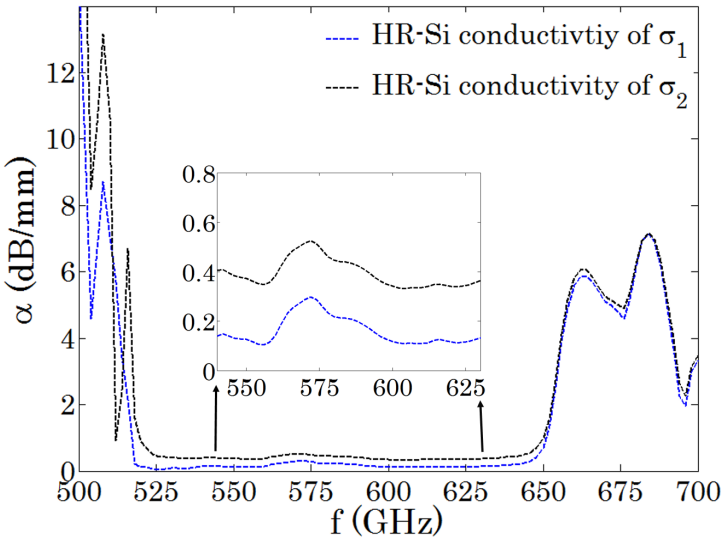

Figure 2.8: Attenuation constant of the proposed THz line–defect waveguide. Inset shows the zoom in over 540 to 630 GHz frequency range.

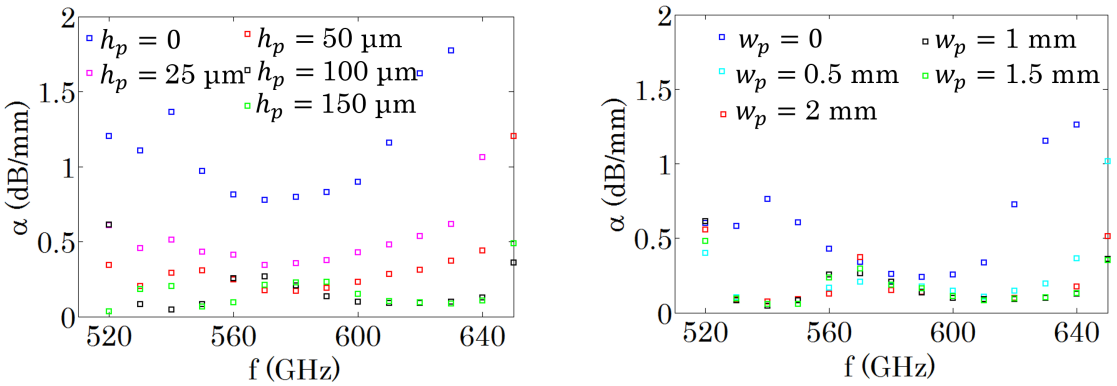

Figure 2.9: Attenuation constant of the proposed THz line–defect waveguide for different dimensions of the etched pyrex region; depth (a), and width (b). These simulations were performed with $\sigma_1 = 0.01 \frac{\text{S}}{\text{m}}$ assumed for HR-Si.

2.2 Fabrication

The fabrication procedure for the line–defect waveguide can be divided into three main steps: etching the pyrex, bonding the silicon to the pyrex, and etching the silicon.

2.2.1 Pyrex Wet Etching

The etching of the pyrex was performed using a wet-etching process in hydrofluoric acid (HF;49%) over a chromium/gold hard mask. The steps are shown schematically in Fig. 2.10.

The process started with cleaning the pyrex pieces. A solution of NH_4OH, H_2O_2, and H_2O at 75 °C was used for the cleaning. Fig. 2.10(b) shows the chromium/gold (Cr/Au : 50/500 nm) deposited on the pyrex. Since the Au layer acts as the mask for the HF wet etching, any cracks in this metal should be avoided. In order to achieve a better hard mask, the Au deposition was divided into three steps (500 nm: 200 nm, 150 nm, 150 nm), with a 10 min cooling down period between steps.

A thick photoresist (AZ P4620; 11 μm) was spin coated on the deposited metal layers [Fig. 2.10(c)] and an optical lithography process was then used to pattern the photoresist [Fig. 2.10(d)]. Next, the Cr/Au was patterned using standard etchant for these metals (wet etching process), Fig. 2.10(e). The backside of the pyrex pieces needed to be protected from etching in HF, therefore Cr/Au 30/250 nm was also deposited on the back side of the pyrex, Fig. 2.10(f) (the waveguides would be diced at the end of the fabrication process, so protecting the side walls of pyrex is not mandatory). The etch rate of pyrex in HF acid is around 6 to 8 $\frac{\mu m}{min}$ (measured $\sim$ 6.6 $\frac{\mu m}{min}$). The pyrex pieces were left in the HF acid for 15 min, resulting in a 100 μm etched depth, Fig. 2.10(g). After etching the pyrex, the Cr/Au layers were removed with standard Au and Cr etchants, Fig. 2.10(h).

Figure 2.11(a) and (b) show images of the etched pyrex, before removing the Cr/Au and photoresist. It can be seen in Fig. 2.11(b) that the Cr/Au mask of the back side has been scratched by HF in some areas; this is due to the thin Au mask used for the backside (250 nm). Although these scratches could have been avoided by using a higher thickness of Au, they do not affect the device's performance.

2.2.2 Anodic Bonding

Anodic bonding is a wafer bonding process used to seal glass to silicon [46, 47, 63–65]. The bonding occurs through a high voltage ($>$ 600 V) applied to the wafers to be bonded, at

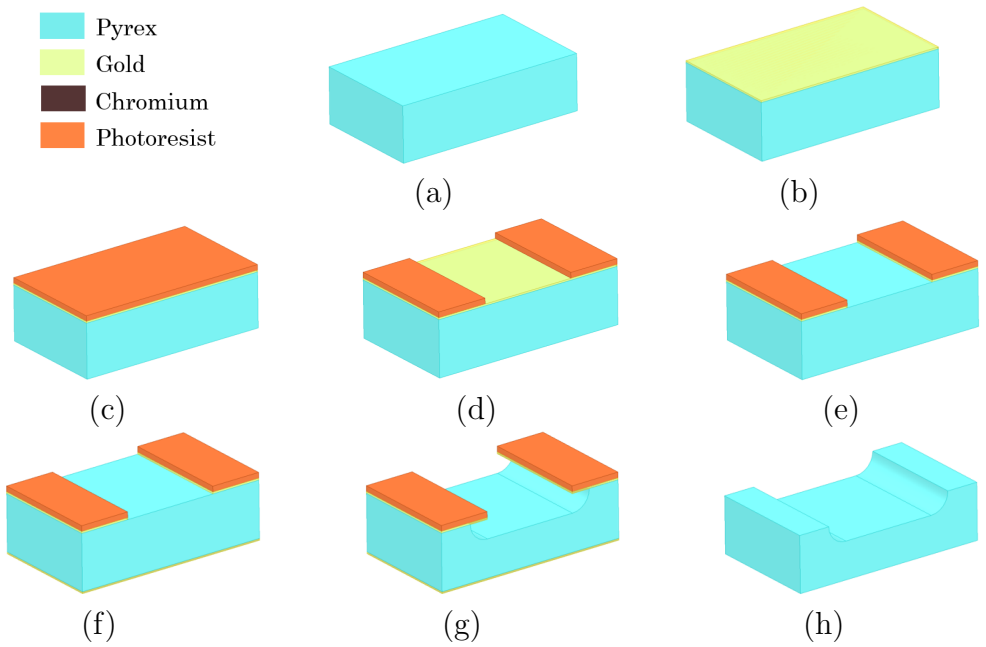

Figure 2.10: Pyrex etching steps: (a) pyrex piece cleaned, (b) Cr/Au mask deposited, (c) photoresist spin coated on Au film, (d) photoresist patterned through optical lithography, (e) Cr/Au mask patterned through wet etching, (f) Cr/Au mask deposited on backside of piece, (g) pyrex etched in HF, (h) Cr/Au masks removed through wet etching and photoresist removed in acetone.

Figure 2.11: (a) Etched pyrex, before removing the Cr/Au hard mask (photoresist is removed only in top-right piece). Each piece served as the substrate for two waveguides. (b) Backside of the etched pyrex pieces.

a high temperature (300 °C to 500 °C). The sodium and oxygen ions in the pyrex become mobile at such high temperatures. These mobile ions travel toward the interface of the pyrex and silicon and form strong molecular bonds (Si – O) between the two wafers [63].

In the designed THz line–defect waveguide, the thickness of the silicon layer is only 100 μm—too thin to be handled without a handling layer. To address this, silicon-on-insulator (SOI) pieces were used which have a low-resistivity handling silicon layer (500 μm) separated from the high-resistivity layer by a thin film (2 μm) of silicon dioxide.

Before performing the anodic bonding process, the pyrex and SOI pieces were cleaned. This step is critical in order to achieve proper bonding. The anodic bonding was performed in wafer bonding equipment (AML AWB-04 Aligner Wafer Bonder) under a vacuum condition (pressure below 10^{-4} mbar) at a temperature of 400 °C. Although a voltage of 600 V is sufficient for bonding silicon and pyrex, the silicon-dioxide film in SOI pieces creates a capacitor in the multilayer structure, so a higher voltage (1 kV) needed to be used. The bonding process took less than 30 min to finish. After bonding, the handle silicon and silicon dioxide layers were removed.

2.2.3 Silicon Etching

Deep Reactive Ion Etching (DRIE) is a highly anisotropic etching process which can provide high aspect ratio features, with almost vertical side-walls in silicon. The Bosch process, used for THz line–defect waveguide fabrication, contains two alternating steps: 1) an isotropic plasma etch (plasma containing sulfur hexafluoride (SF_6) ions attack silicon almost vertically), then 2) deposition of a chemically inert passivation layer of Octafluorocyclobutane (C_4F8; protects the silicon from lateral etching).

The steps of the silicon etching are shown schematically in Fig. 2.12. First, the silicon, already bonded to the pyrex substrate, was spin coated with a thick photoresist [AZ P4620; 11 μm; Fig. 2.12 (b)]. The photoresist was then baked on a hotplate (115 °C for 90 seconds). Three hours was considered sufficient time for the rehydration of the photoresist. Then, the optical lithography process was used to pattern the photoresist with the waveguide structure, Fig. 2.12 (c). To align the waveguide pattern on the photoresist with the etched region of the pyrex, back-sight alignment was performed. The DRIE etching process was used to etch the silicon and map the waveguide structure onto the silicon layer, Fig. 2.12(d). Finally, the photoresist was removed in acetone, Fig. 2.12(e).

Figure 2.13 shows the optical microscope images of the patterned photoresist and Fig. 2.14 shows the optical microscope images of the final device. This figure shows a zoomed view of two holes of the structure. The diameters of the holes are very close to the target

value ($d = 90\ \mu$m). It should be mentioned that the accuracy of the fabrication is limited by the optical lithography process, which has an accuracy of $\sim 1\ \mu$m. This level of accuracy is sufficient for the frequency range of interest in this research. Fig. 2.15(a) shows the scanning electron microscope images of the fabricated device. Etched pyrex can be seen underneath the guiding channel. Fig. 2.15(b) shows a few holes of the periodic structure.

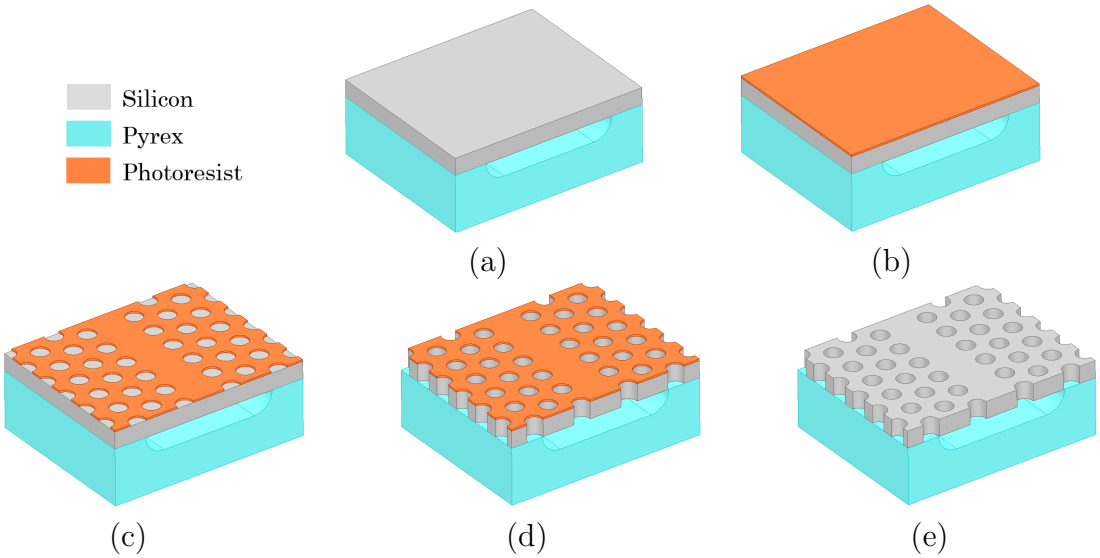

Figure 2.12: Silicon etching steps: (a) silicon bonded to the pyrex substrate, (b) silicon coated with photoresist, (c) photoresist patterned through optical lithography, (d) silicon etched through DRIE, (e) photoresist removed.

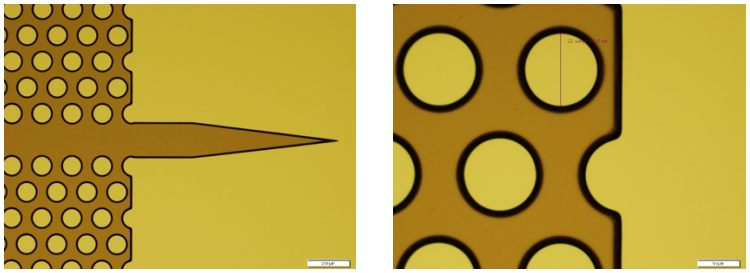

Figure 2.13: (a) Optical microscope images of the patterned photoresist; (b) zoom in of a few holes of the pattern.

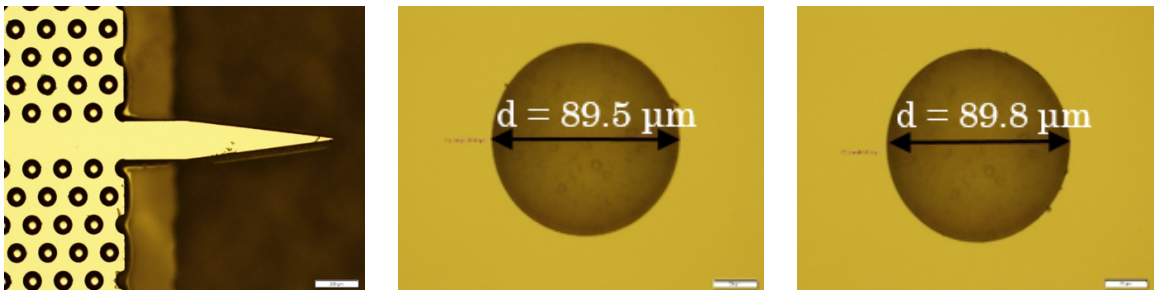

(a) (b) (c)

Figure 2.14: Optical microscope images of the fabricated THz line–defect waveguide. (a) THz line–defect waveguide and tapered channel waveguide; (b) and (c) zoom in of two holes of the photonic crystal structure.

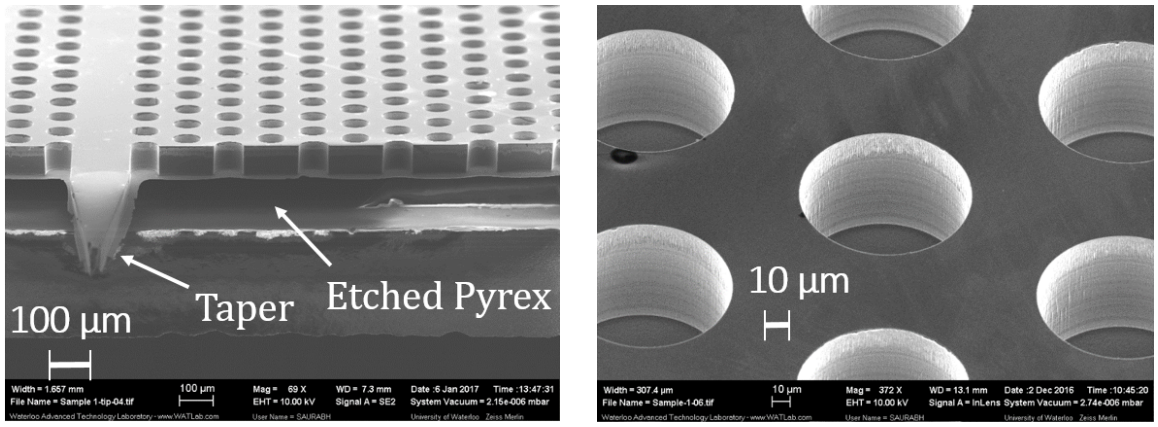

(a) (b)

Figure 2.15: Scanning electron microscope images of the fabricated THz line–defect waveguide. (a) THz line–defect waveguide and tapered channel waveguide; (b) zoom in of a few holes of the photonic crystal structure.

2.3 Measurement

Figure 2.16 shows the components of measurement setup. A Network Analyzer (Agilent PNA-X) connected to the frequency extender modules (from Virginia Diodes Inc) are used as the source and detector in the setup, Fig. 2.16(a). The frequency extender modules have rectangular waveguides, $WR_{1.5}$, at their outputs. As a stage for line–defect waveguide, several metallic stages with different lengths are fabricated using machining, Fig. 2.16(b) and (c). The stages are designed and fabricated such that the taper section of the line–defect waveguide will be in the middle of the $WR_{1.5}$ after installation. Fig. 2.17 shows the installed measurement setup. The frequency extender modules are located on micropositioners for alignment and safe insertion of tapers into $WR_{1.5}$ waveguides. The metallic stage is connected between two $WR_{1.5}$ as a holder for line–defect waveguide. Using this measurement setup all complex components of the scattering matrix can be measured, and it is among the most accurate methods for waveguide characterization.

Proposed THz line–defect waveguide was fabricated and measured with two different lengths, $L_1^m = 9.3$ mm and $L_2^m = 19.8$ mm. Fig. 2.18 shows the measured S_{21} of both lengths. The average of S_{21} over the 540 to 630 GHz range is -5.4 dB for L_1^m and -9.9 dB for L_2^m. Simulated transmission band and the measured one can be quantitatively compared by examining plots in Fig. 2.7(a) and Fig. 2.18. If we define the cutoff frequencies as the frequencies wherein the transmission drops by 1 dB from its average value over 540 to 630 GHz frequency range, then simulated transmission band is 525.5 to 648 GHz and 526.5 to 647 GHz for short and long waveguides respectively, and the measured transmission band, based on same definition, is 523 to 631 GHz and 529 to 626 GHz for short and long waveguides respectively.

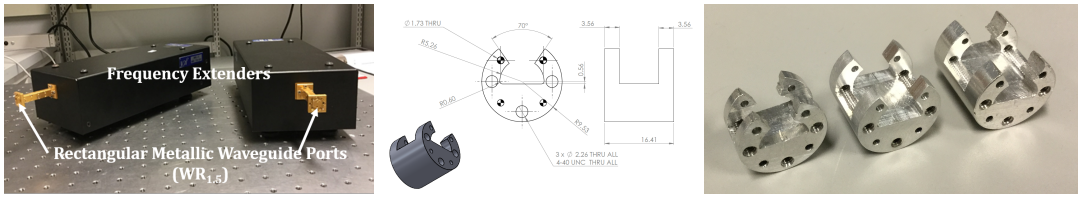

(a) (b) (c)

Figure 2.16: (a) Frequency extender modules. (b) and (c): Metallic stage (fabricated using machining).

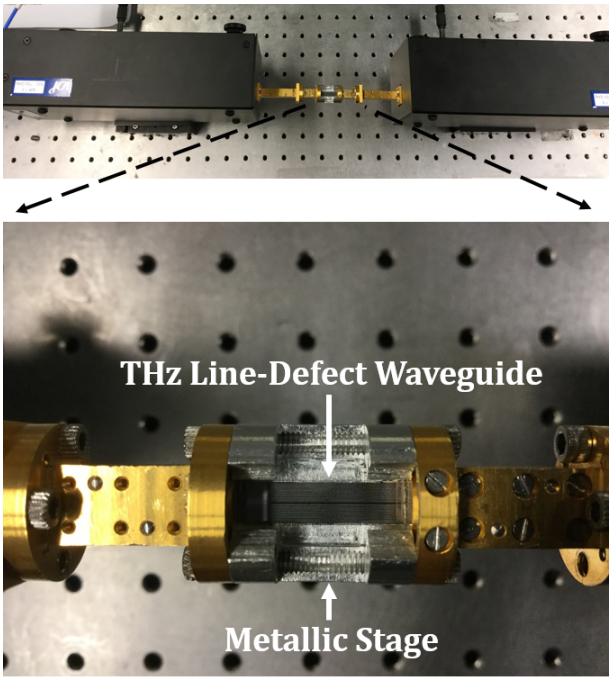

Figure 2.17: Measurement setup; frequency extender modules with $WR_{1.5}$ waveguide outputs are connected to the metallic stage. THz line–defect waveguide is on the metallic stage and its tapered channel waveguides are inserted into the rectangular waveguides.

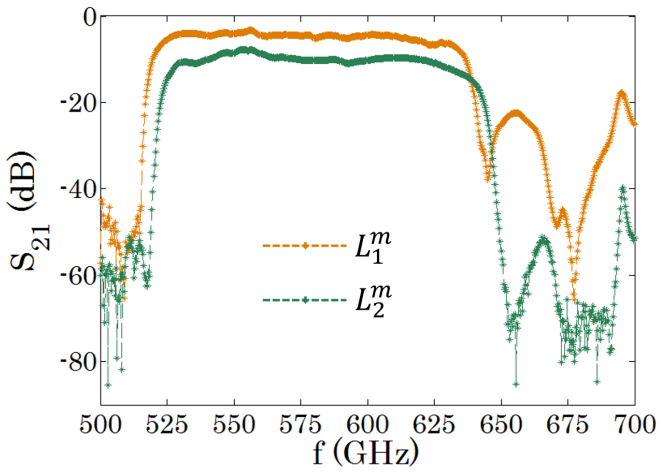

Figure 2.18: Measurement result for the transmission through the back-to-back structure, for two different waveguide lengths.

2.3.1 Extracting the Waveguide Attenuation Constant

Attenuation constant of the THz line–defect waveguide was extracted from the scattering parameters measured for two lengths of the waveguide using the method presented in [62]. Waveguide with lengths of $L_1 = 9.43$ mm and $L_2 = 19.9$ mm, were fabricated and their scattering parameters were measured using a Network Analyzer. Suppose the excitation sections, including the $WR_{1.5}$ waveguide and tapered HR-Si channel waveguide, have transmission matrices of $\mathbf{T_x}$ a and $\mathbf{T_y}$ on two ends. Considering the transmission matrices of the THz line–defect waveguides with lengths of L_1 and L_2 as $\mathbf{T_{L_1}}$ and $\mathbf{T_{L_2}}$, then the measured transmission matrices are:

$$\mathbf{T_1} = \mathbf{T_x}\mathbf{T_{L_1}}\mathbf{T_y} \tag{2.1}$$

$$\mathbf{T_2} = \mathbf{T_x}\mathbf{T_{L_2}}\mathbf{T_y} \tag{2.2}$$

Considering THz line–defect waveguides as single mode waveguides, then:

$$\mathbf{T_{L_1}} = \begin{bmatrix} e^{-\gamma L_1} & 0 \\ 0 & e^{\gamma L_1} \end{bmatrix} \tag{2.3}$$

$$\mathbf{T_{L_2}} = \begin{bmatrix} e^{-\gamma L_2} & 0 \\ 0 & e^{\gamma L_2} \end{bmatrix} \tag{2.4}$$

In which, γ is the complex propagation constant of the waveguides. Multiplying T_2 by the inverse of T_1:

$$\mathbf{T_2}\mathbf{T_1^{-1}} = \mathbf{T_x}\mathbf{T_{L_{21}}}\mathbf{T_x^{-1}} \tag{2.5}$$

in which:

$$\mathbf{T_{L_{21}}} = \begin{bmatrix} e^{-\gamma(L_2-L_1)} & 0 \\ 0 & e^{\gamma(L_2-L_1)} \end{bmatrix} \tag{2.6}$$

Eigenvalues of $\mathbf{T_2}\mathbf{T_1^{-1}}$ and $\mathbf{T_{L_{21}}}$ are the same, from which the complex propagation constant is derived.

Figure 2.19 shows the attenuation constants from simulations (σ_1 and σ_2) and measurement. The measured attenuation constant varies between 0.05 $\frac{\text{dB}}{\text{mm}}$ and 0.58 $\frac{\text{dB}}{\text{mm}}$ over 540 to 630 GHz, with an average of 0.40 $\frac{\text{dB}}{\text{mm}}$. In the next section, a simulation study on the expected tolerances in this parameter due to the misalignments in the measurement setup is presented.

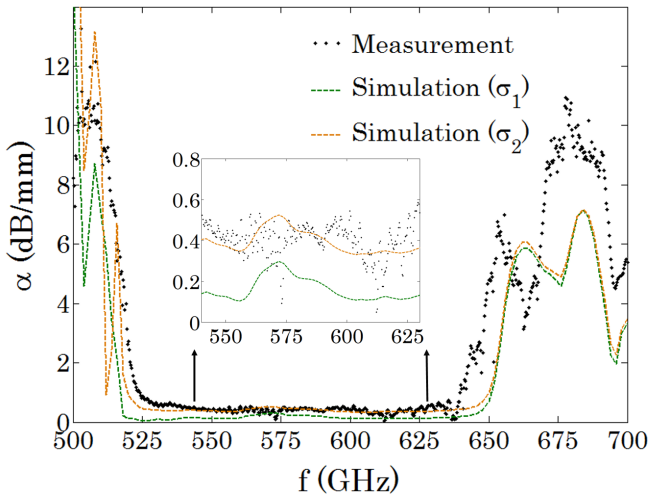

Figure 2.19: Attenuation constant of the THz line–defect waveguide, measurement and simulation results. Inset shows zoom in over 540 to 630 GHz.

2.3.2 Misalignment in the Measurement

In the presented waveguide loss extraction method, it was assumed that the transitions from $WR_{1.5}$ to the channel waveguide ($\mathbf{T_x}$), and from the channel waveguide to $WR_{1.5}$ ($\mathbf{T_y}$), are the same for short and long waveguides. However, different alignments of the tapered channel waveguides inside the $WR_{1.5}$ waveguides during measurement will result in different $\mathbf{T_x}$ and $\mathbf{T_y}$ for short and long waveguides. For instance, if the short waveguide is perfectly aligned but the long waveguide has some misalignments then the higher coupling loss between $WR_{1.5}$ and the channel waveguides in the long waveguide (due to misalignments) will result in an over-estimate in the waveguide loss. A study was performed using HFSS simulator, to provide an estimation of the amount of error that should be expected in the waveguide attenuation constant extracted from the measurements.

Figure 2.20(a) shows the simulated structure. The tapered channel waveguides on both ends are exactly the same as those used for line–defect waveguides; however, the line–defect waveguide is replaced by a free standing channel waveguide (with a length of L_0 = 5 mm, more than 8 λ_0; λ_0 is the free space wavelength). This replacement reduces the simulation time without affecting the results as long as the tapered sections are the same as before; same $\mathbf{T_x}$ and $\mathbf{T_y}$. First, the structure is simulated in an aligned setup (center of tapered channel waveguides are in the middle of the $WR_{1.5}$ waveguides). The length of the channel waveguide was $L_0 = 5$ mm (more than $8\lambda_0$; λ_0 is the free space wavelength). For each misalignment case study, the structure is simulated again. The

transmission matrices between the $WR_{1.5}$ waveguides are extracted from simulations, for both aligned case and each misalignment case study. Loss extraction method applied to these transmission matrices to calculate the resulting attenuation due to misalignments.

The width of the $WR_{1.5}$ and channel waveguides along the x-direction are 191 μm and 180 μm, respectively. Therefore, the maximum possible misalignment along the x-direction is 5.5μm. Misalignment along the y-direction depends on the accuracy of the dimensions in the metallic stage used between the two $WR_{1.5}$ waveguides. A maximum of 20 μm for the misalignments in y and z-directions was assumed. Fig. 2.20(b) shows the simulation results for the tolerance in the waveguide attenuation for several misalignment case studies, over 500 to 650 GHz. The maximum value of the error, averaged over 500 to 650 GHz, among the studied misalignment cases is 0.124 dB. Considering the length difference of the fabricated line–defect waveguides (10.47 mm), the maximum tolerance in the extracted waveguide attenuation constant is $\frac{0.124}{10.47} = 0.012$ $\frac{\text{dB}}{\text{mm}}$. Therefore precise presentation for the measured average waveguide attenuation constant is 0.40 ± 0.012 $\frac{\text{dB}}{\text{mm}}$.

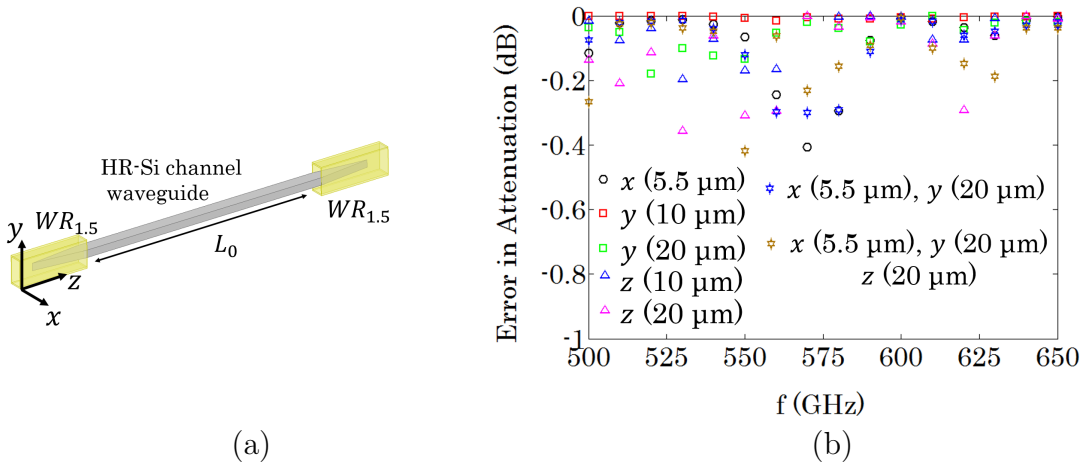

(a) (b)

Figure 2.20: (a) Simulation setup for examining error in the extracted waveguide loss. (b) Error in the attenuation due to the misalignment in each of x, y, and z -directions (directions and amount of the misalignments of each case study are shown).

2.4 Conclusions

In this chapter, a new photonic crystal line–defect waveguide based on SOG technology was presented for THz applications. The proposed waveguide is designed, fabricated, and

verified experimentally over the 500 to 700 GHz frequency range. The following synopses present comparisons of the SOG line–defect waveguide with other THz waveguide technologies in terms of: losses of the waveguides, fabrication complexity and scalability, and integrability with other components.

Losses of the Waveguides

Table 2.2 summarizes the losses of several THz waveguide structures investigated experimentally (in the same frequency range). For better comparison, the loss values are presented in $\frac{\text{dB}}{\lambda_0}$, in which λ_0 is the free space wavelength. As shown in this table, the proposed waveguide has significantly lower loss compared to the planar metallic waveguides (microstrip line and coplanar waveguide). However, the measured loss of the THz line–defect waveguide is higher than that of the rectangular metallic waveguide [39], and the suspended SOG waveguide [39].

Table 2.2: Performance comparison of THz waveguides

Waveguides	Frequency (GHz)	Attenuation constant α ($\frac{\text{dB}}{\lambda_0}$)
Microstrip line [32]	500 to 600	> 1.5
Coplanar waveguide [31]	500 to 600	> 2
Rectangular metallic waveguide [28]	500 to 750	0.045
Suspended SOG waveguide [39]	440 to 550	0.038
Line–defect SOG waveguide (Presented in this chapter)	540 to 630	0.208

To further investigate losses in the line-defect waveguide, Fig. 2.21 shows simulation results of the attenuation constant of this waveguide when pyrex is removed and HR-Si is assumed loss-less. Also, simulation results of the waveguide when two different conductivities assumed for HR-Si and pyrex is included are repeated from Fig. 2.8 (inset). The average waveguide attenuation constants are 0.39, 0.16, and 0.11 $\frac{\text{dB}}{\text{mm}}$ for these three cases. This simulation result shows that for a low-loss HR-Si, majority of the waveguide loss is due to the mode leakage to the photonic crystal structure.

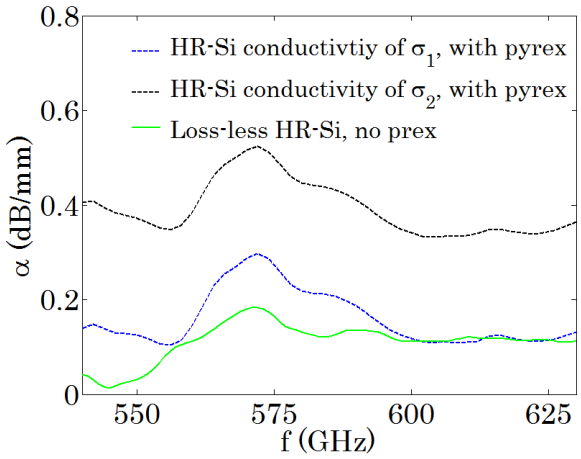

Figure 2.21: Losses of the line-defect waveguide, with and without material loss.

Fabrication Complexity and Scalability

In the fabrication process presented in [28] for rectangular metallic waveguides, the two halves of the waveguide are fabricated separately, and then connected through a complex alignment process. In addition, the fabrication process becomes even more challenging at higher frequencies inside the THz range; frequencies at which the waveguide performance becomes more sensitive to potential errors in the alignment step of fabrication.

The suspended SOG and line–defect SOG waveguides follow the same fabrication process. Using the advanced fabrication facility available for silicon-based devices, these planar waveguides are easy to fabricate. Moreover, the fabrication process is scalable to higher frequencies in the THz range.

Integrability with Other Components

The integration of passive and active components with a waveguide is an essential step towards achieving compact THz systems. Planar SOG waveguides provide promising platforms for integration compared to rectangular metallic waveguides.

In SOG technology, loss of the pyrex substrate should be avoided, not only for the waveguide but also for other integrated components. Therefore, the etched region of the pyrex substrate underneath the silicon layer needs to be expanded. In this case, the role of a handling structure that supports the waveguide and other potential components over the etched pyrex substrate becomes quite significant. In the suspended SOG waveguide

presented in [39], the integration of other components is challenging due to its specific handling structure. In contrast, the mechanically stable platform provided by the photonic crystal structure in the proposed THz line–defect waveguide, makes such integration quite achievable. Fig. 2.22 shows a few passive components based the THz line–defect waveguide, schematically. The studies required to verify these integrations are among the suggestions in the future works of this thesis.

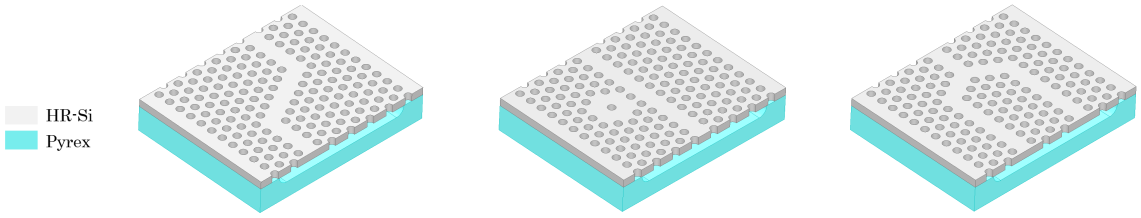

(a) (b) (c)

Figure 2.22: Passive components based on the THz line defect waveguide platform; (a) bend, (b) ring resonator, and (c) powder divider.

Chapter 3

Terahertz Silicon-BCB-Quartz Platform

In this chapter, a new platform for THz dielectric waveguides, Silicon-BCB-Quartz (SBQ), is proposed and investigated theoretically and experimentally. In the new THz waveguide, shown in Fig. 3.1(a), HR-Si is the guiding medium and quartz is used as the substrate. Guiding medium and the substrate are bonded using a benzocyclobutene (BCB) thin adhesive layer.

Silicon-on-Glass (SOG) technology, which was described in Section 1.2.2 and based on which THz line–defect photonic crystal waveguide presented in Chapter 2, uses pyrex as the substrate. In this technology, pyrex underneath the guiding channel is etched to reduce high losses of pyrex for frequencies above 200 GHz [48], as swhon in Fig. 3.1(b). The pyrex etching not only adds to the fabrication complexity, but also creates the challenge of handling the guiding channel over the etched pyrex. In the SBQ platform proposed in this chapter, crystal quartz is used as the substrate. Crystal quartz is among very low loss dielectrics in THz frequency range [1, 66], as swhon in Fig. 3.1(b), with high permittivity contrast with HR-Si (relative permittivities of quartz and HR-Si are 4.45 and 11.69 respectively). In contrast to SOG technology, etching the substrate is not required in the SBQ platform. This simplifies the fabrication significantly. Moreover, the quartz substrate could perform as a supporting platform for other potential components integrated with the SBQ waveguide and allows for realizing highly compact THz systems.

Crystalline quartz has thermal expansion coefficient very different from that of HR-Si; therefore, high temperature bonding processes, such as anodic bonding, are not applicable for bonding crystalline quartz and HR-Si. In contrast to high temperature bonding meth-

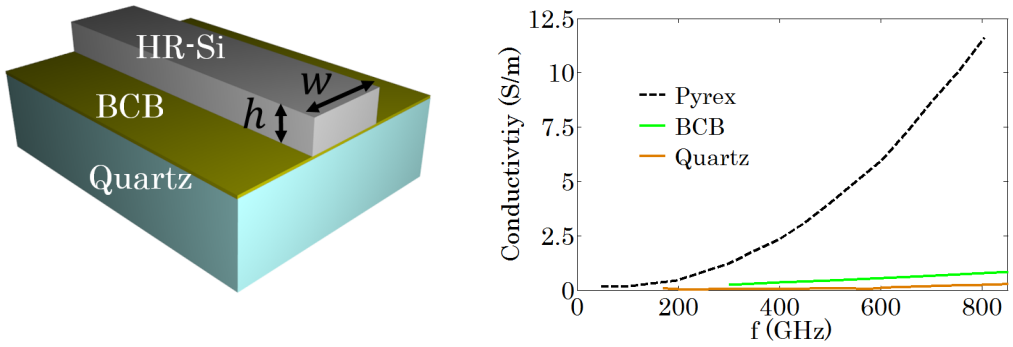

(a) (b)

Figure 3.1: (a) Proposed Silicon-BCB-Quartz (SBQ) waveguide structure. (b) Conductivities of pyrex, quartz, and BCB below 1 THz, (extracted from [48], [66, 75] and [73], respectively).

ods, adhesive bonding techniques, which uses an intermediate layer, can tolerate different thermal properties of the two medium to be bonded. BCB is an adhesive polymer, used for bonding, packaging, and which is also used as dielectric substrate [32, 67–72]. In SBQ, BCB is used for bonding HR-Si and the quartz substrate. This polymer has a relative permittivity of about 2.49 and very low-loss charachteristics in the THz frequency range, as shown in Fig. 3.1(b) [73].

Based on the proposed SBQ platform, a waveguide is designed for 500 to 580 GHz frequency range and presented in Section 3.1. Then, fabrication process is presented and discussed in Section 3.2. Measurement results are presented in Section 3.3. A waveguide bend is a mandatory component toward achieving compact miniaturized devices. In Section 3.4, simulation, fabrication, and measurement results of SBQ-based bend are presented. Conclusions of this chapter are presented in Section 3.5. It should be mentioned that some of the results presented in this chapter have been published in [74].

3.1 Design and Simulation

The structure of the proposed waveguide is shown in Fig. 3.1. Permittivities and loss values of crystalline quartz and BCB were extracted from [66, 75] and [73] respectively. HR-Si with different values of resistivity are characterized in the literature [59–61], as summarized in Table 3.1. In simulations, two different values for the conductivity of HR-Si

were considered, $\sigma_1 = 0.01\ \frac{\mathrm{S}}{\mathrm{m}}$ and $\sigma_2 = 0.42\ \frac{\mathrm{S}}{\mathrm{m}}$, which are the lowest and highest values presented in Table 3.1 (same procedure was employed in Chapter 2, in simulating THz line–defect waveguide).

Table 3.1: Conductivity of HR-Si

Silicon Resistivity	Frequency Range	Conductivity
10 kΩ – cm [59]	up to 1 THz	0.01 ($\frac{\mathrm{S}}{\mathrm{m}}$)
8 kΩ – cm [60]	up to 400 GHz	0.12 ($\frac{\mathrm{S}}{\mathrm{m}}$)
HR-Si [61] (Resistivity value not mentioned)	500 to 750 GHz	0.13 to 0.42 ($\frac{\mathrm{S}}{\mathrm{m}}$)

The dimensions of the SBQ waveguide cross section are $w = 180\ \mu$m and $h = 100\ \mu$m, and a thickness of 5 μm was assumed for the BCB layer. A simulation was performed using the FEM method in HFSS simulator. The propagation constant of the fundamental mode is shown in Fig. 3.2(a). The cutoff frequency of this mode is 415 GHz. Fig. 3.2(b) shows the attenuation constant of the mode, for both σ_1 and σ_2, conductivities of HR-Si. In Fig. 3.2(c)-(f), plots of the electric and magnetic fields of the fundamental mode are shown over the cross section of the waveguide. Fig. 3.3 shows the same plots for the second mode of the waveguide. As shown in Fig. 3.3(a), the cutoff frequency of the second mode is 470 GHz.

The SBQ waveguide was simulated in a back-to-back structure with tapered HR-Si channel waveguides as transitions between the rectangular metallic waveguides, $WR_{1.5}$, and the SBQ waveguide, as shown in Fig. 3.4 (a) and (b). The long edge of the $WR_{1.5}$ is along y-direction in order to excite the fundamental mode of the SBQ channel waveguide. It should be mentioned that although the simulation frequency range contains excitation frequencies of the second mode, it will not be excited due to mode mismatch (first mode is E_x mode, but second mode is E_y mode). The waveguide length is $L_1 = 9.43$ mm, which is more than $15\lambda_0$ over the frequency range of interest (λ_0 is free space wavelength). A simulation was performed for both conductivities of HR-Si, σ_1 and σ_2. Fig. 3.4(c) shows the insertion loss (S_{21}) through the back-to-back structure. Average insertion loss, over the 500 to 580 GHz frequency range, is -0.55 dB and -2.64 dB for σ_1 and σ_2 respectively, and it drops significantly for frequencies lower than 450 GHz as it approaches the cutoff frequency of the SBQ waveguide.

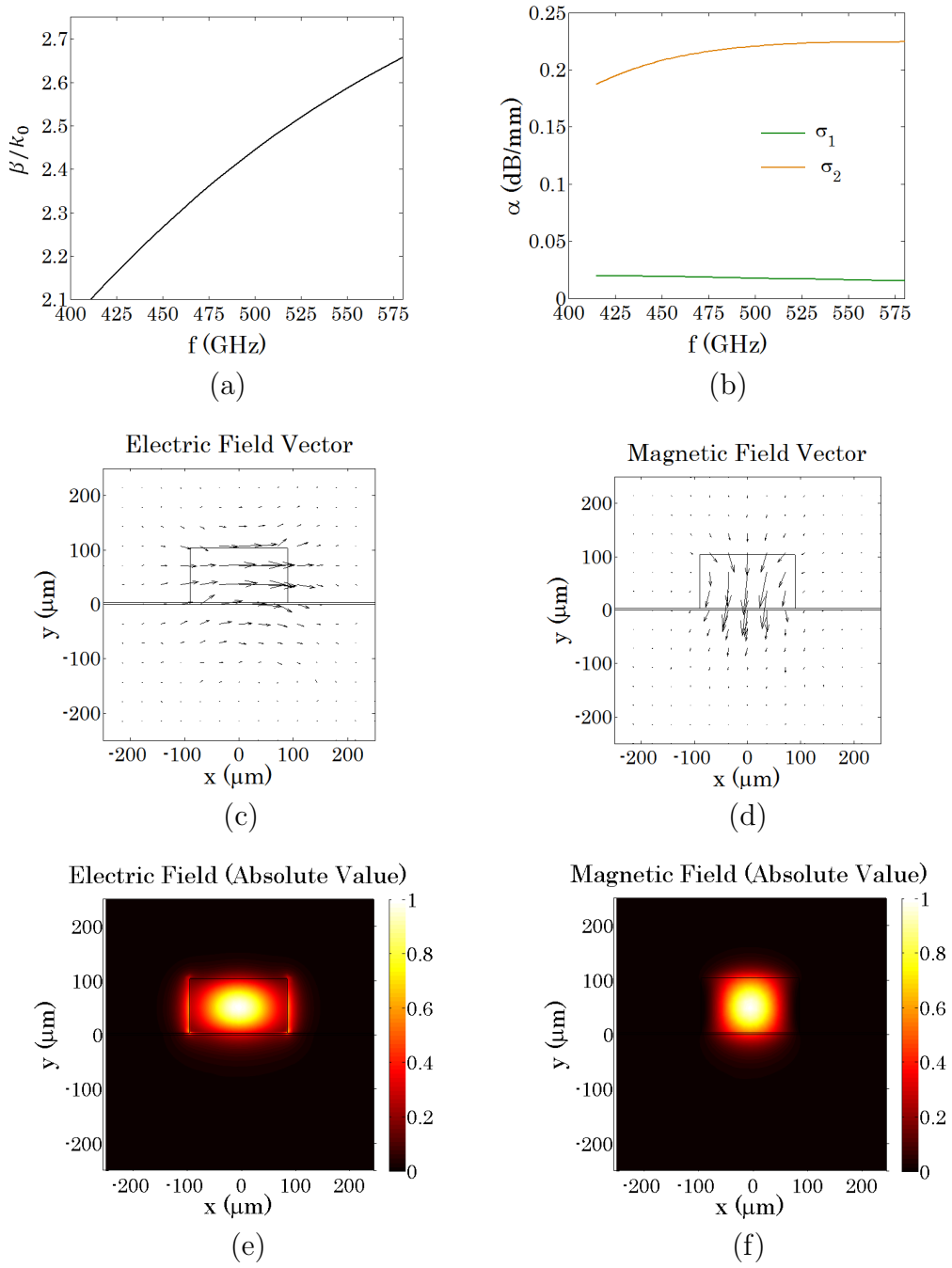

Figure 3.2: (a) and (b): Normalized propagation constant and attenuation constant (for two values of HR-Si conductivity) of the fundamental mode, (c) and (d) are the vector plots and (e) and (f) are the absolute value plots of fields over the cross section of the waveguide, all for first mode ($f = 530$ GHz).

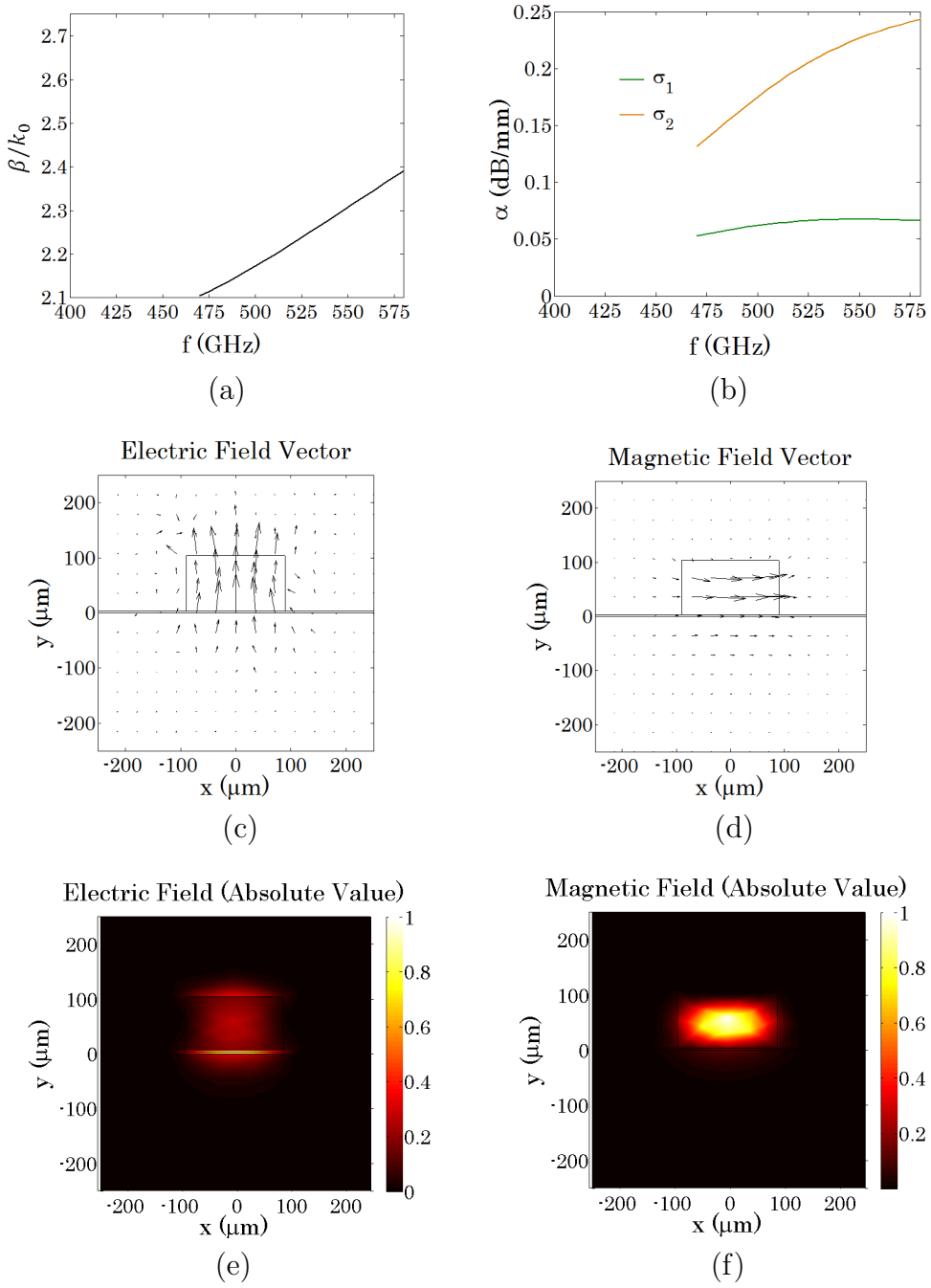

Figure 3.3: (a) and (b): Normalized propagation constant and attenuation constant (for two values of HR-Si conductivity) of the second mode, (c) and (d) are the vector plots and (e) and (f) are the absolute value plots of fields over the cross section of the waveguide, all for second mode ($f = 580$ GHz).

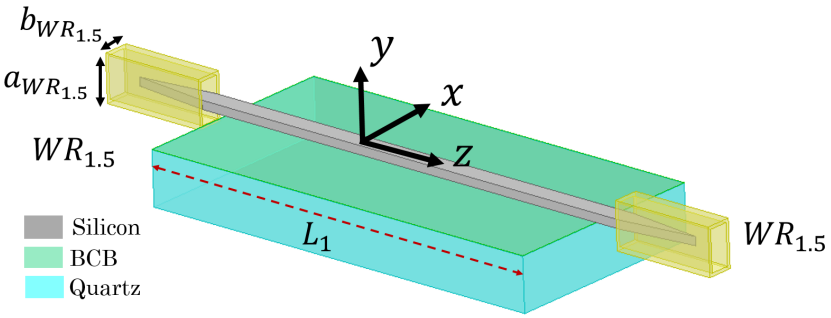

(a)

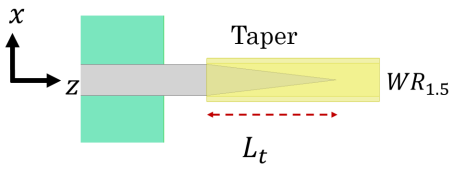

(b)

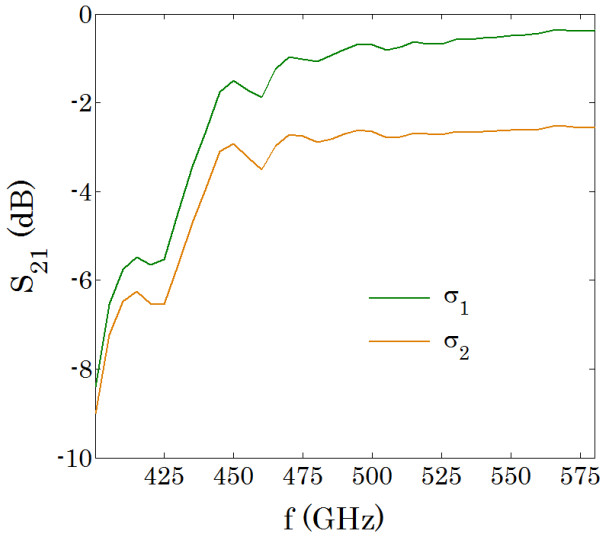

(c)

Figure 3.4: (a) Back-to-back structure of $WR_{1.5}$ waveguide connected to $WR_{1.5}$-SBQ transition, a straight segment of SBQ waveguide, and SBQ-$WR_{1.5}$ transition. Cross section dimensions of $WR_{1.5}$ are $a_{WR_{1.5}} = 0.381$ mm and $b_{WR_{1.5}} = 0.191$ mm. The waveguide length is $L_1 = 9.43$ mm. (b) Tapered HR-Si channel as a transition between SBQ waveguide and $WR_{1.5}$, with length of $L_t = 0.75$ mm. (c) Insertion loss through the back-to-back structure, for two values of HR-Si conductivity, σ_1 and σ_2.

3.2 Fabrication

The fabrication of the SBQ waveguide included three main steps: silicon-quartz bonding, optical lithography, and silicon etching.

3.2.1 Silicon-Quartz Bonding

Table 3.2.1 shows the thermal expansion coefficients of several materials at room temperature. Pyrex and silicon have very close thermal expansion coefficients; therefore, high temperature bonding methods, such as anodic bonding, are applicable to bond these materials, as presented in Chapter 2. In contrast, the thermal expansion coefficients of silicon and quartz are very different. This difference creates forces acting to de-bond the materials, because each material expands at a different rate compared to the other.

In [77] a repetitive process of thinning the silicon layer and annealing the bonded silicon-quartz interface is proposed. It is shown that, when the thickness of silicon is less than a few μm, silicon can be bonded to quartz despite their very different thermal expansion coefficients. However, in THz dielectric waveguides the thickness of the silicon ($\sim$ 100 μm at 500 GHz) is significantly higher than what is possible using this method.

In [81], a plasma-assisted bonding method is proposed for bonding silicon and quartz. Several plasma gases were investigated (e.g. oxygen, nitrogen, helium), and it is shown that oxygen provides the best result. In this method, plasma activation provides a highly hydrophilic and contamination-free contact surface due to the bombardment of energetic

Material	Thermal Expansion Coefficient ($10^{-6}\frac{1}{^\circ\mathrm{C}}$)
Silicon	2.33 - 2.6 [76, 77]
Pyrex	2.9 [76]
Crystal Quartz	$>$ 7.1 [78]
Silicon Nitride	2.44 [79]
Indium Phosphide	4.7 - 5.1 [80]

ions. This bonding process takes several hours ($\sim$ 10 hours). In addition, plasma-assisted bonding needs to be performed with special advanced equipment, not available in most laboratories.

BCB is a polymer using with which strong and chemical and thermalstable stable bondings can be achieved [67,69,70,72,82,83]. The curing of BCB happens through heating. In [84], BCB is used to bond silicon to silicon nitride. To cure BCB, the temprature is raised to 250 °C for 1 hour under vacuum conditions. In [85], silicon is bonded to pyrex, using the same recipe. The vacuum condition prevents air from being trapped during bonding; however, based on the results presented in [86], it is not a crucial requirement. In [86], silicon is bonded to indium phosphide using BCB in an oven without vacuum condition.

Although adhesive bonding is almost independent of the parameters of the wafers to be bonded, the thermal properties of the materials affect the curing temperature and time required. Considering the thermal expansion coefficients of materials presented in Table 3.2.1, the difference between these coefficients of quartz and silicon is significant compared to the other materials. Therefore bonding silicon and quartz, even using an adhesive bonding method, is challenging. Several recipes for this bonding were investigated, as described in the following sections.

Bonding in a Wafer Bonding Tool

The bonding steps are shown schematically in Fig. 3.5. Since the thickness of HR-Si is as low as 100 μm, working with such a thin layer without a handling layer is impractical. Therefore SOI pieces with a 500 μm thick handling silicon layer separated from the HR-Si by a thin (2 μm) silicon dioxide layer were used. The bonding process begins by cleaning the SOI and quartz pieces. This step is critical in order to achieve a strong bond. A solution of NH_4OH, H_2O_2, and H_2O at 75 °C is used for cleaning. The next step is to coat the SOI and quartz pieces with BCB polymer. In order to achieve better adhesion, a very thin layer of an adhesion promoter (AP3000) is spin coated first Fig. 3.5(b). Spin coating BCB on each of the quartz and SOI pieces results in a thin BCB layer (4 μm), Fig. 3.5(c). The edge beads of BCB on the edges of the pieces were removed using a rinse solvent (T1100).

To cure the BCB layer, wafer bonding equipment (AML AWB-04 Aligner Wafer Bonder) was used. The pieces were loaded into the machine an the pressure reduced to 10^{-4} mbar. Then the pieces were heated at 190 °C without contact. After one hour, the pieces came into contact at a pressure of 0.35 MPa. The temperature was then increased to 250 °C for one hour. The cooling process was preformed using nitrogen gas (cooling rate $\sim$ 5

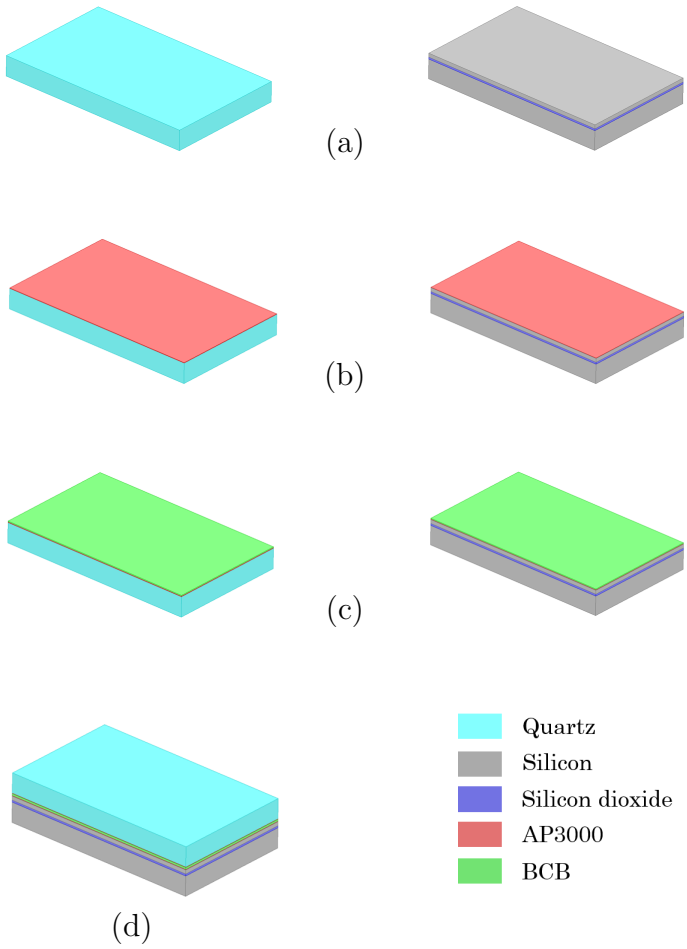

Figure 3.5: (a) Cleaned quartz and SOI pieces, (b) pieces spin coated by adhesion promoter (AP3000), (c) pieces spin coated by BCB, (d) silicon bonded to quartz through cured BCB.

$\frac{^{\circ}C}{min}$). After the chamber temperature reduced to 100 °C, the pieces were unloaded from the equipment. The pieces were found to have multiple cracks.

The process was repeated with different parameters for curing and cooling down steps. A lower temperate (190 °C) was used for the curing of BCB. For cooling down, before applying the nitrogen gas, it was found that leaving the pieces to cool in the vacuum condition until the temperature reduced to 150 °C was best. The cooling rate in vacuum condition is significantly lower than that of nitrogen cooling (~ 1 $\frac{^{\circ}C}{min}$ versus ~ 5 $\frac{^{\circ}C}{min}$). After the temperature had reached the desired level, nitrogen gas was used to cool the chamber temperature down to 50 °C before opening the chamber. This recipe with a slower cool

down rate was found to be successful. The total process time was about three hours. Since a lower temperature was used for the BCB curing (190 °C compared to 250 °C), it is reasonable to expect that a longer curing time would result in better bonding.

Bonding on a Hotplate

The curing of BCB in a vacuum chamber (wafer bonding tool) is a time-consuming process and requires special equipment. In contrast, performing the curing on a hotplate is fast and easy to access. Bonding silicon and quartz on a hotplate can be accomplished in 30 min. The bonding strength was sufficient to perform the remaining steps of the waveguide fabrication.

It should be mentioned that several trials for BCB curing in an oven were performed as well, but it was found that better results can be achieved by BCB curing on a hotplate. Although it is expected that the bonding strength will be lower when a hotplate has been used for BCB curing rather than a wafer bonding tool, hotplate bonding was used to fabricate the SBQ waveguide because it is a simple and fast process. Quantification of the bonding strength is not included in this thesis, but it is among the suggested future work to be undertaken.

After bonding, the handle silicon layer of the SOI was removed using etching, and the silicon dioxide layer was removed by HF (49 %) wet etching. A Cr/Au (30/150 nm) mask on the back side of the quartz was used to protect it from the etching solution.

3.2.2 Optical Lithography

The steps of the optical lithography process are shown schematically in Fig. 3.6. First, the SBQ pieces were coated with a thick photoresist (AZ P4620; 11 μm). After coating the pieces with photoresist, hotplate baking was performed (115 °C for 90 seconds) and the pieces were left in cleanroom for three hours to rehydrate (the same process as the recipe used for the SOG platform in Chapter 2). Then, optical lithography was performed to pattern the photoresist, followed by developing (in AZ 400K developer). The optical microscope images of the results are shown in Fig. 3.7. As shown in this figure, the photoresist has been removed in some areas, resulting in an incomplete pattern. Different recipes for the baking step performed to resolve this issue. It was found that, due to the very low thermal conductivity of quartz and BCB, the baking of the photoresist could not be performed properly on a hotplate. In contrast to the hotplate, baking the photoresist using an oven is almost independent of the thermal properties of the substrate materials.

Several trials were conducted, changing the baking temperature and duration. The most stable recipe from which multiple successful results were achieved was:

1. Start baking 10 min after coating SBQ by photoresist.
2. Bake in oven at 50 °C for 10 min.
3. Increase the temperate to 100 °C, and bake at this temperature for 50 min.

Figure 3.8 shows an optical microscope image of the photoresist pattern achieved using this recipe.

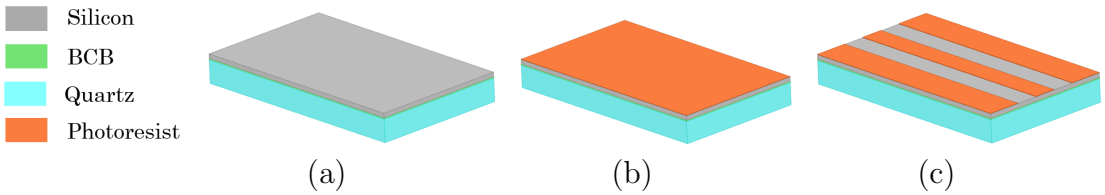

Figure 3.6: (a) SBQ piece, (b) piece coated with photoresist, (c) photoresist patterning using optical lithography.

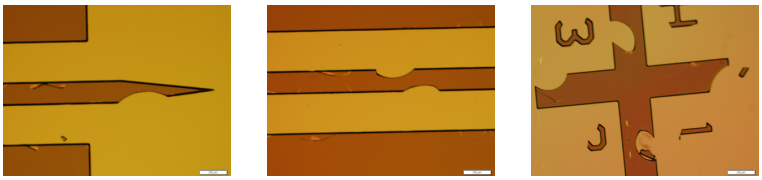

Figure 3.7: Optical microscope images of three different spots of the patterned photoresist on SBQ structure, when a hotplate used for baking the photoresist.

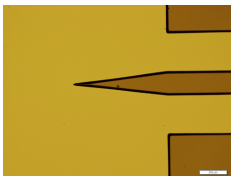

Figure 3.8: Optical microscope image of patterned photoresist on SBQ structure, when photoresist baked using proposed recipe.

3.2.3 Silicon Etching

The next step involves etching the silicon via DRIE, using the patterned photoresist as the mask. Cooling down the device during etching is an important factor of this process. The heating of the silicon during DRIE results in erosion of the photoresist and an etch rate and mask selectivity reduction. The recipe used for the DRIE (Bosch recipe), uses active cooling to a temperature of 15 °C during the process. However, the low thermal conductivity of the quartz and BCB was problematic. Erosion in the photoresist was observed even after only a few cycles of the Bosch recipe, as is shown in the optical microscope image in Fig. 3.9.

The photoresist erosion during DRIE was considered when developing the photoresist baking recipe presented in the previous section. Moreover, to avoid executive heat up, the the required Bosch cycles were grouped into sets. Etching to a depth of 100 μm requires around $\sim$ 250 cycles of the Bosch recipe; in this case the cycles were split into 10 sets of 25 cycles. A cooling period was included after each set of 25 cycles.

After etching the silicon, the remaining photoresist was removed in acetone. Optical and scanning electron microscope images of one of the fabricated samples are shown in Fig. 3.10 and Fig. 3.11 respectively.

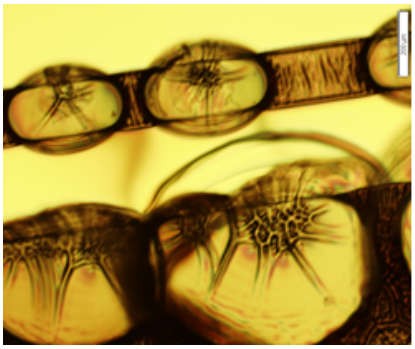

Figure 3.9: Optical microscope image of erosion in photoresist due to excessive heat up during DRIE process.

3.3 Measurement

Figure 3.12(a) shows the measurement setup. A Network Analyzer (Agilent PNA-X) connected to frequency extender modules (from Virginia Diodes Inc) was used as the source

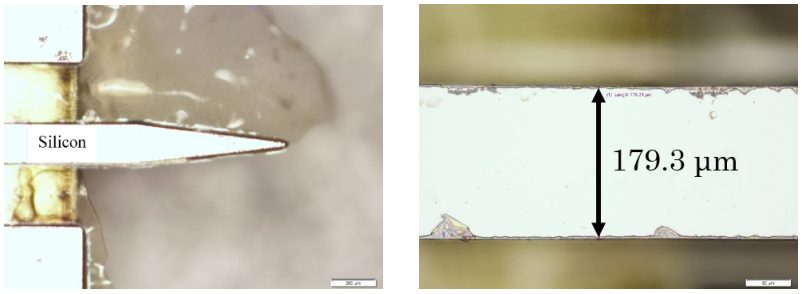

(a) (b)

Figure 3.10: Optical microscope images of: (a) SBQ waveguide and tapered HR-Si channel, and (b) magnified SBQ waveguide.

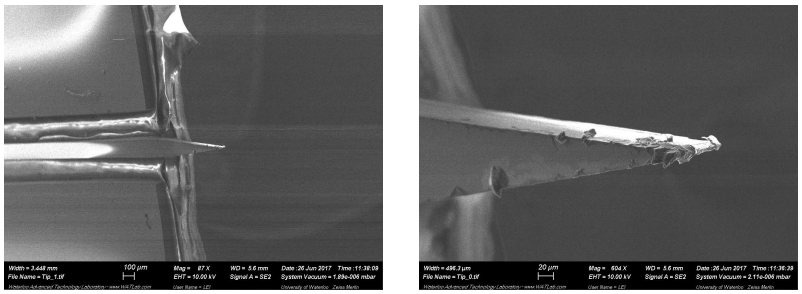

(a) (b)

Figure 3.11: Scanning electron microscope images of: (a) fabricated waveguide, and (b) magnified tapered HR-Si channel.

and detector in the setup. Frequency extender modules have rectangular metallic waveguides, $WR_{1.5}$, at their outputs. There is a metallic stage between two $WR_{1.5}$ waveguides as a holder for the SBQ waveguide. The stage is designed such that the middle of the tapered HR-Si channels align with the centres of $WR_{1.5}$ waveguides. This stage is manufactured using machining. Frequency extender modules are located on micropositioners for alignment and safe insertion of tapered HR-Si channels into $WR_{1.5}$ waveguides.

In order to de-embed the SBQ waveguide characteristics from the back-to-back structure, SBQ waveguide is fabricated and measured with two different lengths, $L_1 = 9.43$ mm and $L_2 = 19.9$ mm. Fig. 3.12(b) shows the measured S_{21} and S_{11} of both lengths. The average of S_{21} over the 500 to 580 GHz frequency range is -2.44 dB for L_1 and -2.96 dB for L_2.

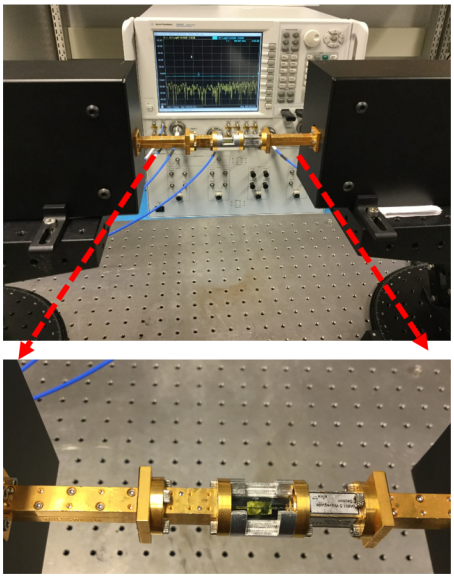

(a)

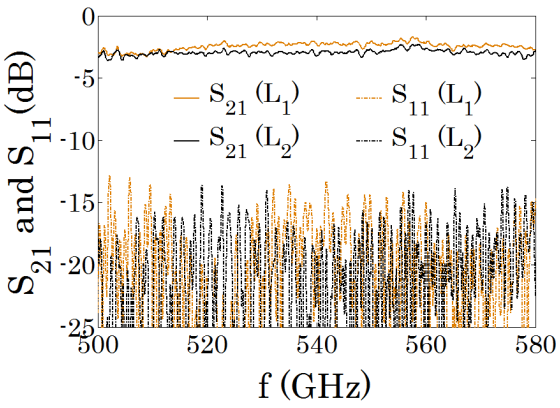

(b)

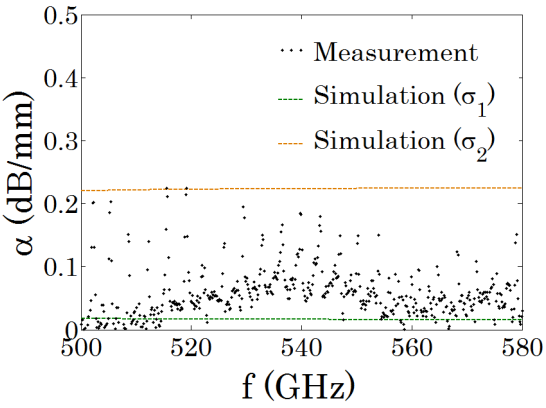

(c)

Figure 3.12: (a) Measurement setup; frequency extender modules with $WR_{1.5}$ outputs, which are connected to a metallic stage. The THz SBQ waveguide is located on the stage and tapered HR-Si channels are inserted into $WR_{1.5}$ waveguides. (b) Measured S_{21} and S_{11} for two SBQ waveguides with lengths of $L_1 = 9.43$ mm, and $L_2 = 19.9$ mm, (c) Attenuation constant; measurement and simulation results.

3.3.1 Extracting the Waveguide Attenuation Constant

The attenuation constant of the SBQ waveguide is extracted from the scattering parameters measured for two SBQ waveguides with lengths of $L_1 = 9.43$ mm and $L_2 = 19.9$ mm, using the same method presented in Section 2.3.1.

Figure 3.12(c) shows the attenuation constant extracted from measurement results, also the simulation results for both conductivities of HR-Si, σ_1 and σ_2. The measured attenuation constant has the average of 0.046 $\frac{\text{dB}}{\text{mm}}$, which is equivalent to 0.026 $\frac{\text{dB}}{\lambda_0}$ over 500 to 580 GHz frequency range.

The error due to the misalignments during measurements was studied in Section 2.3.2. Based on the results presented in that section, the maximum value of the error, averaged over 500 to 580 GHz, among the studied misalignment cases is 0.095 dB. Considering the length difference between two SBQ waveguides (10.47 mm), the maximum tolerance in the extracted waveguide attenuation constant is $\frac{0.095}{10.47} = 0.01$ $\frac{\text{dB}}{\text{mm}}$. Therefore, the precise presentation of the measured average attenuation constant of the SBQ waveguide is 0.046 $\pm$ 0.01 $\frac{\text{dB}}{\text{mm}}$. The tolerance in this measurement can be reduced by using a longer length difference, and by improving the measurement setup for better alignment. A more accurate measurement setup is under development and not available at the time that these measurements were performed. The measurement setup improvement is listed among the future work of this thesis.

As presented before, the average of S_{21} over 500 to 580 GHz range for the long waveguide ($L_2 = 19.9$ mm) is -2.96 dB. Using the average of the waveguide loss, coupling between $WR_{1.5}$ and SBQ waveguides could be calculated, approximately, as $\frac{-2.96+0.046\times19.9}{2}$ = -1 dB. The coupling value would be the same if the short waveguide, $L_1 = 9.43$, and the average of S_{21} for that, -2.44 dB, be used to calculate coupling between $WR_{1.5}$ and SBQ waveguides. It should be mentioned that the calculated value, -1 dB, includes not only the coupling between $WR_{1.5}$ and SBQ waveguides, but also loss of these waveguides over the taper section. Since the taper length is quite short, majority of the calculated loss is because of the mode mismatch between the two different waveguides.

The losses of all three materials used in the SBQ waveguide structure (HR-Si, quartz, and BCB) affect the waveguide attenuation constant. However, since HR-Si is the guiding region and contains the majority of the mode power, it is expected that this material has the most significant effect on the modal properties, including the mode attenuation constant. More simulations with different conductivities assumed for HR-Si were performed to provide an estimation of the conductivity of the used HR-Si sample. The result was that with conductivity of $\sigma = 0.05$ $\frac{\text{S}}{\text{m}}$ assumed for HR-Si, average of the waveguide loss over

500 to 580 GHz frequency range is the same in simulation and measurement. As shown in Fig. 3.12(c), based on simulation, using HR-Si with conductivity of $\sigma_1 = 0.01 \frac{\mathrm{S}}{\mathrm{m}}$, loss of the waveguide reduces to 0.015 $\frac{\mathrm{dB}}{\lambda_0}$.

3.4 SBQ Bend

The Waveguide bend is among the most essential passive components for realizing compact systems. Achieving sharper bends without significant increase of losses is highly desirable for system miniaturization. In this section, an SBQ bend is studied and investigated experimentally. Fig. 3.13(a) shows a back-to-back SBQ bend structure, which contains four 90° bends; all with radius of R. Bend radius (R) is swept in simulation from 0.5 to 2 mm. Fig. 3.13(b) shows the simulation result. As can be seen in this figure, the bending loss is insignificant for a bend with radius equal to or more than $R = 1.5$ mm.

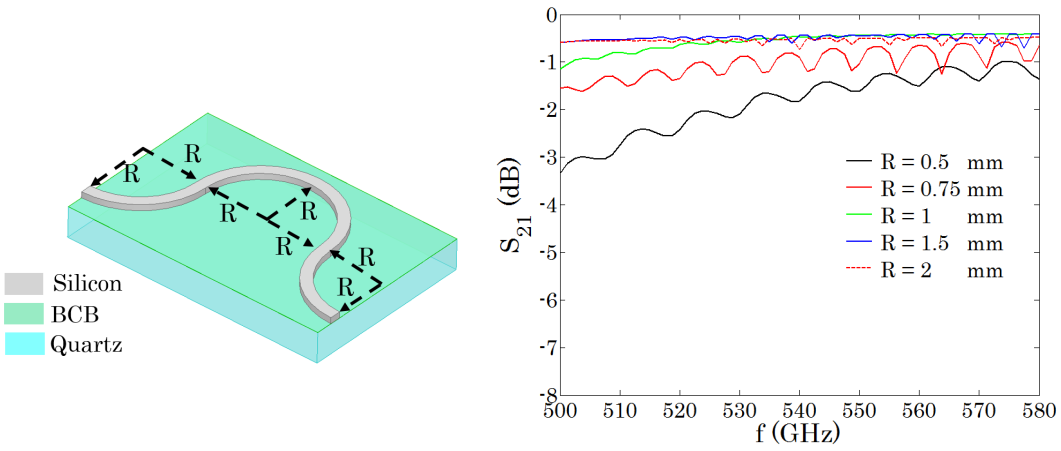

(a) (b)

Figure 3.13: (a) SBQ bend structure; containing four back-to-back 90° bends. (b) Simulation results of the bend structure, for $R = 0.5$, 0.75, 1, 1.5, and 2 mm.

The bend structure is fabricated using the same recipe presented in Section 3.2. Fig. 3.14(a) shows the schematic of the SBQ bend device, which includes: tapered HR-Si channels as transitions between the $WR_{1.5}$ waveguide and the SBQ waveguide, SBQ waveguides with lengths of $L_0 = 6.77$ mm, and SBQ bend in the middle which contains four back-to-back 90° bends all with radius of $R = 1.5$ mm. The measurement setup and the fabricated bend device are shown in Fig. 3.14(b).

Insertion loss of the bend structure (the region bounded by dashed lines in Fig. 3.14(a), could be extracted from the measurement results of the bend device by de-embedding the effect of the $WR_{1.5}$ waveguide, tapered HR-Si channel, and SBQ straight waveguide segments using the same method presented in the previous section. Suppose the excitation sections, including the $WR_{1.5}$ waveguide and tapered HR-Si channel, have transmission matrices of $\mathbf{T_x}$ and $\mathbf{T_y}$ on two ends. Considering the transmission matrices of the SBQ waveguides with the length of L_0 as $\mathbf{T_{L_0}}$, and the transmission matrix of the bend structure $\mathbf{T_B}$, then, the measured transmission matrix of the bend structure can be written as:

$$\mathbf{T_3} = \mathbf{T_x}\mathbf{T_{L_0}}\mathbf{T_B}\mathbf{T_{L_0}}\mathbf{T_y} \tag{3.1}$$

The transmission matrix of the SBQ waveguide with length L_0, as presented in the previous section, could be written as:

$$\mathbf{T_{L_0}} = \begin{bmatrix} e^{-\gamma L_0} & 0 \\ 0 & e^{\gamma L_0} \end{bmatrix} \tag{3.2}$$

Since the radius of the bend section is large in comparison to the wavelength, the bend structure can be assumed to act as a single mode waveguide with higher radiation losses due to bending; therefore, the transmission matrix of the bend structure can be written as:

$$\mathbf{T_B} = \begin{bmatrix} e^{-B} & 0 \\ 0 & e^{B} \end{bmatrix} \tag{3.3}$$

To extract $\mathbf{T_B}$ from the measured matrix, $\mathbf{T_3}$, the measured matrix for the waveguide with length of L_2 is used:

$$\mathbf{T_2} = \mathbf{T_x}\mathbf{T_{L_2}}\mathbf{T_y} \tag{3.4}$$

Multiplying $\mathbf{T_3}$ by the inverse of $\mathbf{T_2}$:

$$\mathbf{T_3}\mathbf{T_2^{-1}} = \mathbf{T_x}\mathbf{T_{B2}}\mathbf{T_x^{-1}} \tag{3.5}$$

In which,

$$\mathbf{T_{B2}} = \begin{bmatrix} e^{-\gamma(2L_0-L_2)-B} & 0 \\ 0 & e^{\gamma(2L_0-L_2)+B} \end{bmatrix} \tag{3.6}$$

The eigenvalues of $\mathbf{T_3}\mathbf{T_2^{-1}}$ and $\mathbf{T_{B2}}$ are the same. The value of γ, which is the propagation of the straight waveguide, is known from the previous section. Therefore, matrix T_B can be calculated.

Matrix T_B is converted to the scattering matrix, and the S_{21} parameter of this matrix is plotted in Fig. 3.14(c). This figure also includes the simulation results for the same

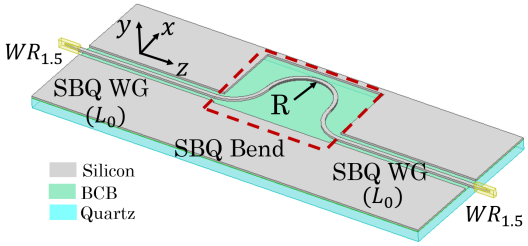

(a)

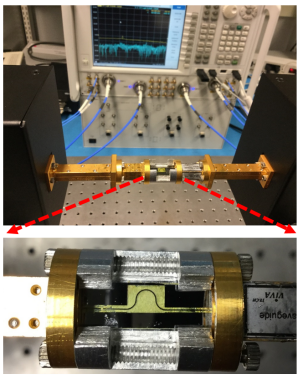

(b)

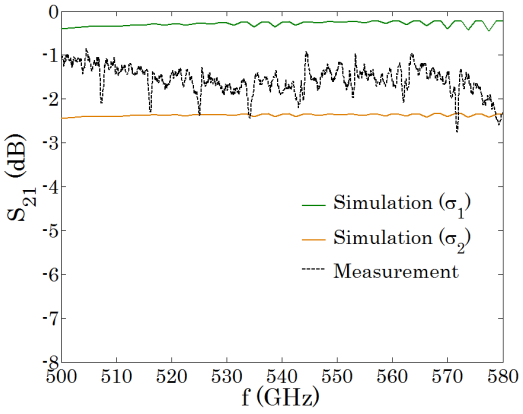

(c)

Figure 3.14: (a) Schematic of SBQ bend device whit four 90° bends of radius $R = 1.5$ mm, tapered HR-Si channels, and two SBQ straight waveguides each with length of $L_0 = 6.77$ mm. (b) Measurement setup with SBQ device located on the stage. (c) S_{21} of the bend structure; simulation and measurement results.

structure for two HR-Si conductivities, σ_1 and σ_2. The average of the measured insertion loss (S_{21}) is -1.56 dB over the 500 to 580 GHz frequency range. The average of the simulation results of the same quantity over the same range of frequency are -0.28 dB and -2.37 dB, for σ_1 and σ_2 respectively. The results show that the bending loss of the structure is tolerable for this range of frequencies and can be reduced even further when using an HR-Si with lower losses (σ_1).

3.5 Conclusions

In this chapter, an SBQ structure was proposed and investigated as an efficient platform for compact THz systems. An average measured waveguide loss as low as 0.026 $\frac{\text{dB}}{\lambda_0}$ was reported for the fabricated SBQ samples, over the 500 to 580 GHz frequency range. The following synopses are comparisons of the presented waveguide with other THz waveguide technologies in terms of: losses of the waveguides, fabrication complexity and scalability, and integrability with other components.

Losses of the Waveguides

Table 3.2 is a repeat of Table 2.2, with the SBQ waveguide results added to the end. The proposed SBQ waveguide has the lowest loss among the waveguides shown in this table.

Table 3.2: Performance comparison of THz waveguides

Waveguides	Frequency (GHz)	Attenuation constant α ($\frac{\text{dB}}{\lambda_0}$)
Microstrip line [32]	500 to 600	> 1.5
Coplanar waveguide [31]	500 to 600	> 2
Rectangular metallic waveguide [28]	500 to 750	0.045
Suspended SOG waveguide [39]	440 to 550	0.038
Line–defect SOG waveguide (Presented in Chapter 2)	540 to 630	0.208
SBQ waveguide (Presented in this chapter)	500 to 580	0.026

Fabrication Complexity and Scalability

One of the primary advantages of the presented SBQ waveguide is that it is easy to fabricate. As mentioned in Section 2.4, an advantage of THz dielectric waveguides is their sim-

pler fabrication processes compared with metallic rectangular waveguides [28]. Moreover, they are scalable to the higher frequencies in the THz range, using the same fabrication processes.

Comparing the SBQ waveguide with the SOG waveguides (suspended SOG waveguide [39], and line–defect waveguide presented in Chapter 2), the SBQ waveguide has a significantly easier fabrication process due to the absence of the substrate etching requirement. Also, the verified ability to successfully perform adhesive bonding on a hotplate, means that the SBQ platform can be fabricated using basic cleanroom facilities.

Thermal Stability

As it was experienced during the fabrication process of the SBQ waveguide, very different thermal expansion coefficients of silicon and quartz degrades the thermal stability of this platform. In contrast, rectangular metallic waveguide and SOG waveguides can tolerate severe thermal conditions better than the SBQ platform. Depending on the application for which the SBQ platform might be used, several thermal condition scenarios can be studied. As an example scenario performed in this research, it was found that SBQ platform can tolerate temperature change from 190 °C to the room temperature with a cooling rate low enough.

Integrability with Other Components

The integration of passive and active components with a waveguide is an essential step towards achieving compact THz systems. Comparing the SBQ and SOG platforms in terms of integration, the SBQ platform has the remarkable advantage of having quartz as the substrate for all integrated components; in contrast, the etched pyrex substrate of the SOG platform creates challenges for integration purposes.

Chapter 4

THz Slot Waveguides for Field Confinement

Slot waveguides, consisting of a dielectric layer with a narrow slot region in the middle, provids highly confined fields in the slot region, and consequently, an enhanced interaction between the waveguide mode and a material in the slot region. In the optical frequency range, this type of waveguide has been studied extensively, and used for a variety of applications including sensing [87–89]. In the THz frequency range, the concept of a slot dielectric waveguide has been investigated theoretically in [90], using a free standing silicon layer (no substrate). However, since no substrate is considered in [90], their approach does not result in a practical waveguide. There have not been any fabrication or measurement results presented for slot dielectric waveguides in the THz frequency range to date. In this chapter, two THz slot waveguide structures are proposed and investigated: 1) an SBQ THz slot waveguide, and 2) a THz slot plasmonic waveguide based on doped-GaAs.

In Section 4.1, an SBQ THz slot waveguide is proposed. In this waveguide, the electric field is confined in a sub-wavelength region ($\frac{\lambda_0}{6} \times \frac{\lambda_0}{28}$) of the waveguide cross section, at f = 530 GHz (λ_0 is the free space wavelength). The design of this waveguide and its fabrication and measurement results are presented. Then, in Section 4.2, a THz slot plasmonic waveguide based on doped-GaAs is presented. Using simulation results, it is shown that the fundamental mode of this waveguide can be confined in a deep-subwavelength region ($\frac{\lambda_0}{19} \times \frac{\lambda_0}{19}$) of the waveguide cross section, at $f = 530$ GHz (λ_0 is the free space wavelength). Conclusions drawn from the work reported in this chapter are presented in Section 4.3.

4.1 THz SBQ Slot Waveguide

In this section, using the SBQ platform proposed in Chapter 3, an SBQ THz slot waveguide is proposed. The waveguide is designed for use at the 500 to 600 GHz frequency range, and its fabrication and measurement results are presented. In Section 4.1.1, the waveguide structure and simulation results are presented. Then, in Section 4.1.2, fabrication results are presented. Two different lengths of the proposed waveguide were fabricated. Measurement results are presented in Section 4.1.3.

4.1.1 THz SBQ Slot Waveguide: Design

Consider a free standing channel waveguide, as shown Fig. 4.1(a). Due to the permittivity difference between regions 1 and 2 (inside and outside of the guiding region), the E_x-component of the electric field has discontinuity at the vertical boundaries between the two regions. Based on the continuity of the normal component of the displacement vector, $\overrightarrow{\mathbf{D}} \cdot \hat{\mathbf{x}}$:

$$\overrightarrow{\mathbf{D}}_1 \cdot \hat{\mathbf{x}} = \overrightarrow{\mathbf{D}}_2 \cdot \hat{\mathbf{x}} \quad \text{at the vertical boundaries} \tag{4.1}$$

$$E_{x1}\varepsilon_{r1} = E_{x2}\varepsilon_{21} \quad \text{at the vertical boundaries} \tag{4.2}$$

in which, ε_{r1} and ε_{r2} are the relative permittivity of regions 1 and 2, respectively. Therefore, when $\varepsilon_{r1} > \varepsilon_{r2}$, E_{x2} would be larger than E_{x1} by a factor of $\frac{\varepsilon_{r1}}{\varepsilon_{r2}}$. The distribution of the amplitude of E_x along the x axis for $y = y_0 + \frac{h}{2}$ is shown in Fig. 4.1(a). A slot waveguide, Fig. 4.1(b), is a channel waveguide with a narrow gap in the middle. Because of the discontinuity of the E_x-component of the electric field, electric field would be highly confined inside the slot region of the waveguide, as shown in Fig. 4.1(b).

Figure 4.2(a) shows a slot waveguide based on the SBQ platform. A simulation of the waveguide was performed using the FEM method in HFSS simulator. The slot width is $w_{slot} = 20$ μm, and the waveguide total width is $2w + w_{slot} = 260$ μm. Thicknesses of HR-Si and BCB were 100 μm and 5 μm respectively. A conductivity of $\sigma_1 = 0.05$ $\frac{\text{S}}{\text{m}}$ was assumed for HR-Si in this simulation. Permittivities and loss values of crystalline quartz and BCB were extracted from [66, 75] and [73] respectively, as were presented in Chapter 3. The simulation results for the normalized propagation and attenuation constants of the first three modes of this waveguide are plotted in Fig. 4.2(b) and (c). The field distributions of these modes are plotted in Fig. 4.3, Fig. 4.4, and Fig. 4.5.

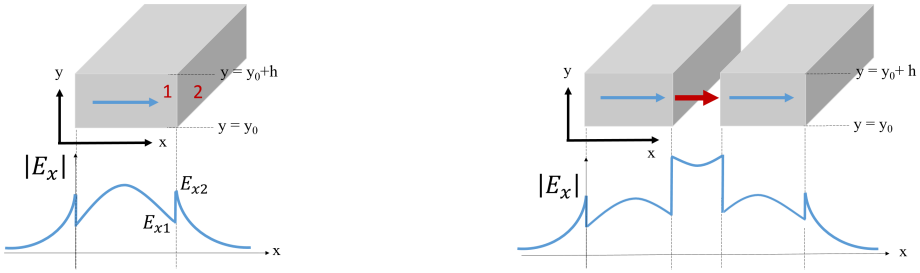

Figure 4.1: (a) Distribution of the amplitude of the E_x-component of the electric field of the first E_x-mode of a channel waveguide, along the x axis, at $y = y_0 + \frac{h}{2}$. (b) Distribution of the amplitude of the E_x-component of the electric field of the first E_x-mode of a slot waveguide, along the x axis, at $y = y_0 + \frac{h}{2}$.

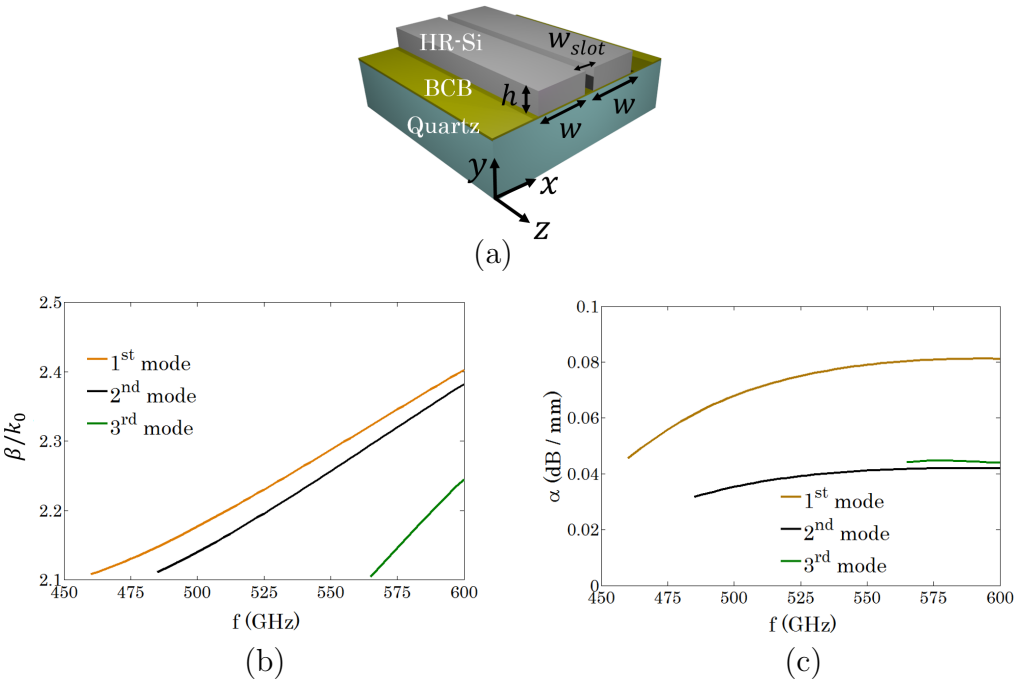

Figure 4.2: (a) THz SBQ slot waveguide (w_{slot} = 20 μm, w = 120 μm, h = 100 μm), (b) Normalized propagation constants of the first three modes of the waveguide (k_0 is the free space wavenumber), (c) Attenuation constants of the first three modes.

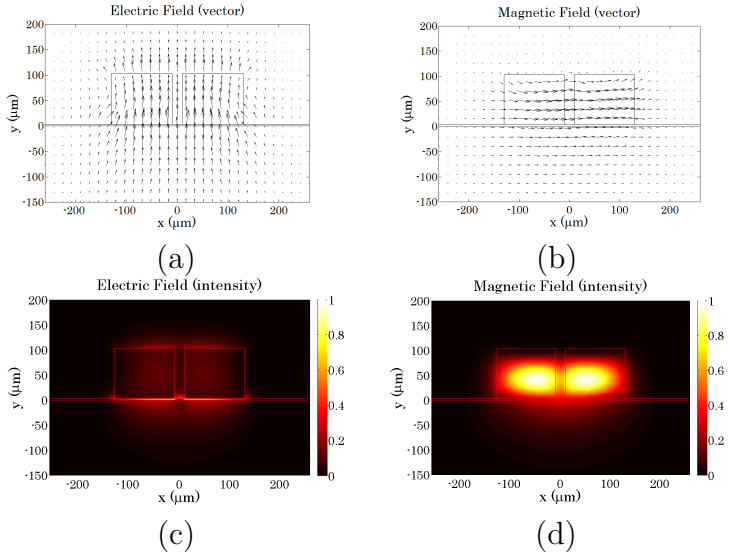

Figure 4.3: First mode of the SBQ Slot Waveguide: (a) and (b) are vector plots of the electric and magnetic fields, respectively, and (c) and (d) are the intensity plots of the electric and magnetic fields, respectively.

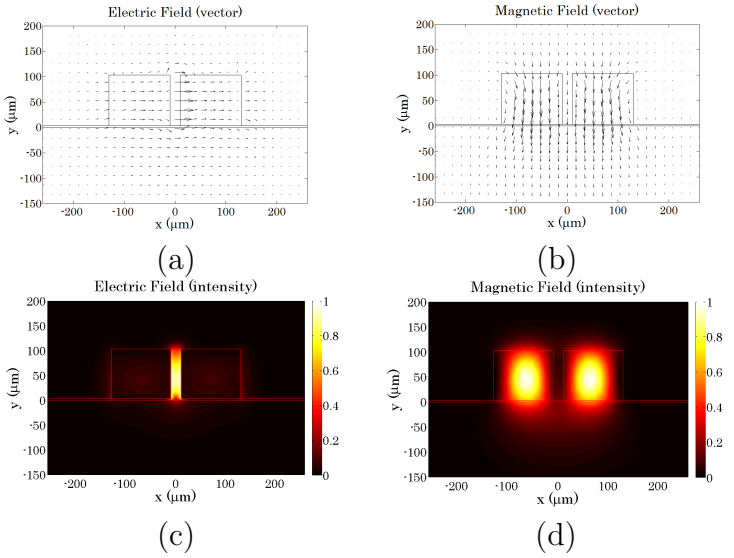

Figure 4.4: Second mode of the SBQ Slot Waveguide: (a) and (b) are the vector plots of the electric and magnetic fields, respectively, and (c) and (d) are the intensity plots of the electric and magnetic fields, respectively.

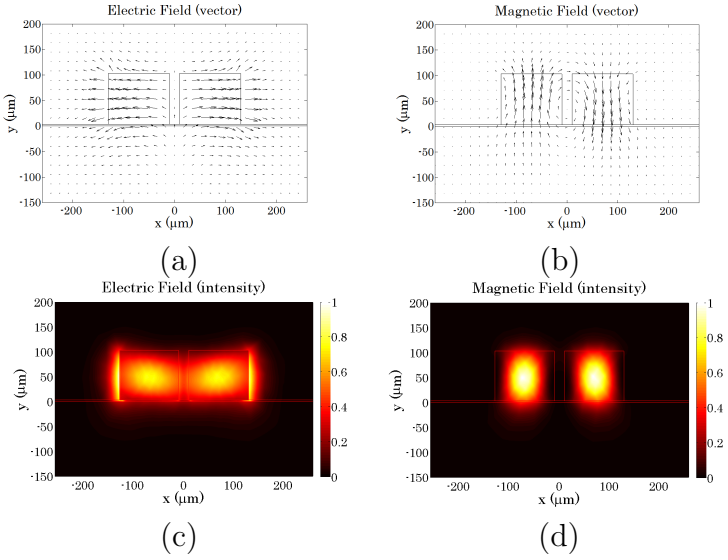

Figure 4.5: Third mode of the SBQ Slot Waveguide: (a) and (b) are the vector plots of the electric and magnetic fields, respectively, and (c) and (d) are the intensity plots of the electric and magnetic fields, respectively.

As shown in Fig. 4.4(c), the electric field of the second mode is highly confined in the slot region ($w_{slot} \times h = 20\ \mu\text{m} \times 100\ \mu\text{m} = \frac{\lambda_0}{20} \times \frac{\lambda_0}{6}$ at $f = 530$ GHz, where λ_0 is the free space wavelength). It is this mode of the waveguide which is of interest for applications such as sensing.

To characterize the SBQ slot waveguide while its second (confined) mode is excited, a Network Analyzer with frequency extender modules were used. Each frequency extender module has metallic rectangular waveguide output, $WR_{1.5}$; therefore, a low loss transition from $WR_{1.5}$ to the SBQ slot waveguide was required. Fig. 4.6(a) shows a transition from $WR_{1.5}$ to the SBQ channel waveguide (taper length of $L_t = 0.75$ mm), and then from the SBQ channel waveguide to the SBQ slot waveguide (taper length of $L_{t1} = 3$ mm). Due to a significant field distribution difference between the fundamental mode of the SBQ channel waveguide and the second mode of the SBQ slot waveguide, a long taper between them is expected to achieve a low loss transition. The gap between the tapered channel and slot waveguides is $g = 5\ \mu$m, as shown in Fig. 4.6(a). The size of this gap, g, and the taper length between the SBQ channel and slot waveguides, L_{t1}, are optimized to minimize the insertion loss, S_{21}, from $WR_{1.5}$ to the SBQ slot waveguide.

In Fig. 4.6(a), the distribution of the absolute value of the electric field, $\left|\vec{E}\right|$, is plotted over the cross sections, xy planes, of the three waveguides (A: $WR_{1.5}$, B: SBQ channel,

and C: SBQ slot waveguides), each operating at 530 GHz. Fig. 4.6(b) shows the scattering parameters of this transition; from the fundamental mode of $WR_{1.5}$ to each of the first three modes of the SBQ slot waveguide. By examining these scattering parameters, it can be seen that coupling from the first mode of the $WR_{1.5}$ to the first and third modes of SBQ slot waveguide are below -40 dB, and the reflection to the $WR_{1.5}$ is below -25 dB. Fig. 4.6(c) shows that the coupling from the $WR_{1.5}$ to the second mode of the SBQ slot waveguide is better than -0.8 dB, over the 500 to 600 GHz frequency range. It should be mentioned that this is the mode of the SBQ slot waveguide demonstrating the greatest confinement of the electric field inside the slot region.

4.1.2 THz SBQ Slot Waveguide: Fabrication

The fabrication process for the SBQ slot waveguide is almost the same as that of the SBQ channel waveguide, presented in Section 3.2, however, they differ in terms of the optical lithography step for patterning the photoresist. Using an optical lithography process for the SBQ slot waveguide is more challenging than that for the SBQ channel waveguide; particularly with regards to the taper connecting the channel waveguide to the slot waveguide. In the taper between the two waveguides, the gap is only $g = 5$ μm, a small dimension to fabricate using the optical lithography process.

First, the recipe used to pattern the photoresist for the SBQ channel waveguide is used for the SBQ slot waveguide. In order to avoid the photoresist sticking to the mask during the optical lithography process, a few pieces of silicon, 150 μm thicker than the actual SBQ pieces sample, are loaded as well. The result is shown in Fig. 4.7(a); the pattern resolution is not enough to achieve the narrow gap in the taper section. This low resolution pattern is due to the large distance between the photoresist and the mask during the exposure. Using thinner adjacent pieces should resolve the problem. However, at the time of fabrication, adjacent pieces with an accurate thickness were not available. So, the same available adjacent pieces were used for alignment purposes. To avoid alignment error, these pieces were removed from the stage very slowly, right before the exposure. The result is shown in Fig. 4.7(b), which has a high resolution in the photoresist pattern.

Figure 4.8(a), (b) and (c) show the optical microscope images of the patterned photoresist of: the tapered section of the SBQ channel waveguide, the taper section between the SBQ channel and slot waveguides, and a segment of the SBQ slot waveguide, respectively. The optical microscope images of the final device (after etching the silicon and cleaning the photoresist) are shown in Fig. 4.8(d), (e) and (f). These illustrate the taper section between the channel and slot waveguides, section of slot waveguide, and zoom in of the gap

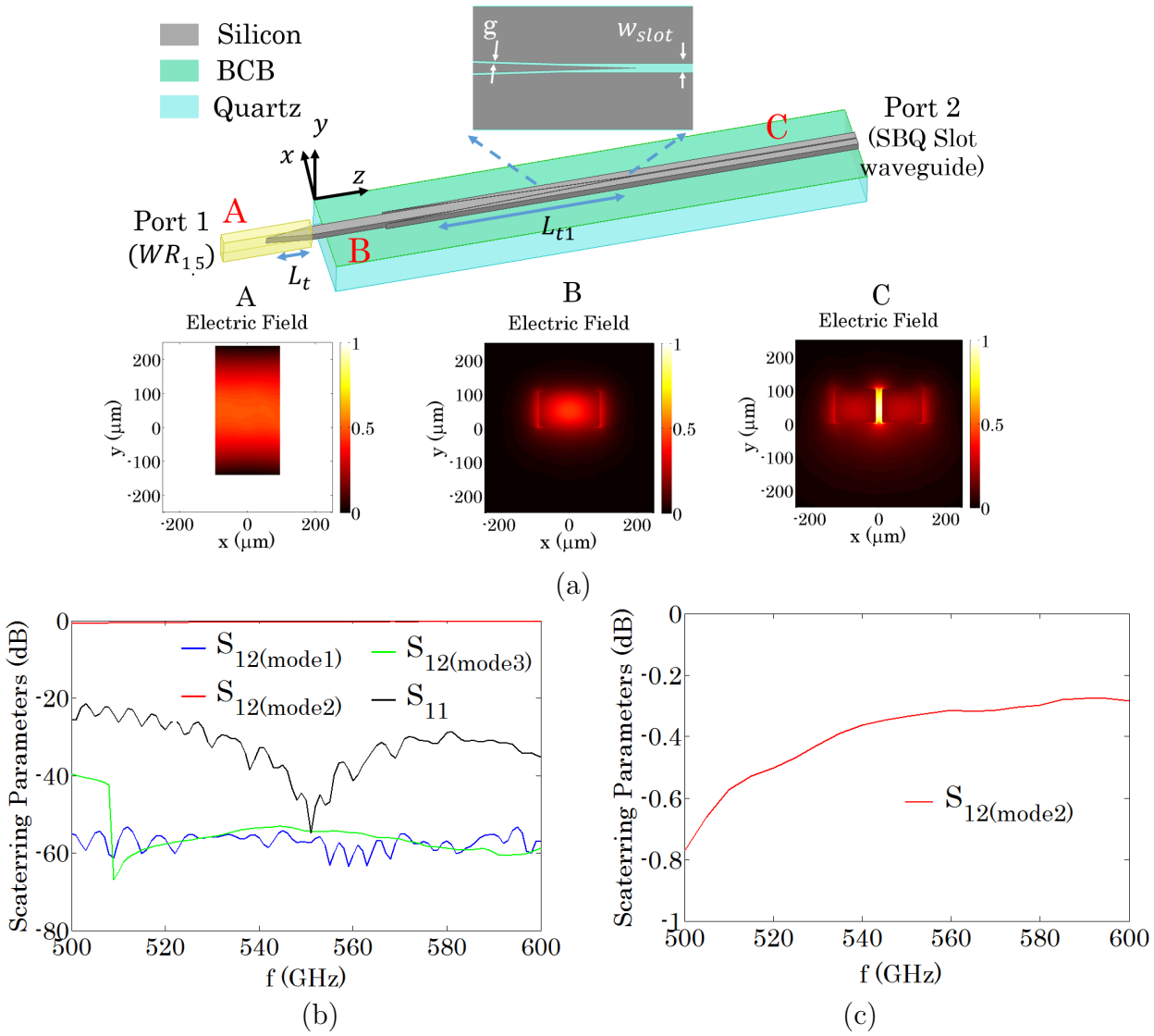

Figure 4.6: (a) Transition from $WR_{1.5}$ waveguide to SBQ channel waveguide (taper length of $L_t = 0.75$ mm), and transition from SBQ channel waveguide to SBQ slot waveguide (taper length of $L_{t1} = 3$ mm), $w_{slot} = 20$ μm, $g = 5$ μm. (b) Scattering parameters between the first mode of the $WR_{1.5}$ waveguide and first three modes of the SBQ slot waveguide. (c) Coupling from the first mode of the $WR_{1.5}$ to the second mode of the SBQ slot waveguide.

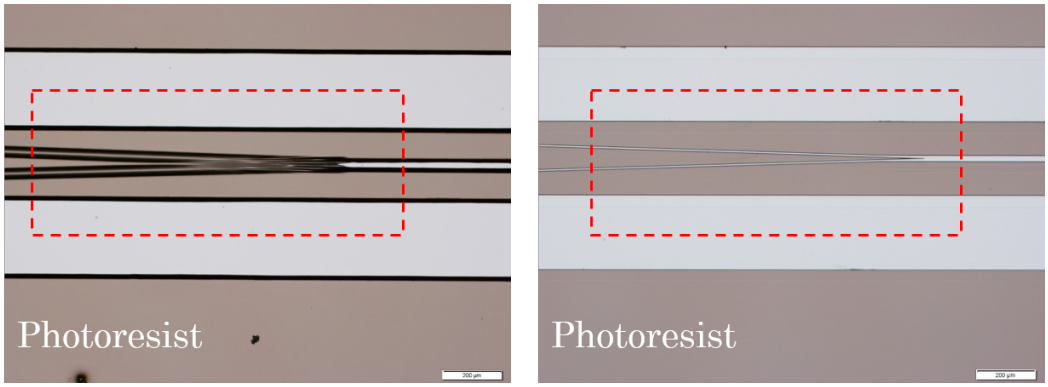

(a) (b)

Figure 4.7: Photoresist pattern for the taper from the channel waveguide to the slot waveguide; (a) Low resolution (unclear) photoresist pattern, (b) High resolution (clear) photoresist pattern.

of the slot waveguide, respectively. The target value for the slot width in the slot waveguide and the total width of the slot waveguide, are 20 and 260 μm, respectively. Fabrication results for these dimensions were 21.5 and 259.7 μm, as shown in Fig. 4.8(e) and (f), respectively. The optimized value for the gap between the slot and channel waveguides in the taper section was 5 μm, the fabrication result for this dimension was 5.34 μm.

4.1.3 THz SBQ Slot Waveguide: Measurement

Two SBQ slot waveguides, with lengths of $L_1 = 5.6$ mm and $L_2 = 9.6$ mm, were fabricated. In each of these waveguides, tapers to the SBQ channel waveguides on both sides were included. In addition, the channel waveguide was tapered as a transition to the metallic rectangular waveguide, $WR_{1.5}$, on both sides (shown in Fig. 4.9).

The setup used to measure the slot waveguides is the same as that used to measure the performance of the SBQ channel waveguide (shown in Fig. 3.12(a)). The device, with the schematic shown in Fig. 4.9, connects two $WR_{1.5}$ waveguides. The scattering parameters, S_{21} and S_{11}, measured between the two $WR_{1.5}$ waveguides, are shown in Fig. 4.10(a), for both lengths of slot waveguide. The average of S_{21} over the 500 to 570 GHz frequency range is -2.8 dB and -3.37 dB, for L_1 and L_2 respectively.

The loss of the SBQ slot waveguide was extracted from the measurement results of two waveguides with different lengths using the method presented in Section 2.3.1. Using this

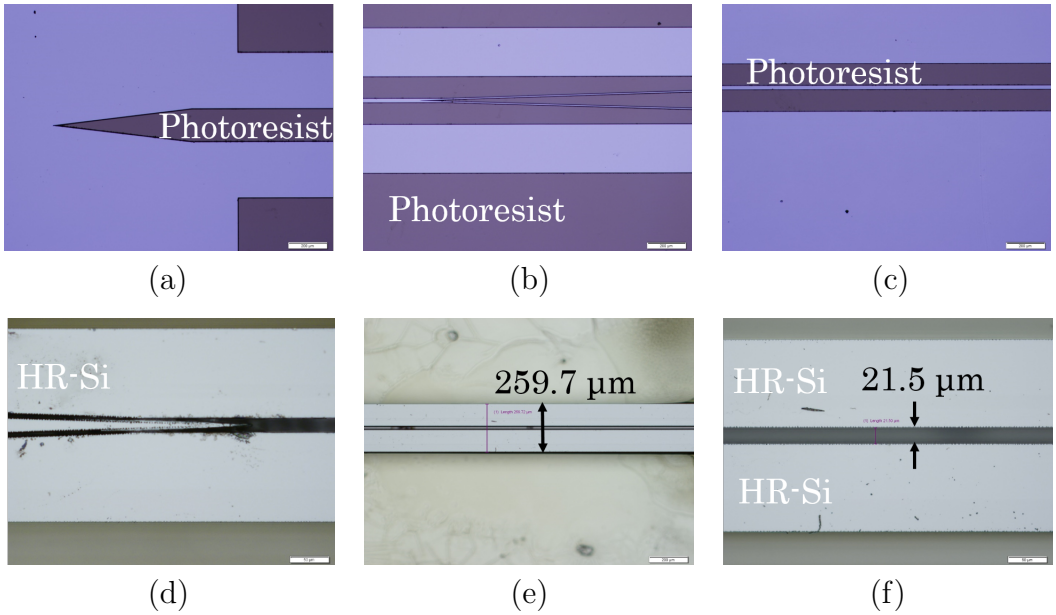

Figure 4.8: Optical microscope images of the photoresist pattern of: the tapered SBQ channel waveguide (a), taper section between the SBQ channel and slot waveguides (b), and segment of the SBQ slot waveguide. Images of the final device after etching the silicon and cleaning the photoresist, taper section between the SBQ channel and slot waveguides (d), section of the SBQ slot waveguide (e), and zoom into the gap region of the SBQ slot waveguide (f).

approach, the effects of the transitions between $WR_{1.5}$ and SBQ channel waveguides and, the transitions between the SBQ channel and slot waveguides were removed. The resulting attenuation constant of the SBQ slot waveguide is shown in Fig. 4.10(b). The average of the attenuation constant over the 500 to 570 GHz frequency range was found to be 0.16 $\frac{\text{dB}}{\text{mm}}$.

Figure 4.10(b) shows the simulation results for the attenuation constant of the second mode of the SBQ slot waveguide, for both $\sigma = 0.05$ $\frac{\text{S}}{\text{m}}$ and $\sigma_2 = 0.42$ $\frac{\text{S}}{\text{m}}$ assumed as the HR-Si conductivity. The averages of these simulation results over 500 to 570 GHz are 0.04 $\frac{\text{dB}}{\text{mm}}$ and 0.17 $\frac{\text{dB}}{\text{mm}}$ for σ and σ_2 respectively. Although assuming a higher conductivity for HR-Si provides a similar average attenuation constant in simulation and measurement, it should be noted that inaccuracy in the material parameters used for quartz and BCB in the simulation could be the reason of the discrepancy between simulation and measurement results. Specifically, in Fig. 4.6, comparing the absolute value of the electric field over

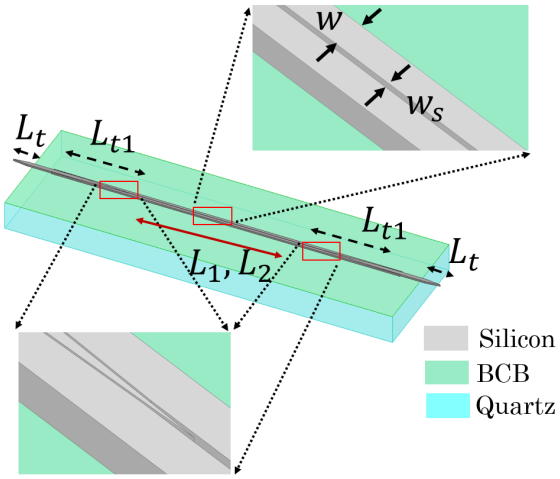

Figure 4.9: Schematic of back-to-back structure fabricated for characterizing the SBQ slot waveguide. $L_t = 0.75$ mm, is the transition between $WR_{1.5}$ and SBQ channel waveguides. $L_{t1} = 3$ mm, is the transition between the SBQ channel and slot waveguides. Lengths of the slot waveguides are $L_1 = 5.6$ mm and $L_2 = 9.6$ mm. $w = 120$ μm, $w_s = 20$ μm.

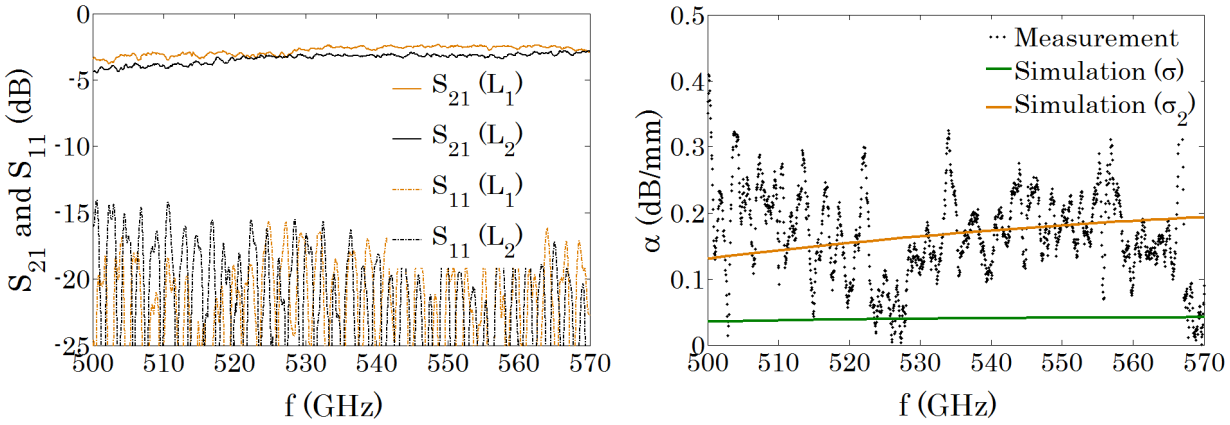

(a) (b)

Figure 4.10: (a) Scattering parameters, S_{21} and S_{11}, measured between two $WR_{1.5}$ waveguides (connected by the device with schematic shown in Fig. 4.9), for both lengths of SBQ slot waveguide ($L_1 = 5.6$ mm and $L_2 = 9.6$ mm). (b) Attenuation constant of SBQ slot waveguide extracted from measurement results.

the cross section of the channel and slot waveguides (B and C), field penetration into the substrate material is more in the slot waveguide. Therefore, if a higher loss be assumed for the substrate material, it is expected that the loss of the slot waveguide to be increased more than that in the channel waveguide.

The error due to the misalignments during measurements was studied in Section 2.3.2. Based on the results presented in that section, the maximum value of the error, averaged over 500 to 570 GHz, among the studied misalignment cases is 0.092 dB. Considering the length difference between the two SBQ slot waveguides (4 mm), the maximum tolerance in the extracted waveguide attenuation constant is $\frac{0.092}{4} = 0.023\ \frac{\text{dB}}{\text{mm}}$. Therefore, the precise presentation of the measured average attenuation constant of the SBQ slot waveguide is $0.16 \pm 0.023\ \frac{\text{dB}}{\text{mm}}$. The tolerance in this measurement can be reduced by using a longer length difference between two SBQ slot waveguides, and by improving the measurement setup for better alignment. A more accurate measurement setup is under development and not available at the time that these measurements were performed. The measurement setup improvement is listed among the future work of this thesis.

4.2 THz Slot Plasmonic Waveguide Based on Doped-GaAs

Plasmonic waves, essentially couplings between electromagnetic waves and the collective oscillations of free electrons of a metal, have attracted attention as useful for many applications including sensing [91–94] and enhanced spectroscopy [95–99]. Integrated plasmonic devices can lead to synergies between optics and electronics and there has been a significant amount of progress made in developing individual plasmonic building blocks [100–104]. One of the main components within an integrated plasmonic device is a plasmonic waveguide. Plasmonic waveguides support highly confined modes, and to date, several plasmonic waveguide structures have been proposed [105–109].

An optical plasmonic slot waveguide, which is made of a slot in a thin metallic film, has been investigated recently and provides highly confined fields in the slot region [110–112]. This type of plasmonic waveguide transmits most of the energy through the air in a deep-subwavelength area of the waveguide cross section.

The extension of optical plasmonic device concepts to the THz range of frequencies is quite challenging. Metals (e.g. gold and silver) support plasmonic waves at optical frequencies because they have small and negative real part of permittivity at THz range of

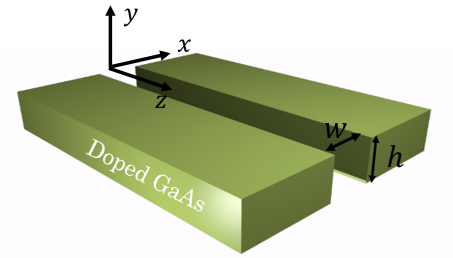

Figure 4.11: Doped-GaAs THz slot plasmonic waveguide ($w = h = 30$ μm).

frequencies. At THz spectrum, the permittivity of metals are very large; therefore, electromagnetic waves cannot penetrate into the metal and plasmonic mode cannot be supported. In order to have plasmonic modes at THz frequencies, highly doped semiconductors (e.g. GaAs, silicon, InP) could be used as the plasmonic material [113–119].

In this section, a THz plasmonic slot waveguide based on doped-GaAs is proposed and analyzed, Fig. 4.11. GaAs was chosen as the plasmonic material because it has higher electron mobility as compared to other semiconductors [120]. In Section 4.2.1, the modelling of GaAs using the Drude model is presented. Then, in Section 4.2.2, simulation results of the proposed waveguide are presented.

4.2.1 Doped-GaAs Modeling

Doped-GaAs can be effectively modeled by Drude theory [119, 121]:

$$\varepsilon(\omega) = \varepsilon_\infty + \frac{j\sigma}{\omega\varepsilon_0} \tag{4.3}$$

in which ε_∞ is the high frequency limit for the permittivity of GaAs, ε_0 is the vacuum permittivity, and ω is the angular frequency. The conductivity of GaAs, σ, can be derived from [119, 121]:

$$\sigma = \frac{10^6 N e^2 \tau / m^*}{1 - j\omega\tau} \tag{4.4}$$

$$\tau = \frac{m^* \mu}{e} \tag{4.5}$$

in Eq. 4.4, N is the carrier density, and m^* is the electron effective mass, τ is the carrier relaxation time, and μ is the carrier mobility, which is a function of the carrier density. For GaAs [120]:

$$m^* = 1.39 \times 10^{-32}\,[kg] \tag{4.6}$$

$$\varepsilon_\infty = 10.89\varepsilon_0 \tag{4.7}$$

For n-doped GaAs, the carrier mobility can be derived from the empirical formula [122]:

$$\mu = \frac{0.94}{1 + \sqrt{10^{-17} N}} \tag{4.8}$$

As the absolute value of the real part of the permittivity increases, field penetration into the GaAs will decrease. This also result in the loss decreasing. A smaller imaginary part of the permittivity will result in lower loss as well. Therefore, to minimize material loss, an optimum carrier concentration level should be considered which minimizes the ratio of $\left|\frac{\varepsilon''}{\varepsilon'}\right|$ [known as the dielectric loss tangent, $\tan(\delta)$]. In Fig. 4.12(a), this factor is shown as a function of the carrier concentration, at $f = 530$ GHz. Here, the optimum value for the carrier concentration is $N = 0.3 \times 10^{17}$ cm^{-3}. Fig. 4.12(b) and (c) show the real and imaginary parts of the permittivity of GaAs with the optimum carrier concentration as a function of frequency.

4.2.2 Simulation of the THz Slot Plasmonic Waveguide

The structure of the proposed THz plasmonic slot waveguide is shown in Fig. 4.11. It is basically a slot in the middle of a GaAs layer. The layer thickness and slot width are are $w = h = 30$ μm. For simplicity, a symmetrical waveguide was considered, in which the GaAs layer is supposed to be free standing in air. Permittivity values, shown in Fig. 4.12(b) and (c), were assumed for GaAs in the simulations. The Finite Element numerical method (FEM) of COMSOL Multiphysics software was used for the simulations.

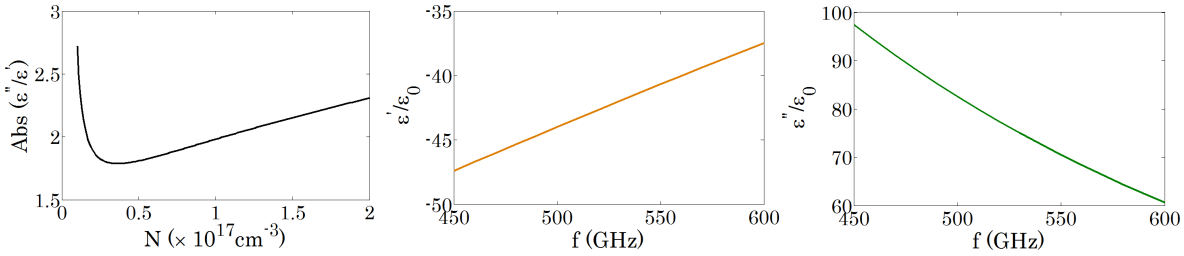

(a) (b) (c)

Figure 4.12: (a) Loss tangent ($\left|\frac{\varepsilon''}{\varepsilon'}\right|$) of GaAs as a function of its carrier concentration at 530 GHz. (b) and (c) are real and imaginary parts of the relative permittivity of GaAs, respectively, with the optimum carrier concentration, $N = 0.3{\times}10^{17}$cm^{-3}.

In Fig. 4.13 and Fig. 4.14, field plots of the first two modes of the proposed THz plasmonic slot waveguide are presented. As shown in Fig. 4.13, the fields of the first mode are confined in the deep-subwavelength slot region ($w \times h = 30\ \mu\text{m} \times 30\ \mu\text{m} = \frac{\lambda_0}{19} \times \frac{\lambda_0}{19}$ at $f = 530$ GHz, wherein λ_0 is the free space wavelength).

In Fig. 4.15(a), the normalized propagation constants of the first and second modes are shown. The propagation constant is larger than the free space wavenumber (k_0), so these modes are bounded (non-radiative). The normalized propagation constants increase with frequency; mainly due to the fact that the absolute value of the permittivity of GaAs decreases with frequency [Fig. 4.12(b) and (c)]. Therefore, for higher frequencies, a larger portion of the mode power will be inside the GaAs, so the normalized propagation constant (effective refractive index) will increase.

The attenuation constant of a plasmonic waveguides is usually expressed in terms of the propagation length, defined as the length over which field amplitudes would be reduced by a factor of e (Neper number). Denoting the complex wavenumber of the mode by $\beta + \text{j}\alpha$, then the propagation length is given by:

$$L_p = \frac{1}{\alpha} \tag{4.9}$$

Figure 4.15(b) shows the propagation lengths for the first two modes of the proposed waveguide versus frequency. It shows that the propagation lengths decrease with frequency. This is because at higher frequencies the absolute value of GaAs permittivity is smaller [Fig. 4.12(b) and (c)], so the percentage of the mode power inside the GaAs will increase and consequently the loss will also increase. Higher loss means shorter propagation length. The propagation length of the first mode at $f = 530$ GHz, is $L_p = 1.03\ \mu$m, equivalent to $8.7\ \frac{\text{dB}}{\mu\text{m}}$. The loss of this waveguide is three orders of magnitude higher than that of the waveguides based on HR-Si, and this fact limits the length of the waveguide.

Figure 4.16 shows the normalized propagation constants and propagation lengths as a function of the slot width w, for slot heights of $h = 20$ and $30\ \mu$m, for the first two modes of the proposed THz plasmonic waveguide. The normalized propagation constants increase as the slot width decreases. This is due to the fact that for smaller slot widths the percentage of the mode power inside the GaAs increases. In addition, the propagation length decreases with smaller widths w. The effect of slot height, h, on the normalized propagation constant is minimal, as shown in Fig. 4.16(a). However, as shown in Fig. 4.16(b), decreasing the slot height, h, decreases the propagation length, L_p.

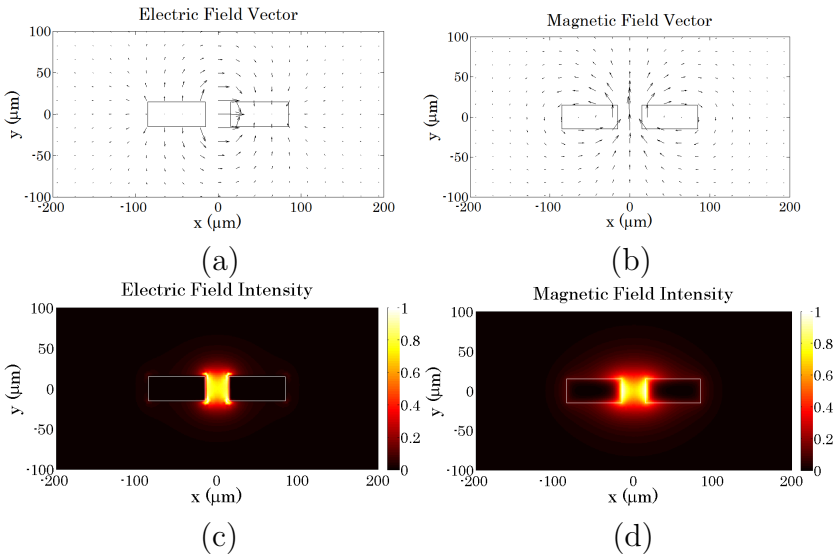

Figure 4.13: (a) and (b): Vector plots of the electric and magnetic fields of the first mode, respectively. (c) and (d): Intensity plots of the electric and magnetic fields of the first mode, respectively.

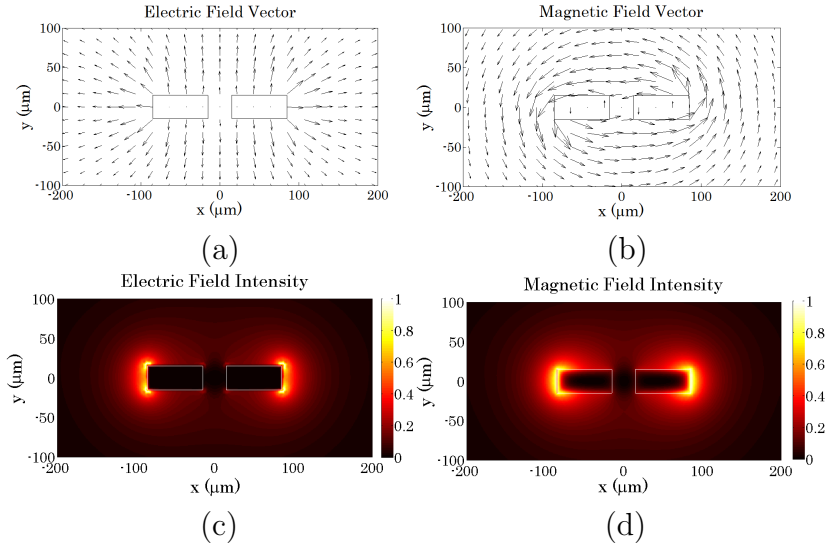

Figure 4.14: (a) and (b): Vector plots of the electric and magnetic fields of the second mode respectively. (c) and (d): Intensity plots of the electric and magnetic fields of the second mode, respectively.

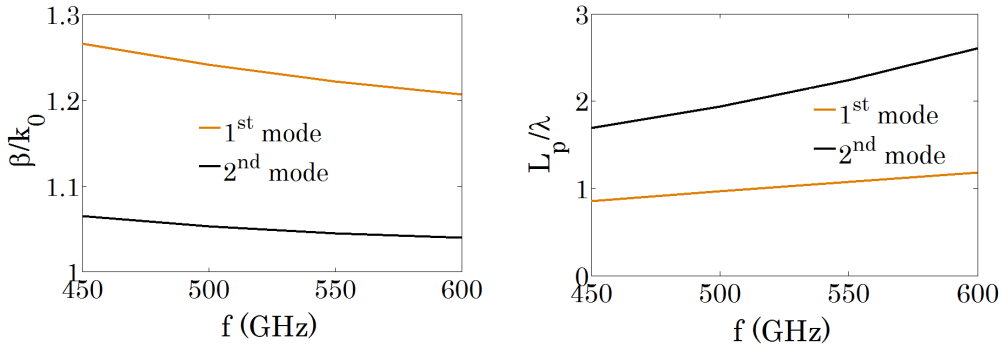

Figure 4.15: (a) Normalized propagation constants of the first two modes of the THz slot plasmonic waveguide (k_0 is the free space wavenumber). (b) Propagation lengths of the first two modes of the THz slot plasmonic waveguide, normalized to the free space wavelength.

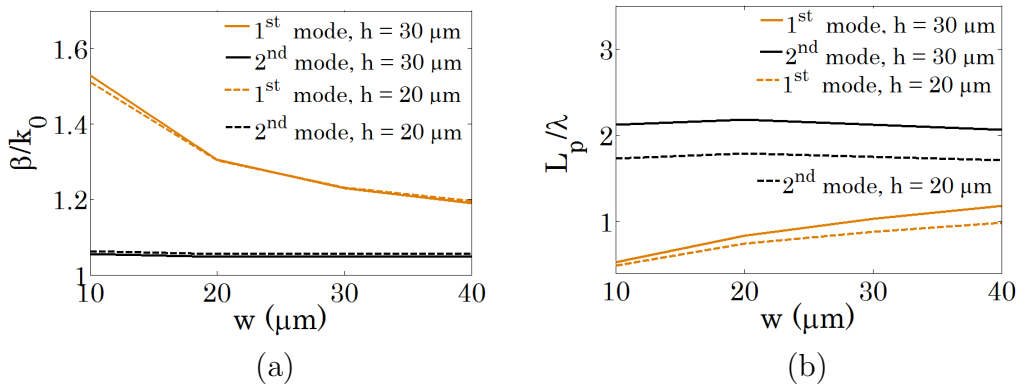

Figure 4.16: (a) and (b) are normalized propagation constants and propagation lengths, respectively, for the first two modes of the THz slot plasmonic waveguide, versus slot width, w, for slot heights $h = 20$ and 30 μm.

Smaller slot dimensions are preferred as they result in higher mode confinement. But, as Fig. 4.16(b) shows, the waveguide loss would increase as well. There is a trade-off between mode confinement and waveguide loss. As can be seen in Fig. 4.16(b), the propagation length does not increase significantly (and the loss does not decrease significantly) for dimensions larger than $w = 30$ μm.

The investigated THz plasmonic waveguide has a symmetric structure; a free standing layer of GaAs with a slot region and the same medium below and above the GaAs layer (air). For experimental investigation and validation of the proposed waveguide, a proper

substrate will be required, resulting in an asymmetrical structure. To provide a practical waveguide structure, a quartz substrate bonded to the GaAs layer using a thin BCB adhesive layer is proposed. Such an asymmetric waveguide structure has been studied theoretically with results published in [71]. Those findings will not be presented here, in an effort to maintain the cohesiveness of this thesis. However, it is worth mentioning that in the asymmetric case, the leaky surface plasmon waves propagating at the interface of the GaAs layer and the quartz substrate must also be considered as a part of the spectrum of the modes supported by the waveguide. To avoid these leaky waves an upper limit should be imposed on the width of the slot region (presented in [71]).

4.3 Conclusions

In this chapter, two slot waveguides for THz field confinement have been proposed and analysed. The SBQ THz slot waveguide was fabricated and its low-loss characteristics were verified experimentally. As compared to the THz SBQ slot waveguide, the proposed THz plasmonic slot waveguide has higher losses by three orders of magnitude, limiting the practicality of this waveguide.

In the plasmonic waveguide, the slot dimensions were $w = h = 30\ \mu$m, and the waveguide mode was confined in a $\frac{\lambda_0}{19} \times \frac{\lambda_0}{19}$ region at $f = 530$ GHz, with λ_0 being the free space wavelength. Comparing these modal field dimensions with those of the SBQ slot waveguide ($\frac{\lambda_0}{6} \times \frac{\lambda_0}{28}$ for an electric field at the same frequency), the plasmonic slot waveguide provided deep-subwavelength confinement in both directions of the waveguide cross section, for both electric and magnetic fields. While decreasing the slot height of the THz SBQ slot waveguide would increase the waveguide's cutoff frequency, the plasmonic slot waveguide maintained its confined propagating mode, even with the deep-subwavelength dimensions of the slot region, both in height and in width, due to the different guiding mechanism (plasmon resonances).

A more quantitative comparison of the field confinement of these two waveguides requires a figure of merit. In the next chapter, focused on the use of THz waveguides for absorption spectroscopy, a figure of merit is defined and the field confinements of the proposed waveguides are compared based on this figure.

Chapter 5

Terahertz Absorption Spectroscopy

5.1 Introduction

Absorption spectroscopy is a spectroscopy technique that measures the absorption of electromagnetic wave radiation as a function of frequency, due to its interaction with a material sample. This spectroscopy method is used as an analytical chemistry tool to determine the presence of a particular substance in a sample and, in some cases, to quantify the amount of the substance. Some materials have absorption peaks, called absorption signatures, at specific frequencies. These absorption signatures are typically classified according to the nature of the change induced in the sample when interacting with electromagnetic waves at those specific frequencies. Rotational absorption lines refer to the absorption of electromagentic waves due to change in the rotational state of molecules, typically found in the microwave spectral range. Vibrational absorptions correspond to changes in the vibrational state of molecules and typically happen in the infrared (IR) range. Electronic absorption lines are produced from changes in the electronic state of the atoms or molecules and typically occur in the visible and ultraviolet ranges. In the mid-IR range of frequencies, corresponding to wavelengths of 2.5 to 25 μm, absorption is caused by both molecular vibrations and rotational vibrations. The IR spectrum contains information about the molecular structures, the strength and the orientation of chemical bonds, and the rotational states of the molecules. As an example, Fig. 5.1(a) shows the vibrational and rotational modes of a water molecule, and Fig. 5.1(b) shows macromolecular dynamics (stretching, bending, and torsional vibration) [1]. When a beam of IR waves passes through a sample and its frequency is the same as the vibrational frequency of a chemical bond, absorption occurs. IR absorption spectroscopy is a simple and reliable technique widely used for the identification

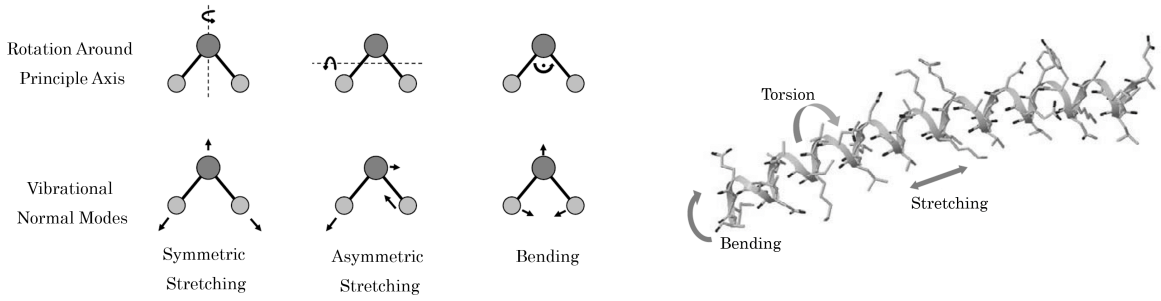

Figure 5.1: (a) Rotational and vibrational modes of a water molecule [1], (b) Macromolecular dynamics: stretching, bending, and torsional vibrations [1].

of organic and inorganic compounds, polymers, and biological samples [123].

THz absorption spectroscopy measures the spectrum of the material over the THz range of frequencies, 300 GHz to 3 THz. A common question about THz absorption spectroscopy, is how the information provided by this new spectroscopy method is different from that provided by the much more mature IR absorption spectroscopy technique. A unique charachteristic of THz absorption spectroscopy is its ability to observe intermolecular vibrations in some chemical and organic molecules [22]. In these materials, the intramolecular modes appear in the IR range, but the intermolecular modes fall within the THz gap. The study of these intermolecular vibrations has shed light on the dynamics of large biomolecules [22, 124, 125]. As an example, Fig. 5.2 shows changes in the absorption spectrum of barbital (a hypnotic drug) after heat treatment, in both the THz and IR frequency ranges [22]. As shown in this figure, a difference in the spectrum at the THz range is clear, while change in the IR range is not apparent.

Common explosives, such as RDX, HMX, PETN, and TNT, have unique spectral signatures in the THz gap [3–5, 126–128]. Fig. 5.3 shows the signatures of RDX in the THz gap and their chemical structures [3]. These materials exhibit strong radiation absorption at certain THz frequencies making it possible to differentiate them from typical covering materials such as clothing and plastic that are almost transparent at THz frequencies. So absorption spectroscopy could be used for security inspection of closed/sealed packages.

Applications of the absorption spectroscopy can be divided into two main categories:

1. **Material Characterization:** in which the objective is to determine the absorption signature of a material under test. This could be applied to study the molecular

structure of a material or to detect the state of a specific material using the potential shift in its signature frequency of absorption (similar to the case of barbital, Fig. 5.2).

2. **Concentration Sensing:** in which the objective is to determine the concentration of a target material in a mixture using its absorption signature. In general, the peak absorption of the target material is a linear function of its concentration in a mixture. This is a highly selective method of material sensing due to the fact that each material has its own signature frequencies of absorption peaks.

In the IR frequency range, sensing the concentration of a target material using absorption signatures has reached a sensitivity below parts-per-million (ppm). But in the THz frequency range, to date, absorption spectroscopy is mostly used for material characterization applications.

5.1.1 Conventional Setup for THz Absorption Spectroscopy

Figure 5.4 shows the conventional setup for THz absorption spectroscopy. More details of this setup can be found in [1]. In this setup a femto-second laser is used to generate and detect THz pulses. The optical beam is split into two parts, called probe and pump. The probe beam passes through a translational stage to provide a relative time delay. The pump signal illuminates the emitter in which the THz pulse will be generated. The generation of THz pulses is performed by either transient currents in a photoconductive antenna or optical rectification in a nonlinear optical crystal. The THz pulse passes through the sample under test and then is focused onto the detector. The time profile of the transmitted pulse through the sample is compared with the reference pulse (i.e. the transmitted pulse when the sample is absent). The frequency spectrum of the reference pulse and the pulse transmitted through the sample are obtained from Fourier transform analyses. This provides the spectroscopic information about the sample under investigation, including its absorption signatures.

Although it has been extensively used for THz absorption spectroscopy during the past few decades, the conventional setup as described has several limitations. Firstly, it requires a large amount of material under test to achieve a measurable interaction between the material and the THz wave. The focusing of the THz wave on the sample in a free space configuration is limited by the diffraction limit, so the sample must have a large enough size to have sufficient interaction with the electromagnetic wave. Secondly, the interaction length between the beam and material sample is limited by the setup; therefore, using this

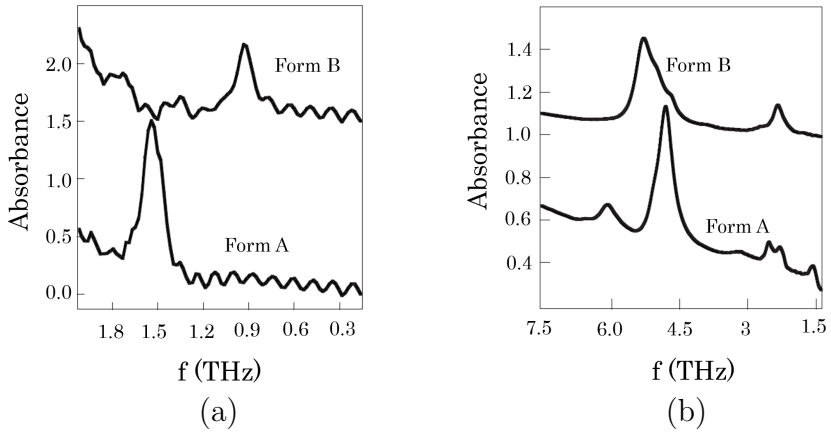

Figure 5.2: Absorption spectrum of barbital in the THz (a), and IR (b), frequency ranges. Form A is the original barbital, Form B is after heating at 160 °C for 30 min [22].

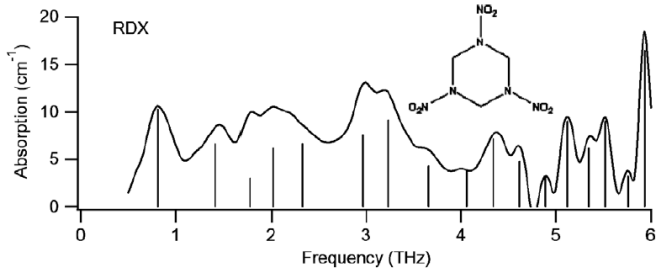

Figure 5.3: Signatures of RDX in the THz frequency range and its chemical structure [3].

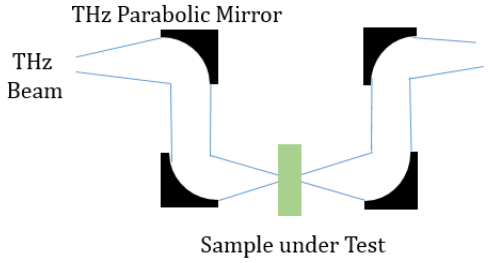

Figure 5.4: Conventional THz spectroscopy setup.

setup, weak absorption signatures cannot be captured. Thirdly, achieving a high signal-to-noise ratio (SNR) is challenging, especially due to limited source power and water vapor

absorption lines in the THz gap. Finally, it is a bulky setup, not appropriate for many commercial applications.

5.1.2 THz Absorption Spectroscopy using Metallic Waveguides

Waveguide-based THz spectroscopy, in which the THz signal passes through a waveguide while interacting with the sample, has many advantages over the free space setup. Firstly, a smaller amount of sample is required. In contrast to the conventional free space setup, in a waveguide-based configuration the waveguide modal field distribution with sub-wavelength features interacts with the sample; therefore, a sub-wavelength sample could interact with the entire mode power. Secondly, since the wave is propagating inside the waveguide, a better SNR is achievable compared with that in the free space setup.

In the THz frequency range, several metallic waveguides have been used for waveguide-based absorption spectroscopy. In [129], a THz single wire waveguide is used for this purpose, shown in Fig. 5.5. The test sample in [129], 1 mg of lactose powder, was dispersed over a 55 mm long single wire waveguide. As shown in Fig. 5.5(b), there is a dip in the amplitude of the transmitted THz signal at 530 GHz. It was possible to capture the absorption peak of the lactose with only 1 mg of sample, while in a free space measurement, 50 mg of the same sample is required to achieve a clear absorption peak [130].

In [131], a microstrip line is used for THz absorption spectroscopy, as shown in Fig. 5.6. The sample used in [131] is lactose powder, which has beencompressed into a pellet and then diced into a cube with dimensions of 1 mm $\times$ 1 mm $\times$ 0.5 mm. Fig. 5.6(b) shows the measurement results presented in [131].

Both the single wire waveguide and microstrip line measurement setups required considerably less of the sample substance than the free space spectroscopy setup. Comparing the measurement results of [129] and [131], shown in Fig. 5.5(b) and Fig. 5.6, the dip in the transmission through the waveguide around 530 GHz (the signature frequency of lactose) is much clearer for the single wire waveguide than the microstrip line. There are two reasons for this. Firstly, in the single wire waveguide most of the mode power is outside of the waveguide, while in the microstrip case a great percentage of the mode power is in the substrate. Therefore, the percentage of the mode power that interacts with the sample is higher in the single wire measurement compared to the microstrip-line case. Secondly, in the single wire case, the lactose powder is dispersed over a 55 mm long wire, while in the microstrip case, the length of the sample is only 1 mm.

Other metallic waveguides used for THz absorption spectroscopy are parallel plate waveguides [132, 133] and coplanar waveguides [134].

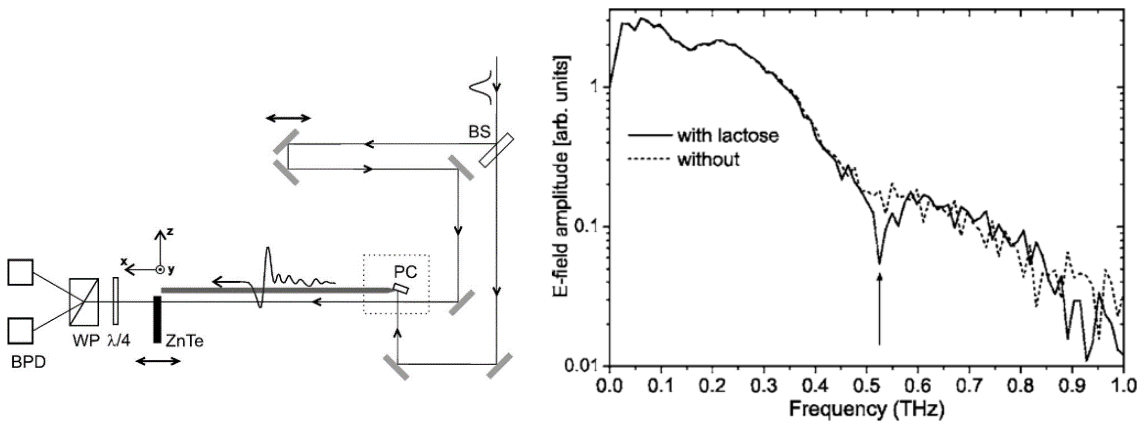

(a) (b)

Figure 5.5: (a) THz absorption spectroscopy using a single wire waveguide [129], (b) frequency spectra of THz pulses propagated along the wire with and without lactose [129].

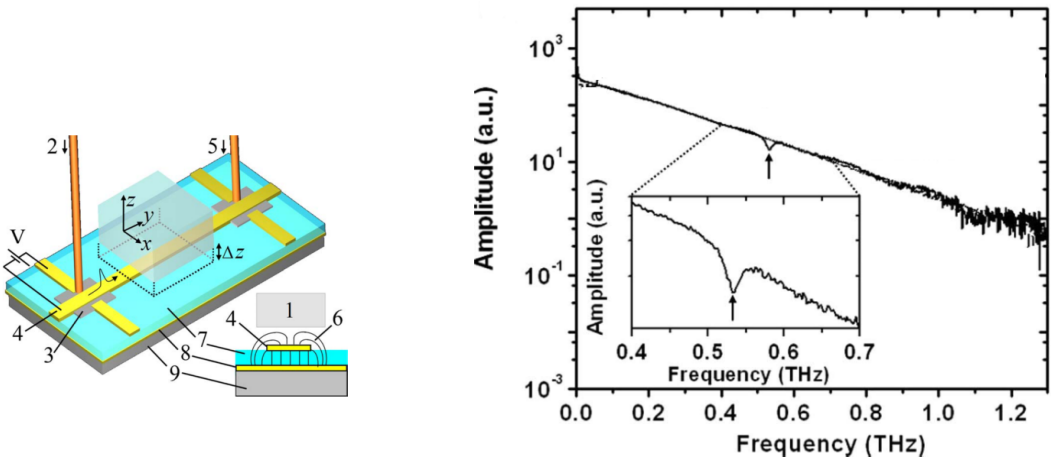

(a) (b)

Figure 5.6: (a) Microstrip line for THz absorption spectroscopy [131], (b) amplitude of transmitted THz wave through the microstrip line, with and without lactose [131].

5.1.3 Chapter Outline

The primary objective of this chapter is to investigate the performance of the proposed SBQ THz dielectric waveguide for THz absorption spectroscopy. The test sample used for this study is lactose powder, the same test sample used in the studies of metallic waveguides for spectroscopy (reviewed in reviewed in Section 5.1.2).

The absorption strength of a compressed powder is different from that of an uncompressed powder. For simplicity, uncompressed powder is used as the test sample in this study. As an initial step, it is necessary to investigate the absorption of the test material, particularly its measured absorption strength repeatability. For this, the the same measurement setup and absorption extraction method are repeated multiple times. In Section 5.2, a free space setup is used to investigate the absorption signature of the test sample. The absorption of the powder is extracted from the measurement multiple times, and the results are presented and discussed.

In Section 5.3, the application of THz dielectric waveguides for absorption spectroscopy is proposed and investigated. To investigative how the parameters of a waveguide affect the interaction between the waveguide mode and the surrounding material under test, a factor called interaction factor, is formulated in Section 5.3.1. This factor is calculated for the proposed THz waveguides using simulations, and presented in Section 5.3.2. Then, several devices based on the SBQ platform are designed, fabricated, and their applicability for waveguide-based absorption spectroscopy is investigated experimentally and presented in Section 5.3.3. The conclusions of this chapter are discussed in Section 5.4. In Section 5.4.1, the performances of the SBQ the THz waveguides and THz metallic waveguides are compared for absorption spectroscopy applications. Then, the sensitivity limits of an SBQ waveguide for concentration sensing of a target material in a mixture, based on molecular fingerprints, are presented in Section 5.4.2.

5.2 Free Space THz Absorption Spectroscopy

In the conventional free space setup for THz absorption spectroscopy, shown in Fig. 5.4, only the transmission through the sample is measurable. For accurate measurement of the absorption of a sample under test, it is essential to calibrate the reflections from the sample. In contrast to the conventional free space setup, a Network Analyzer provides all scattering parameters, including reflections from the sample; therefore, a material under test can characterised more accurately. This equipment has been extensively used in the

microwave frequency range for this purpose. The same setup recently became available for THz frequencies.

In [135], the setup shown in Fig. 5.7(a) was used to measure complex permittivity of several dielectrics at the 220 to 330 GHz frequency range. In [136], a similar setup was used to measure the real part of the permittivity of several dielectrics, up to 1.1 THz. The measured quantities in this setup are the scattering parameters between the rectangular waveguides, port 1 and port 2 in Fig. 5.7(a). The permittivity of the material under test is extracted from these scattering parameters. A collimated wave, which passes through the material under test between the two lenses [Fig. 5.7(a)], simplifies the extraction using analytic formulas as presented in [135, 136].

Instead of the setup shown in Fig. 5.7(a), a near-field setup, shown in Fig. 5.7(b), was used here for the free space absorption spectroscopy. The near-field setup has several advantages:

1. In a free space setup, the dimensions of the sample under test should be large enough in the plane perpendicular to the direction of propagation [i.e., xy plane in Fig. 5.7(a) and (b)] in order to avoid edge scattering. In the near-field setup, Fig. 5.7(b), since the antennas are close to each other, the beam spot size is small compared to that in the far-field setup, Fig. 5.7(a); therefore, a large sample size in the xy is not required. This was advantageous in our measurements due to limitation existed on the sample size.

2. In the near-field setup, Fig. 5.7(b), the horn antennas are close to each other and this provides a high SNR for the system, even without using lenses. A high SNR is especially critical when using the setup for absorption spectroscopy, in which the absorption of the material under test can reach high values at the signature frequencies (i.e., samples can be quite lossy). It should be mentioned that the samples characterized in [135] and [136] using the Fig. 5.7(a) setup were very low-loss, and therefore less challenges with regard to the SNR of the system.

3. Finally, the alignment in the near-field setup is easier because no component for wave-collimation is required.

Since the THz wave passing through the sample in the near-field setup, Fig. 5.7(b), is not a collimated beam, it could be challenging to accurately extract the parameters of the material under test from the scattering parameters between ports 1 and 2. In the next section, using Gaussian mode analysis, it is shown that the absorption of the material under test in this setup can be extracted from the scarring parameters even without a collimated wave. Then, the accuracy of the method is investigated using full-wave simulations.

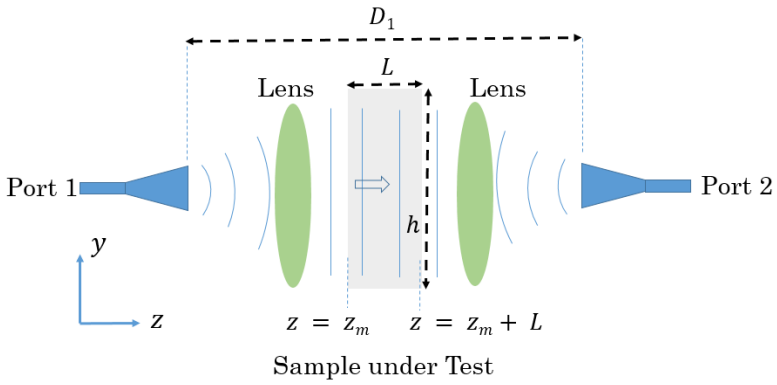

(a)

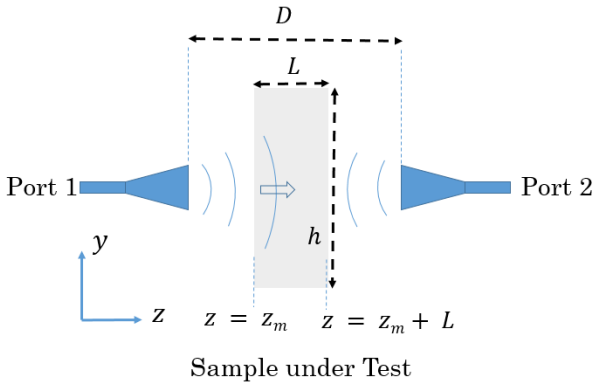

(b)

Figure 5.7: Schematic of free space setups for material characterization: (a) long path of collimated beam using lenses, and (b) short path without lenses.

5.2.1 Absorption Extraction Method

Waves for which the wavefront normals make small angles with the direction of propagation are called paraxial waves, and satisfy the paraxial Helmholtz equation [137]. A Gaussian beam, Eq. 5.1, is a scalar solution of the Helmholtz equation. The beam power is concentrated within a small cylinder around the beam axis.

$$U(\mathbf{r}) = A_0 \frac{W_0}{W(z)} e^{-\frac{x^2+y^2}{W^2(z)}} e^{-jkz - jk\frac{x^2+y^2}{2R(z)} + j\zeta(z)} \tag{5.1}$$

in which $W(z)$ is the beam radius and $R(z)$ is the beam wavefront radius.

$$W(z) = W_0(1 + (\frac{z}{z_0})^2)^{1/2} \tag{5.2}$$

$$R(z) = z(1 + (\frac{z_0}{z})^2)^{1/2} \tag{5.3}$$

$$\zeta(z) = tan^{-1}\frac{z}{z_0} \tag{5.4}$$

$$W_0 = (\frac{\lambda z_0}{\pi})^{1/2} \tag{5.5}$$

In Eq. 5.1, z_0 is called the Rayleigh range.

The output of a horn antenna could be approximately represented by a Gaussian beam [138, 139]. Assuming the interfaces of the material under test with wave propagating medium (air for example), are planar and perpendicular to the z-direction (Fig. 5.7(b)), the Gaussian beam parameters will not change inside the region of the material under test [137]. Assuming the transmission matrix between the rectangular waveguide mode, TE_{10}, and the Gaussian beam at $z = z_m^+$, as $\mathbf{T_T}$, and the transmission matrix between the Gaussian beam at $z = z_m + L^-$ and the rectangular waveguide mode, TE_{10}, as $\mathbf{T_R}$, the transmission matrix between the two rectangular waveguides can be written as:

$$\mathbf{T} = \mathbf{T_T}\mathbf{T_m}\mathbf{T_R} \tag{5.6}$$

in which, $\mathbf{T_m}$, is the transmission matrix between the Gaussian beam at $z = z_m^+$ and $z = z_m + L^-$. Multiple reflections of the incident wave occur inside the material under test, and the output from this material is the summation of all these waves. For materials under test with low real parts of relative permittivity, these multiple reflections are much smaller than the first term (Reflection from the interface between a material and air is $r = \frac{\sqrt{\varepsilon_r}-1}{\sqrt{\varepsilon_r}+1}$, in which ε_r is the real part of permittivity of the material. Considering the power instead of the field amplitude, and considering bouncing from two side walls of the material under test, the second term in the summation series of multiple reflections is smaller than the first term by a factor of r^4, which is less than 0.012 for $\varepsilon_r \leq 4$). Moreover, the wave passing through a lossy material sample makes these multiple reflections even weaker. Ignoring the multiple reflections, based on the complex amplitude expression for Gaussian beam, given in Eq. 5.1, $\mathbf{T_m}$ can be written as ($k = \beta - j\frac{\alpha}{2}$):

$$\mathbf{T_m} = \begin{bmatrix} A_1(x,y)A_2(x,y;\alpha)e^{j\psi(x,y;\beta)} & 0 \\ 0 & A_1^{-1}(x,y)A_2^{-1}(x,y;\alpha)e^{-j\psi(x,y;\beta)} \end{bmatrix} \tag{5.7}$$

in which:

$$A_1(x,y) = \frac{W(z_m^+)}{W(z_m+L^-)} e^{-(x^2+y^2)(\frac{1}{W^2(z_m+L^-)}-\frac{1}{W^2(z_m^+)})} \tag{5.8}$$

$$A_2(x,y;\alpha) = e^{-\frac{\alpha}{2}(L+\frac{x^2+y^2}{2R(z_m+L^-)}-\frac{x^2+y^2}{2R(z_m^+)})} \tag{5.9}$$

A_1 is representative of decay in the beam amplitude from its divergence, while, A_2 is decay due to the lossy material sample. All phase quantities are expressed as the $e^{j\psi(x,y;\beta)}$ term, altogether. At any z location, the majority of the Gaussian beam power is inside a circle with a radius of $W(z)$. Then, using Eq. 5.2, 5.3, and 5.5:

$$\frac{x^2+y^2}{2R(z_m+L^-)} - \frac{x^2+y^2}{2R(z_m^+)} < \frac{x^2+y^2}{2R(z_m+L^-)} < \frac{W(z_m+L^-)}{2R(z_m+L^-)} = \frac{L}{2\pi^2}(\frac{\lambda}{W_0})^2 \tag{5.10}$$

Therefore, if:

$$\frac{1}{2\pi^2}(\frac{\lambda}{W_0})^2 << 1 \tag{5.11}$$

then $A_2(x,y,\alpha)$ can be simplified as:

$$A_2(x,y;\alpha) = e^{-\frac{\alpha}{2}L} = A_2(\alpha) \tag{5.12}$$

Suppose the measurement is performed for a material with unknown absorption coefficient, α, and a reference material with known absorption coefficient α_0. Suppose the transmission matrix between the two rectangular waveguides is $\mathbf{T}$ and $\mathbf{T_0}$, for the unknown material and the reference material respectively. If the real parts of the relative permittivity of both materials are close, then the $\mathbf{T_T}$ and $\mathbf{T_R}$, transmission matrices between the horn antennas and the materials under test, are the same in the test of the unknown material and test of the reference material. Therefore:

$$\mathbf{T} = \mathbf{T_T T_m T_R} \tag{5.13}$$

$$\mathbf{T_0} = \mathbf{T_T T_{m0} T_R} \tag{5.14}$$

Then:

$$\mathbf{T T_0^{-1}} = \mathbf{T_T T_m T_R T_R^{-1} T_{m0}^{-1} T_T^{-1}} = \mathbf{T_T T_m T_{m0}^{-1} T_T^{-1}} \tag{5.15}$$

Using Eq. 5.7 and 5.12:

$$\mathbf{T_m T_{m0}^{-1}} = \begin{bmatrix} e^{-L(\frac{\alpha}{2}-\frac{\alpha_0}{2})} e^{-j(\psi(x,y;\beta_x)-\psi(x,y;\beta_0))} & 0 \\ 0 & e^{L(\frac{\alpha}{2}-\frac{\alpha_0}{2})} e^{j(\psi(x,y;\beta_x)-\psi(x,y;\beta_0))} \end{bmatrix} \tag{5.16}$$

Based on Eq. 5.15, $\mathbf{T T_0^{-1}}$ and $\mathbf{T_m T_{m0}^{-1}}$ have the same eigenvalues. $\mathbf{T}$ and $\mathbf{T_0}$ are the measured matrices, so the eigenvalues of $\mathbf{T_m T_{m0}^{-1}}$ are known. Based on Eq. 5.16, the real part of the eigenvalues of $\mathbf{T_m T_{m0}^{-1}}$ are $\pm L(\frac{\alpha}{2}-\frac{\alpha_0}{2})$. Therefore, the attenuation constant of the unknown material, α, can be calculated.

5.2.2 Simulation

As presented in the previous section, there are several approximations used in the absorption extraction method. To quantify the accuracy of the method, a full-wave simulation of the actual measurement setup is required.

The test sample used in this chapter is lactose powder. A sample holder is required. The flatness of the sample holder walls is critical to have the paraxial Gaussian beam maintain its propagation axis while passing through the sample holder. Another important consideration for the sample holder is that it should transparent in the frequency range of interest (it should have low permittivity and low loss). In [140], multiple polymers have been characterized in the THz frequency range and the results are shown in Fig. 5.8(a). As shown in this figure, polystyrene is an extremely low loss polymer in this frequency range and has a low permittivity (refractive indices are shown in Fig. 5.8(a)). Sample holders from Sigma Aldrich Inc maid of polystyrene, were used, shown in Fig. 5.8(b).

Full-wave simulation of the measurement setup was performed using HFSS simulator. The parameters of the available horn antennas for measurement were used in the simulations. The structure is electrically large (distance between ports 1 and 2 is more than $61\lambda_0$). To run the simulation more efficiently, the sample holder body was assigned as the Integral Equation (IE) region in HFSS simulator. By this assignment the IE region is not discretized volumetrically, only its surface is discretized.

Simulations were performed for two different assumption for the region inside the sample

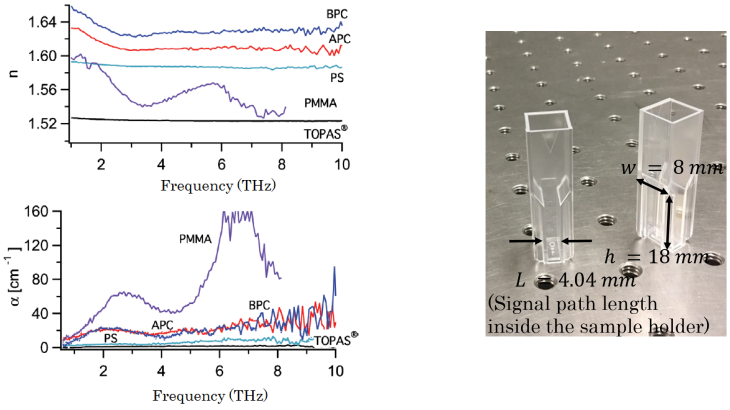

(a) (b)

Figure 5.8: (a) Several polymers characterized in THz frequency range [1], (b) Sample holders made of polystyrene (PS).

holder: a lossy material ($\varepsilon_{rx} = 3$ and $\alpha = 4.95$ $\frac{\text{dB}}{\text{mm}}$, at $f = 532$ GHz) and a reference material ($\varepsilon_{r0} = 3$ and $\alpha = 0$ (loss-less), at the same frequency). Fig. 5.9(b) and (c) show the simulation results for the magnitude of the electric field over a plane which cuts the structure in the middle in y-direction, for both material assumptions. The field magnitude at the side walls of the sample holder which (parallel to the yz plane) is significantly smaller than its maximum value at the center. This confirms that the sample holder is wide enough in the x-direction to avoid reflections from these side walls. The sample holder size in the y-direction is larger than in the x-direction; therefore, it can be concluded that the sample holder cross section (in xy plane) is large enough to avoid scattering from the edges.

Assuming S_x and S_0 are the scattering parameters between ports 1 and 2 for the lossy

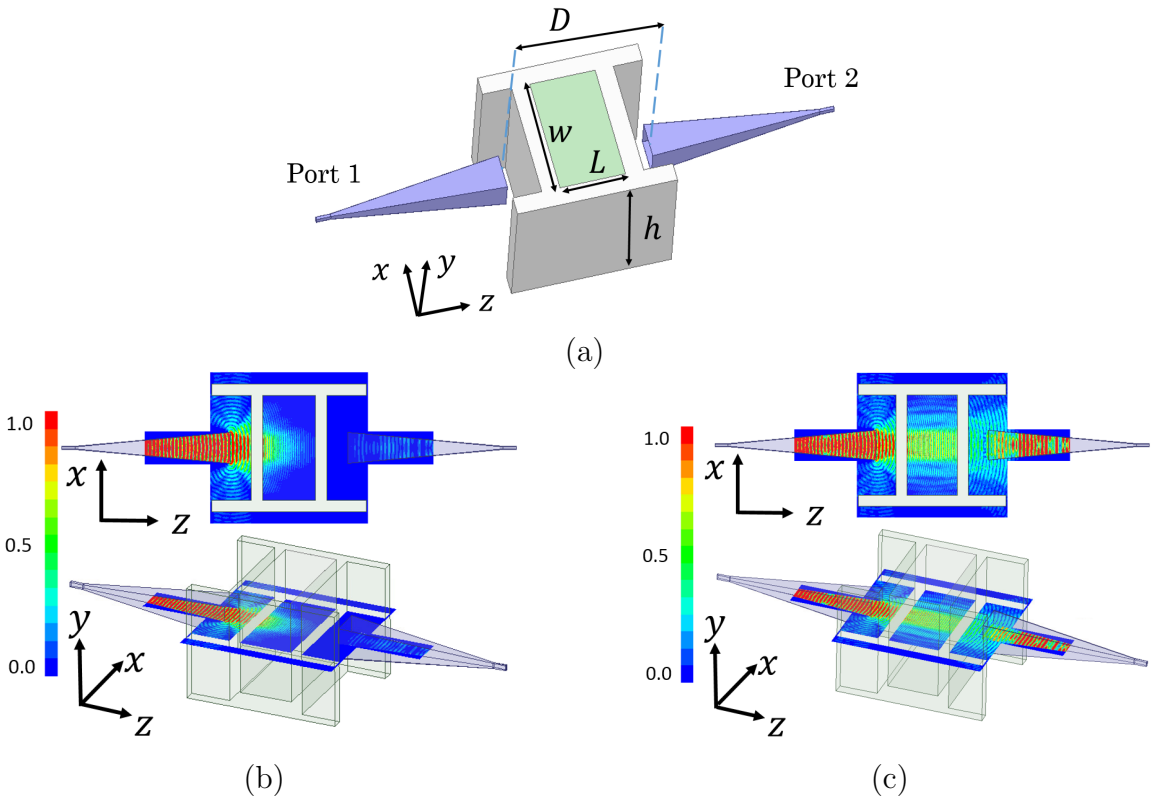

Figure 5.9: (a) Free space setup; including horn antennas and sample holder filled with the test sample, in the middle. $D = 9$ mm, $w = 8$ mm, $h = 9$ mm, $L = 4.04$ mm. (b) and (c) are the magnitude of the electric field when the sample holder is filled with the lossy material and the reference material, respectively.

and reference materials respectively, the following are the simulation results for these matrices (the magnitudes are in dB and the angles are in degrees).

$$S_x = \begin{bmatrix} -13.4 < 174 & -27.5 < 124 \\ -27.5 < 124 & -13.4 < 174 \end{bmatrix}, \; S_0 = \begin{bmatrix} -10.3 < -165 & -6.5 < 128 \\ -6.5 < 128 & -10.8 < -166 \end{bmatrix}$$

Converting these scattering matrices to the transmission matrices and then using the method presented in Section 5.2.1, loss of the lossy material was calculated as $\alpha = 5.32$ $\frac{\text{dB}}{\text{mm}}$. The error in the value of the extracted loss is 7.4 %. One of the sources of error for this particular extraction method is the Gaussian beam assumption for the output of the horn antennas, which is valid by approximation. The other parameter contributing to the error is the finite cross section of the sample holder in the xy plane. The amount of error in the extracted loss calculated here is less than that presented in [135] for the 220 to 330 GHz frequency range (It should be mentioned that the materials characterized in [135] are low-loss compared to the materials considered here, so higher tolerance in extracted loss is to be expected).

Examining the presented method for measuring the loss of a material by more simulations would be of value. However, due to the high resource requirements in this simulation further studies could not be included here (the presented simulation for a single frequency required 389 GB of memory and 69 hours to complete).

5.2.3 Test Sample

Lactose $C_{12}H_{22}O_{11}$, abundant in the milk of most mammals, is an important disaccharide used in many food and pharmaceutical applications [130]. Two anomers of lactose (α-lactose and β-lactose) commonly exist in disaccharide powder. Fig. 5.10(a) shows the molecular structures of these anomers and Fig. 5.10(b) shows their absorption signatures in the THz gap. The evaluation and control of the ratio of these anomers is important when using lactose in food and drugs because these anomers show significantly different physiochemical properties [130]. The THz signatures of these anomers have been used to determine the ratio of each anomer within a mixture.

The absorption signatures of lactose anomers at the THz frequency range has been investigated in the literature [130, 141–143]. In [130], lactose powder was compressed to form pellets with a diameter of 6 mm and the thickness of 0.7 mm for spectroscopy testing. As shown in Fig. 5.10(b) from [130], α-lactose has two absorption peaks at 532 GHz and 1.37 THz, and β-lactose has one absorption peak at 1.19 THz.

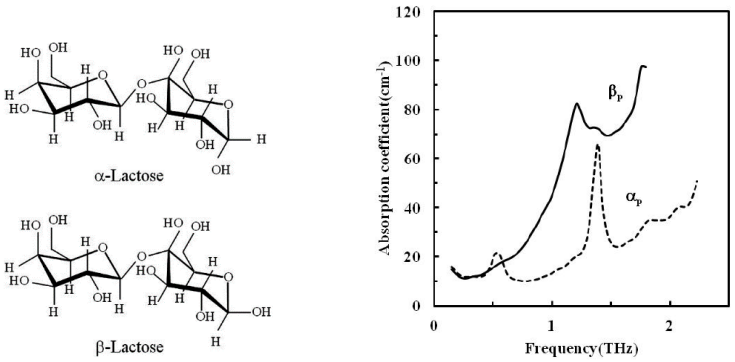

(a) (b)

Figure 5.10: (a) Molecular structures of lactose anomers [130], (b) Absorption coefficient of lactose anomers [130].

In [141], a high-resolution tunable frequency multiplication method was used to study the α-lactose signature around 532 GHz. It was shown that the signature occurs at 532 ($\pm$ 1) GHz with a 24 ($\pm$ 1) GHz linewidth.

In this research, α-lactose powder was used as a test sample, since it has an absorption signature around 520 to 545 GHz—the frequency range for which THz frequency extenders and horn antennas are available (for free space measurement), and for which the proposed dielectric waveguides were designed. In addition, the same test sample has been used in the literature when investigating the performance of metallic waveguides for THz absorption spectroscopy (as reviewed in Section 5.1.2). Apparently the concepts studied are scalable to any other frequency ranges within the THz gap, wherein other materials exhibit absorption signatures.

5.2.4 Measurement; Setup and Results

In this section, the measurement setup and results of the free space THz absorption spectroscopy of the test material sample are presented. The signal generated by a Network Analyzer was upconverted to the 500 to 750 GHz frequency range using frequency extender modules. The output of these modules are rectangular waveguides, $WR_{1.5}$, and were connected to horn antennas. The aperture diameter of the horn antenna is 2.4 mm, and it has gain of 25 dB, Fig. 5.11(a). Fig 5.11(b) shows the measurement setup.

In order to quantify the strength of the lactose signature versus its concentration in a mixture, it was mixed with polyethylene powder with different weight ratios. Polyethylene

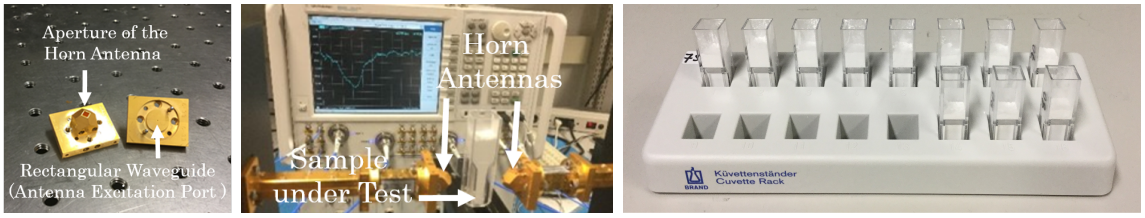

(a) (b) (c)

Figure 5.11: (a) Diagonal horn antennas for 500 to 750 GHz; (b) measurement setup used for the free space THz absorption spectroscopy; (c) mixtures of lactose/PE with different concentrations.

is very low loss in the THz range (less than 0.1 $\frac{\text{dB}}{\text{mm}}$ for frequencies up to 600 GHz [1]). Very fine polyethylene powder from Micro Powders Inc. (with mean particle size of 4.25 to 4.75 μm) was used as a secondary compound for the experiments. A digital weight with an accuracy of 0.1 mg was used to measure the different weights of lactose and polyethylene, which were then mixed manually. Fig. 5.11(c) shows the lactose/polyethylene mixtures, prepared with different concentrations. The total weight of the powder mixture is 1 g in all prepared samples.

Figure 5.12(a) shows the extracted absorption of the samples versus frequency for different concentrations. As shown in this figure, the absorption peak of the powder (at 532 GHz) increases with the concentration, and the maximum absorption value is around 12 $\frac{\text{dB}}{\text{mm}}$ for pure lactose powder (100 % concentration).

For a repeatability check, the same measurement was performed independently three times. Fig. 5.12(b) shows the absorption value at 532 GHz versus concentration for each of these three experiments. As shown in this figure, the extracted absorption is almost a linear function of the concentration. The absorption values of the three independent tests are closer to each other for higher concentrations; this could be explained by the fact that for higher concentrations, the absorption of the mixture is less affected by inconsistent mixing of the powders (lactose and polyethylene) are not mixed properly. These graphs verify that the uncompressed lactose powder shows the same absorption when the measurement is repeated, when keeping the details of the measurement the same. It should be mentioned that the size of the lactose powder particles are small enough compared to the THz wavelength (less than $\frac{\lambda}{50}$) to be considered as a homogeneous medium.

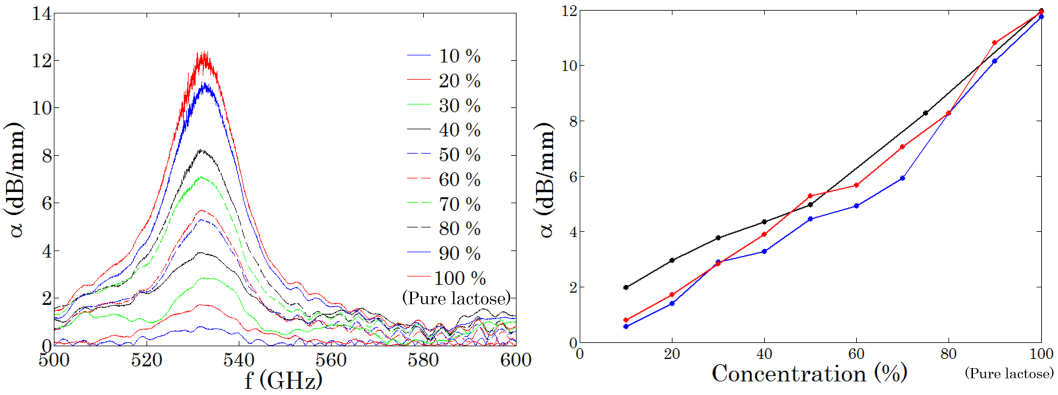

(a) (b)

Figure 5.12: (a) Absorption of lactose/polyethylene mixture versus frequency for different concentrations; (b) Absorption of lactose/polyethylene mixture at 532 GHz versus concentration, for three independent experiments.

5.3 THz Dielectric Waveguides for Absorption Spectroscopy

THz spectroscopy methods were presented in Section 5.1. In that section, waveguide-based THz spectroscopy methods and their advantages over the free space conventional setup were discussed as well. To date, single wire waveguides, microstrip lines, parallel plate waveguides, and coplanar waveguides have all been used for waveguide-based THz absorption spectroscopy [129, 131–134]. In this section, the application of a THz dielectric waveguides for waveguide-based spectroscopy is proposed. THz dielectric waveguides based on HR-Si are very low loss compared to existing metallic waveguides, especially at higher frequencies in the THz gap; therefore, for absorption spectroscopy applications, a very long waveguide of this type could be used to achieve a long interaction length. Using long interaction lengths in waveguide-based absorption spectroscopy, would enable weak absorption signatures to be captured as well as stronger signatures. Considering sensing applications, longer interaction lengths would result in higher sensitivity in detection of a target material. Moreover, advanced fabrication facilities are now available for silicon-based devices which assures the feasibility of fabricating THz dielectric waveguides with complex structures. In addition, as presented in Section 1.3, there has been significant advancements made in integrating solid-state THz sources with dielectric waveguides. Therefore, dielectric waveguides are promising candidates for fully integrated THz spectroscopy systems.

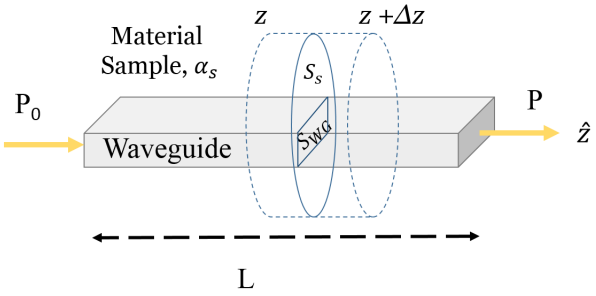

Figure 5.13: (a) Electromagnetic wave passing through a waveguide which is immersed in a lossy material sample.

5.3.1 Interaction Factor

In the waveguide-based absorption spectroscopy setup, a waveguide is immersed in a lossy material under test, as shown in Fig. 5.13. In this method, not all of the modal power interacts with the material sample, since a part of the modal field is confined inside the waveguide and only the part of the field which is outside of the guiding region passes through the sample. For a waveguide immersed in a lossy material [144]:

$$P = P_0 e^{-(\alpha_{WG} + \Gamma \alpha_s)L} \tag{5.17}$$

in which: P_0 is the input power of the electromagnetic wave, P is the output power, α_{WG} is the loss of the waveguide, α_s is the absorption coefficient of the lossy material surrounding the waveguide, L is the length of the waveguide and lossy material, and Γ is the interaction factor denoting the interaction between the waveguide mode and the lossy material.

The interaction factor depends on the cross section of the waveguide and the modal field distribution. In [145], a formulation for the interaction factor is presented where an electromagnetic wave passes through a periodic structure in free space. Although the same formulation has been used for waveguide-based setups in some cases in the literature, [146, 147], it will be shown in this section that this form of the factor is not sufficiently accurate for waveguide-based cases. In this section, the Poyntings theorem is used to derive the interaction factor in a waveguide-based setup.

Without loss of generality, consider a free standing dielectric channel waveguide, shown in Fig. 5.13. The waveguide is assumed to be immersed in a lossy material sample. The Poyntings theorem is applied to a cylindrical region V, enclosed by the surface S. Based on Poyntings theorem:

$$P_s = P_e + \overline{P}_d + j2\omega(\overline{W}_m - \overline{W}_e) \tag{5.18}$$

where, P_s is the complex power supplied by the sources inside V and P_e is the complex power exiting volume V:

$$P_e = \frac{1}{2}\int_S (\boldsymbol{E} \times \boldsymbol{H}^*) \cdot \hat{\boldsymbol{n}} dS \tag{5.19}$$

$\overline{P}_d$ is the time average dissipated power:

$$\overline{P}_d = \frac{1}{2}\int_V \sigma \left|\boldsymbol{E}\right|^2 dV \tag{5.20}$$

$\overline{W}_e$ and $\overline{W}_m$ are the time averaged stored energies in the electric and magnetic fields. For the cylinder shown in Fig. 2, as there is no electromagnetic source inside the cylinder, $P_s = 0$. $\overline{W}_e$ and $\overline{W}_m$ are equal in a waveguide mode [148]. In this case, the Poyntings theorem will be simplified to:

$$P_e + \overline{P}_d = 0 \tag{5.21}$$

In general, the integration in Eq. 5.19 should be applied over all faces of the cylinder. Since in an ideal waveguide there is no radiation loss, the integration will be non-zero only on the circular disks.

$$\begin{aligned} P_e &= -\frac{1}{2} Re\left\{\int_{S,z+\Delta z} (\boldsymbol{E} \times \boldsymbol{H}^*) \cdot \hat{\boldsymbol{z}} dS - \int_{S,z} (\boldsymbol{E} \times \boldsymbol{H}^*) \cdot \hat{\boldsymbol{z}} dS\right\} \\ &= -P(z+\Delta z) + P(z) = -\Delta z \frac{dP(z)}{dz} \\ &= \Delta z \frac{d}{dz}\left\{\frac{1}{2} Re \int_S (\boldsymbol{E} \times \boldsymbol{H}^*) \cdot \hat{\boldsymbol{z}} dS\right\} = -\Delta z \alpha \frac{1}{2} Re \int_S (\boldsymbol{E} \times \boldsymbol{H}^*) \cdot \hat{\boldsymbol{z}} dS \end{aligned} \tag{5.22}$$

wherein $P(z)$ is the transmitted modal power passing through the cross section S at z, and is given by:

$$P(z) = P_0 e^{-\alpha z} \tag{5.23}$$

wherein α is the mode attenuation constant and P_0 is the input power. The dissipated power relation Eq. 5.20, can rewritten as:

$$\overline{P}_d = \frac{1}{2}\int_S \sigma \left|\boldsymbol{E}\right|^2 dS \int_0^{\Delta z} e^{-\alpha z} dz \tag{5.24}$$

$$\int_0^{\Delta z} e^{-\alpha z} dz = \frac{1 - e^{-\alpha \Delta z}}{\alpha} = \Delta z \quad \text{for} \quad \Delta z \to 0 \tag{5.25}$$

Also, the integration over cross section S can be divided into the integration over the cross section of the guiding region of the waveguide, S_{WG}, and the cross section of the material sample, S_s. Therefore:

$$\overline{P}_d = \Delta z \frac{1}{2} \int_S \sigma \left|\boldsymbol{E}\right|^2 dS = \Delta z \frac{1}{2} (\sigma_{WG} \int_{S_{WG}} \left|\boldsymbol{E}\right|^2 dS + \sigma_s \int_{S_s} \left|\boldsymbol{E}\right|^2 dS) \tag{5.26}$$

On the right hand side of Eq. 5.26, the first term is the loss of the guiding region of the waveguide, and the second term is the loss of the material sample. Using Eq. 5.21, 5.22, and 5.26, the mode attenuation constant will be:

$$\alpha = \sigma_{WG} \frac{\int_{S_{WG}} \left|\boldsymbol{E}\right|^2 dS}{Re \int_S (\boldsymbol{E} \times \boldsymbol{H}^*) \cdot \hat{\boldsymbol{z}} dS} + \sigma_s \frac{\int_{S_s} \left|\boldsymbol{E}\right|^2 dS}{Re \int_S (\boldsymbol{E} \times \boldsymbol{H}^*) \cdot \hat{\boldsymbol{z}} dS} \tag{5.27}$$

The power absorption coefficient of the material sample, α_s, is related to the complex relative permittivity as:

$$\alpha_s = 2k_0 Im \sqrt{\varepsilon'_{r_s} + j\varepsilon''_{r_s}} \tag{5.28}$$

If the material sample is very low loss, then:

$$\sqrt{\varepsilon'_{r_s} + j\varepsilon''_{r_s}} \approx \sqrt{\varepsilon'_{r_s}} (1 + j \frac{\varepsilon''_{r_s}}{2\varepsilon'_{r_s}}) \tag{5.29}$$

Therefore:

$$\sigma_s = \omega \varepsilon_0 \varepsilon''_{r_s} = \frac{\alpha_s}{\eta_s} \tag{5.30}$$

in which $\eta_s = \sqrt{\frac{\mu_s}{\varepsilon_s}}$ is the characteristic impedance of the material sample. Therefore:

$$\sigma_s \frac{\int_{S_s} \left|\boldsymbol{E}\right|^2 dS}{Re \int_S (\boldsymbol{E} \times \boldsymbol{H}^*) \cdot \hat{\boldsymbol{z}} dS} = \frac{\alpha_s}{\eta_s} \frac{\int_{S_s} \left|\boldsymbol{E}\right|^2 dS}{Re \int_S (\boldsymbol{E} \times \boldsymbol{H}^*) \cdot \hat{\boldsymbol{z}} dS} \tag{5.31}$$

Using Eq. 5.17, the interaction factor Γ will be:

$$\Gamma = \frac{1}{\eta_s} \frac{\int_{S_s} \left|\boldsymbol{E}\right|^2 dS}{Re \int_S (\boldsymbol{E} \times \boldsymbol{H}^*) \cdot \hat{\boldsymbol{z}} dS} \tag{5.32}$$

This relation can be converted to a more comprehensive form as follows. The total stored energy in the material sample per unit length along the waveguide (z-direction) is:

$$W = \frac{1}{2} \int_{S_s} \varepsilon_s \left|\boldsymbol{E}\right|^2 dS \tag{5.33}$$

The interaction factor in Eq. 5.22 can then be rewritten as:

$$\Gamma = \frac{1}{\eta_s \varepsilon_s} \frac{\frac{1}{2}\int_{S_s} \varepsilon_s \left|\boldsymbol{E}\right|^2 dS}{\frac{1}{2}\int_S \varepsilon \left|\boldsymbol{E}\right|^2 dS} \frac{\frac{1}{2}\int_S \varepsilon \left|\boldsymbol{E}\right|^2 dS}{\frac{1}{2} Re \int_S (\boldsymbol{E} \times \boldsymbol{H}^*) \cdot \hat{\boldsymbol{z}} dS} \tag{5.34}$$

In Eq. 5.34, the second fraction is the total average stored energy in the material sample divided by the total average stored energy in both the material sample and the guiding region of the waveguide, per unit length of propagation direction (z). This term can be defined as a filling factor, representing the percentage of the modal stored energy that is in the sample region.

$$f = \frac{\frac{1}{2}\int_{S_s} \varepsilon_s \left|\boldsymbol{E}\right|^2 dS}{\frac{1}{2}\int_S \varepsilon \left|\boldsymbol{E}\right|^2 dS} \tag{5.35}$$

This expression can also be expressed in terms of the waveguide energy velocity, which is defined as [148]:

$$v_{en} = \frac{P_z}{W} = \frac{\frac{1}{2} Re \int_S (\boldsymbol{E} \times \boldsymbol{H}^*) \cdot \hat{\boldsymbol{z}} dS}{\frac{1}{2}\int_S \varepsilon \left|\boldsymbol{E}\right|^2 dS} \tag{5.36}$$

Therefore Eq. 5.34 can be rewritten as:

$$\Gamma = \frac{1}{\eta_s \varepsilon_s} f \frac{1}{v_{en}} \tag{5.37}$$

Furthermore:

$$\frac{1}{\eta_s \varepsilon_s} = \frac{1}{\sqrt{\frac{\mu_s}{\varepsilon_s}} \varepsilon_s} = \frac{1}{\sqrt{\mu_s \varepsilon_s}} = v_s \tag{5.38}$$

where v_s is the speed of light in the sample material medium. Therefore Eq. 5.37 can be written in its most concise form as:

$$\Gamma = f \frac{v_s}{v_{en}} \tag{5.39}$$

In [145] a similar formula was derived, wherein the energy velocity, v_{en}, is replaced by the group velocity, v_g, for a periodic structure in free space. Although in some special cases (including a periodic structure) $v_g = v_{en}$ and therefore Eq. 5.39 and the expression derived in [145] become identical, the rigorous expression for the interaction factor for a waveguide is the one given in Eq. 5.39.

5.3.2 Interaction Factor of the Proposed THz Waveguides

Based on Eq. 5.17, ΓL is the multiplicand of the loss factor of the material sample. Therefore, increasing either the interaction factor Γ, or interaction length L would enhance the interaction between the waveguide mode and the lossy material surrounding the waveguide. The interaction length (L) is limited by the size of the device and also the SNR of the system; lower the loss of the waveguide a longer waveguide could be used for a predefined value of SNR. Therefore, to compare the performance of the different waveguides for absorption spectroscopy, their Γ factors and losses should be considered.

Table 5.1 provides a comparison of the interaction factors of the proposed SBQ channel, SBQ slot, and plasmonic slot waveguides, calculated at a frequency of 532 GHz using full wave simulations and the equations presented in the previous section. Although the Γ factor of the plasmonic waveguide is more than that of the SBQ channel waveguide by a factor of 28, and more than the SBQ slot waveguide by a factor of 7.4, it suffers from a high amount of loss (three orders of magnitude higher than the SBQ waveguides). However, it should be mentioned that the plasmonic waveguide could outperform the SBQ waveguides due to its high interaction factor, in the cases of an application where the interaction length cannot be increased due to the small amount of available material under test.

Based on the values shown in Table 5.1, the Γ-factor of the SBQ slot waveguide is higher than that of the SBQ channel by a factor of 3.89. According to the measurement results presented in the previous chapters for these waveguides, the loss of the SBQ slot waveguide is higher than that of the SBQ channel waveguide by a factor of 6. Therefore, despite its low Γ-factor, the SBQ channel waveguide outperforms the SBQ slot waveguide for absorption spectroscopy applications, due to its low loss characteristic.

Table 5.1: Γ and f factors of the Proposed THz Waveguides (at 532 GHz).

Waveguide Type	Filling Factor (f)	Interaction Factor (Γ)
SBQ Channel Waveguide	0.023	0.09
SBQ Slot Waveguide	0.1	0.35
Plasmonic Slot Waveguide	0.76	2.6

5.3.3 THz SBQ Waveguides for Absorption Spectroscopy

(A) SBQ Channel Waveguide

Figure 5.14(a) shows an SBQ channel waveguide ($w_0 = 180$ μm, $h = 100$ μm). The vector plot of the electric fields of the first two modes over the waveguide cross section are shown in Fig. 5.14(b) and (c), at 530 GHz. The first mode has E_x as the main component of the electric field (E_x-mode), while the second mode is an E_y-mode. The propagation constants of the first two modes are shown in Fig. 5.14(d). The cutoff frequencies of these modes are 411 and 462 GHz. The Γ-factors of these modes were calculated using equations presented in Section 5.3.1 in HFSS simulation and are shown versus frequency in Fig. 5.14(e). As the frequency increases, the modal field distribution becomes more confined inside the guiding channel (HR-Si region); therefore, a decrease in the Γ-factor is expected, as shown in Fig. 5.14(d). The second mode has a higher Γ-factor compacted to first mode.

An SBQ channel waveguide with a sample holder was fabricated. Its schematic is shown in Fig. 5.15(a) (the sample holder for powder samples is etched in silicon with dimensions of $w \times L = 5 \times 8$ mm). There are two tapered-channel waveguides on each end of the waveguide as the transitions between the dielectric and metallic waveguides. The measurement setup is shown in Fig. 5.15(b). The dimensions of the $WR_{1.5}$ cross section are 381 by 191 μm. Having the long side of the $WR_{1.5}$ cross section in the x-direction, makes the manual alignment of the tapered channel waveguide to the center of the $WR_{1.5}$ challenging. The dimension of the short side of the $WR_{1.5}$, 191 μm, is close to the width of the SBQ waveguide, $w_0 = 180$ μm, so its alignment would be easier when this side is in the x-direction. The described arrangement for $WR_{1.5}$ would result in the excitation of the first mode of the dielectric waveguide (E_x). Although the first mode has a lower Γ-factor compared to the second mode [shown in Fig. 5.14(d)], for better alignment purpose, the first mode was used in the measurements.

Figure 5.15(c) shows S_{21} measured for three cases: no material sample, sample holder filled by 20 mg of lactose powder, and sample holder filled by 20 mg of polyethylene powder. The waveguide was cleaned after the lactose measurement and then used for the polyethylene measurement. As shown in this figure, the S_{21} result for the polyethylene case is very similar to that of the no material sample case; the reason being that polyethylene is a very low-loss powder with low permittivity value in the frequency range of interest. The S_{21} result for the lactose powder case shows a clear dip around 532 GHz, the absorption signature of this powder.

Polyethylene was used as the reference material sample to extract the loss of lactose, using a method similar to that used in the free space measurements, in Section 5.2.1. It

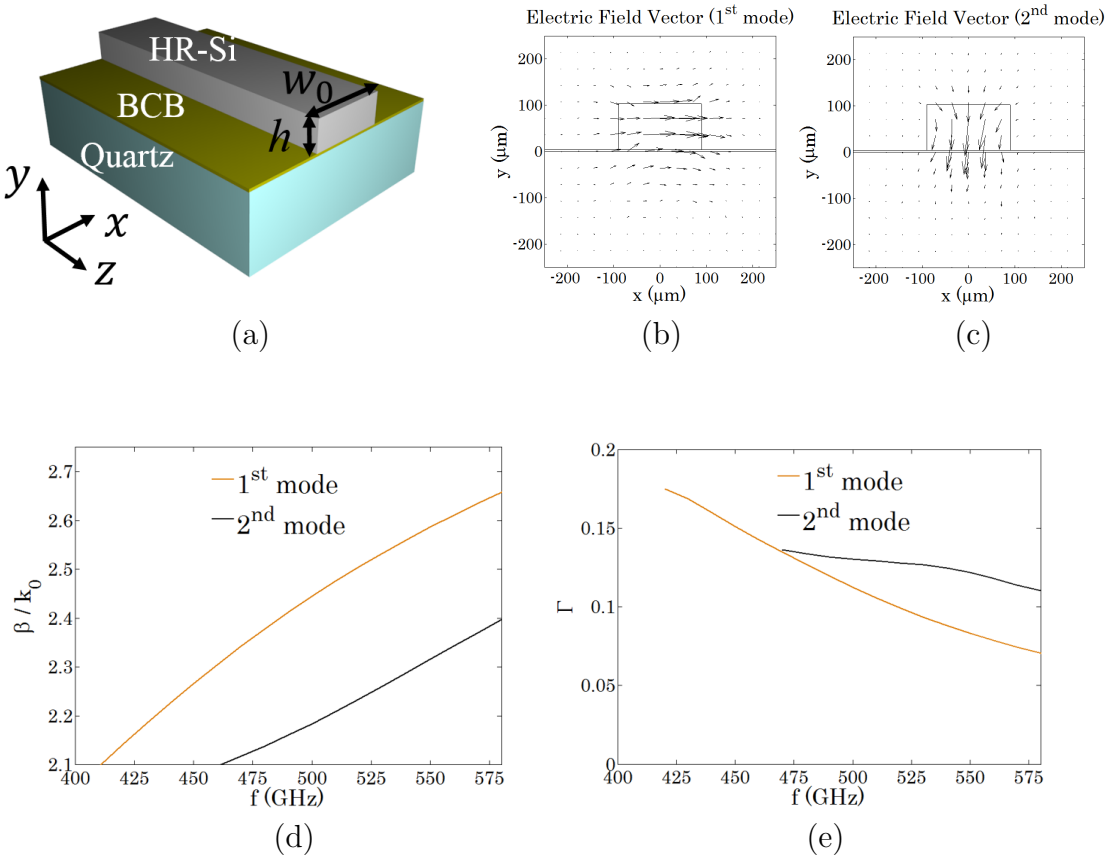

Figure 5.14: (a) SBQ channel waveguide, $w_0 = 180$ μm, $h = 100$ μm. (b) and (c) are the simulation results for the electric field vector plot over the cross section of the waveguide, for the first and second modes, respectively. (d) Simulation results for the normalized propagation constant for the first two modes of the waveguide (k_0 is the free space wavenumber). (e) Simulation results for Γ-factor versus frequency for the first two modes of the waveguide.

can be described as follows. Suppose that the transmission matrix measured between the $WR_{1.5}$ ports for the lactose and polyethylene cases are $\mathbf{T}$ and $\mathbf{T_0}$ respectively. Then:

$$\mathbf{T} = \mathbf{T_T T_m T_R} \tag{5.40}$$

$$\mathbf{T_0} = \mathbf{T_T T_{m0} T_R} \tag{5.41}$$

in which, $\mathbf{T_T}$ is the transmission matrix from the $WR_{1.5}$ port to the SBQ waveguide mode, at the location of the beginning of the sample holder. $\mathbf{T_R}$ is the transmission matrix from

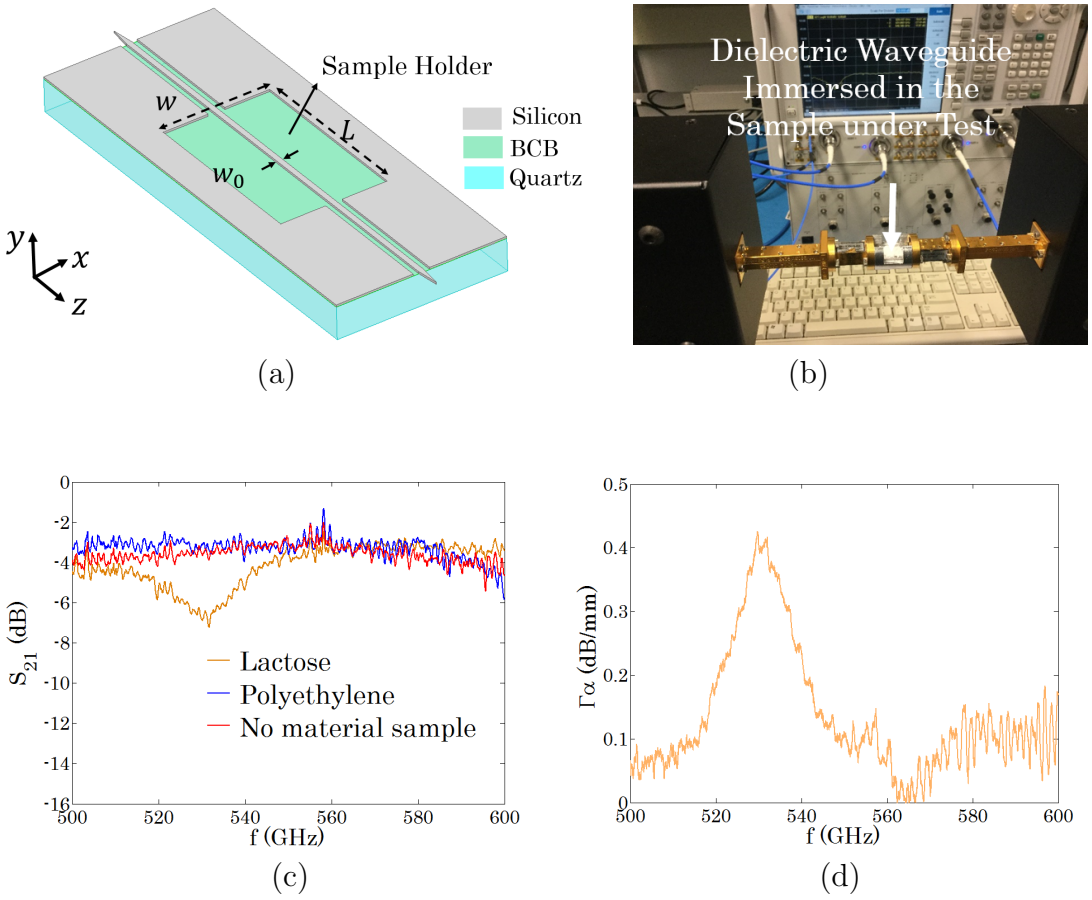

Figure 5.15: (a) SBQ channel waveguide, with sample holder and tapers at both ends for efficient coupling from/to $WR_{1.5}$ waveguide ($w_0 = 180$ μm, $L = 8$ mm, $w = 5$ mm, silicon thickness = 100 μm). (b) Waveguide-based THz absorption spectroscopy setup. (c) Measured S_{21} for three cases: no material sample inside the sample holder, polyethylene, and lactose. (d) Extracted $\Gamma\alpha$ from the measurements.

the SBQ waveguide mode, at the location of the end the sample holder, to the other $WR_{1.5}$ port. For powders with the same real parts of permittivity, $\mathbf{T_T}$ and $\mathbf{T_R}$ would be the same. Then:

$$\mathbf{T T_0^{-1}} = \mathbf{T_T T_m T_R T_R^{-1} T_{m0}^{-1} T_T^{-1}} = \mathbf{T_T T_m T_{m0}^{-1} T_T^{-1}} \tag{5.42}$$

Using Eq. 5.17:

$$\mathbf{T_m T_{m0}^{-1}} = \begin{bmatrix} e^{-L(\frac{\Gamma\alpha+\alpha_{WG}}{2}-\frac{\Gamma\alpha_0+\alpha_{WG}}{2})}e^{-j(\beta-\beta_0)L} & 0 \\ 0 & e^{L(\frac{\Gamma\alpha+\alpha_{WG}}{2}-\frac{\Gamma\alpha_0+\alpha_{WG}}{2})}e^{j(\beta-\beta_0)L} \end{bmatrix} \tag{5.43}$$

in which β and β_0 are the propagation constants of the SBQ waveguide mode when immersed in lactose and polyethylene respectively. α_{WG} is the attenuation constant of the SBQ waveguide mode. α and α_0 are the absorption factors of lactose and polyethylene powders respectively. Based on Eq. 5.42, $\mathbf{T_m T_{m0}^{-1}}$ and $\mathbf{T T_0^{-1}}$ have the same eigenvalues. $\mathbf{T}$ and $\mathbf{T_0}$ are measured matrices, so the eigenvalues of $\mathbf{T T_0^{-1}}$, and subsequently the eigenvalues of $\mathbf{T_m T_{m0}^{-1}}$, are known from two measurements. The real parts of the eigenvalues of $\mathbf{T_m T_{m0}^{-1}}$ are $\pm L(\frac{\Gamma\alpha+\alpha_{WG}}{2}-\frac{\Gamma\alpha_0+\alpha_{WG}}{2}) = \pm L\Gamma\frac{\alpha}{2}$, when the absorption of polyethylene is ignored compared to that of lactose. Therefore, from the two measurements, $L\Gamma\frac{\alpha}{2}$ can be calculated, which is linearly proportional to the absorption factor of lactose. For the known interaction length, $L = 8$ mm, $\Gamma\alpha$ is plotted in Fig. 5.15(d).

(B) SBQ Narrowed Channel Waveguide

From dielectric waveguide theory, it is known that reducing the width of a channel waveguide increases the cutoff frequency; therefore, for a fixed frequency, a higher amount of the modal field will be outside of the guiding region. The width of the SBQ channel waveguide, w_0 in Fig. 5.14(a), was swept in simulation and its cutoff frequency and interaction factor (Γ) are plotted in Fig. 5.16. As shown in Fig. 5.16(a), for a smaller width of channel waveguide, the cutoff frequency of both modes would be higher. Fig. 5.16(b) shows how the Γ-factor is higher for a smaller w_0. For a w_0 reduced to 140 μm from its initial value of 180 μm, Γ-factor increases by a factor of 1.94, and the cutoff frequency increases to 485 GHz from its initial value of 411 GHz [shown in Fig. 5.14(c)].

A tapered channel waveguide was also fabricated. Its schematic is shown in Fig. 5.17(a). The width of the channel waveguide outside of the sample holder is $w_1 = 180$ μm for better coupling from the $WR_{1.5}$ waveguide to the SBQ channel waveguide. The width of the waveguide tapers down to $w_0 = 140$ μm inside the sample holder over a taper length of $L_t = 1$ mm. The sample holder dimensions are $w \times L = 5 \times 8$ mm, the same as for the previous case. Fig. 5.17(b) shows the S_{21} for the sample holder filled by lactose powder. In this figure, for comparison, the S_{21} of the straight waveguide's lactose powder measurement is repeated from Fig. 5.15(c). S_{21} for $w_0 = 140$ μm is noisy for frequencies below 520 GHz, however, that is not the case for $w_0 = 180$ μm. This could be due to an increase in the cutoff frequency of the SBQ waveguide mode for a narrower width, w_0 (Simulation results

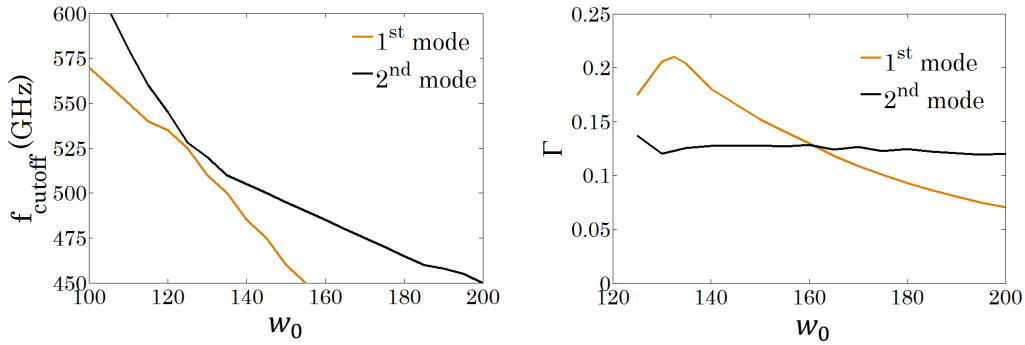

Figure 5.16: Cutoff frequency (a), and Γ-factor at 530 GHz (b), for the first two modes of the SBQ channel waveguide versus channel width (simulations).

for the cutoff frequencies in $w_0 = 140$ μm and $w_0 = 140$ μm are 485 GHz and 415 GHz, respectively).

Figure 5.17(c) shows the extracted absorption of lactose powder for both cases [using polyethylene as the reference material and using the matrix calculation presented for the straight SBQ waveguide, in Section (A)]. Again, the noisy result for $w_0 = 140$ μm at frequencies below 520 GHz could be explained based on the waveguide's cutoff frequency.

Figure 5.17(d) shows the division of the two plots of Fig. 5.17(c), $\frac{\Gamma(w_0=140\mu m)}{\Gamma(w_0=180\mu m)}$. In the same figure, simulation results of the same quantity are plotted as well. Simulations were performed for two different assumptions for the permittivity of the cladding region, $\varepsilon_r = 1$ and 3.7 (ε_r of the compressed lactose is below 3.7 for the frequencies up to 1.8 THz [149]; therefore, it is expected that the ε_r of the powder used in the experiments in this thesis falls within the 1 to 3.7 range). The significant fluctuations in the measurement results presented in this figure are due to the noisy results for the $w_0 = 140$ μm case, as can be seen in Fig. 5.17(b) and (c).

Although the average of the measurement results is quite close to the simulation results, to reduce the error of this measurement, a longer interaction length should be used (interaction length in the performed measurement was $L = 8$ mm). For a more accurate verification of the Γ-factor plot in Fig. 5.16(b), several channel SBQ waveguides with other width values, e.g. $w_0 = 150$, 160 μm, should be fabricated and measured. These steps towards more accurate experimental verification of the Γ factor are part of the future work of this research.

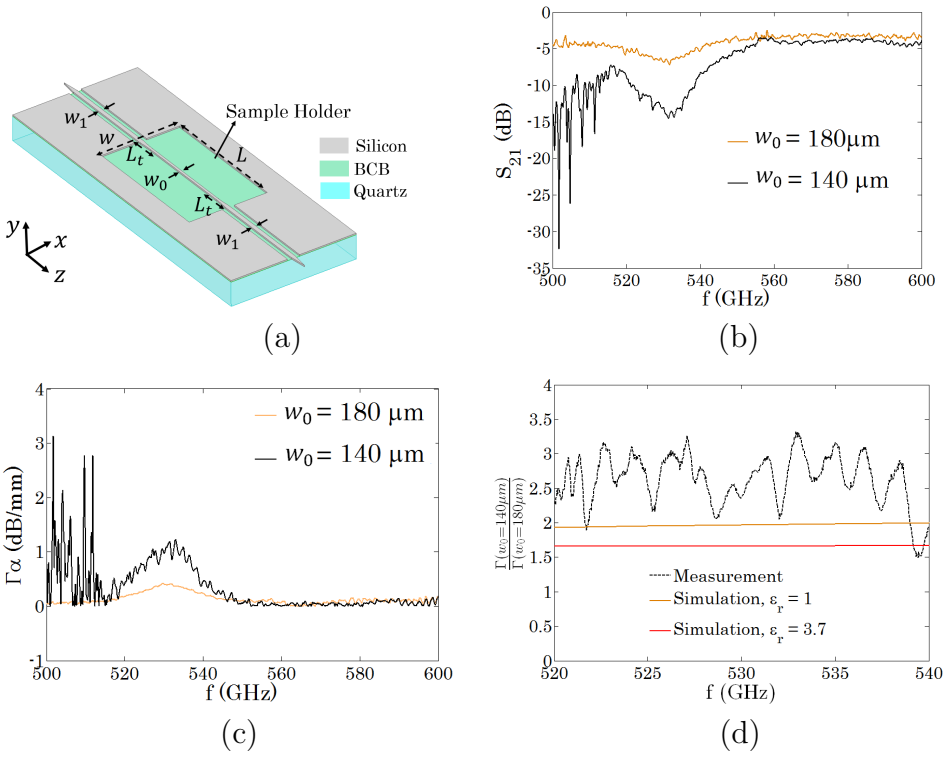

Figure 5.17: (a) Tapered SBQ channel waveguide ($w_1 = 180$ μm, $L = 8$ mm, $w = 5$ mm, $w_0 = 140$ μm, L_t= 1 mm, silicon thickness = 100 μm). (b) Measured S_{21} for lactose powder. (c) Extracted $\Gamma\alpha$ from the measurement. (d) Interaction factor of the SBQ channel waveguide, with the width of $w_0 = 140$ μm, divided by that of the SBQ channel waveguide with the width of $w_0 = 180$ μm; measurement and simulation results.

(C) Spiral SBQ Channel Waveguide

As derived in Section 5.3.1, the interaction between the material sample and a waveguide mode increases not only by Γ-factor, but also by the interaction length. The interaction length, L, is limited by two factors: 1) the SNR of the system (greater waveguide length increases the losses and results in a lower loss SNR), and 2) size of the device. A spiral shaped waveguide, Fig. 5.18(a), could be used to avoid a very long device, however, it comes with the cost of added bend losses. A spiral waveguide with a total length of 29.6 mm was fabricated, with the schematic shown in Fig. 5.18(a). The measurement setup is shown in Fig. 5.18(b). The amount of lactose and polyethylene powders used for this measurements was increased compared to previous measurements proportional to the

increase in the volume of the sample holder (42 mg). Fig. 5.18(c) shows S_{21} measured for the spiral waveguide immersed in the lactose powder. The S_{21} value at frequencies above 550 GHz, far from lactose's signature, is about 5 dB lower compared to that using the straight and tapered waveguides. Since lactose is low-loss in this frequency range, this drop in S_{21} is due to the increase in the waveguide loss because of the increase in its length, and also radiation losses in the bends.

The absorption of lactose was extracted using polyethylene as the reference material and shown in Fig. 5.18(d). $\Gamma\alpha$ is slightly higher for the spiral waveguide compared to that of the straight channel waveguide, with the same width, $w_0 = 180$ μm. This is expected, because in the bend regions of the spiral waveguide, the amount of modal field outside of the guiding channel increases; therefore, Γ factor would be higher for the bend regions compared to the straight waveguide. In Fig. 5.18(e), $\Gamma\alpha L$ is shown.

A spiral waveguide with the channel widths tapered down to 140 μm and 150 μm (from its initial value of 180 μm) were also fabricated and tested. Fig. 5.18(f) shows the $\Gamma\alpha L$ factor for all three spiral waveguides ($w_2 = 140$, 150, and 180 μm). For $w_2 = 140$ μm, the signal is noisy for frequencies below 540 GHz, compared to Fig. 5.17 (c), for which the signal is noisy for frequencies below 520 GHz. This could be explained by the added radiation loss of the bends and higher waveguide loss due to increased length. For $w_2 = 150$ μm, the signal is less noisy compared to the case of $w_2 = 140$ μm, which is expected for a wider channel width.

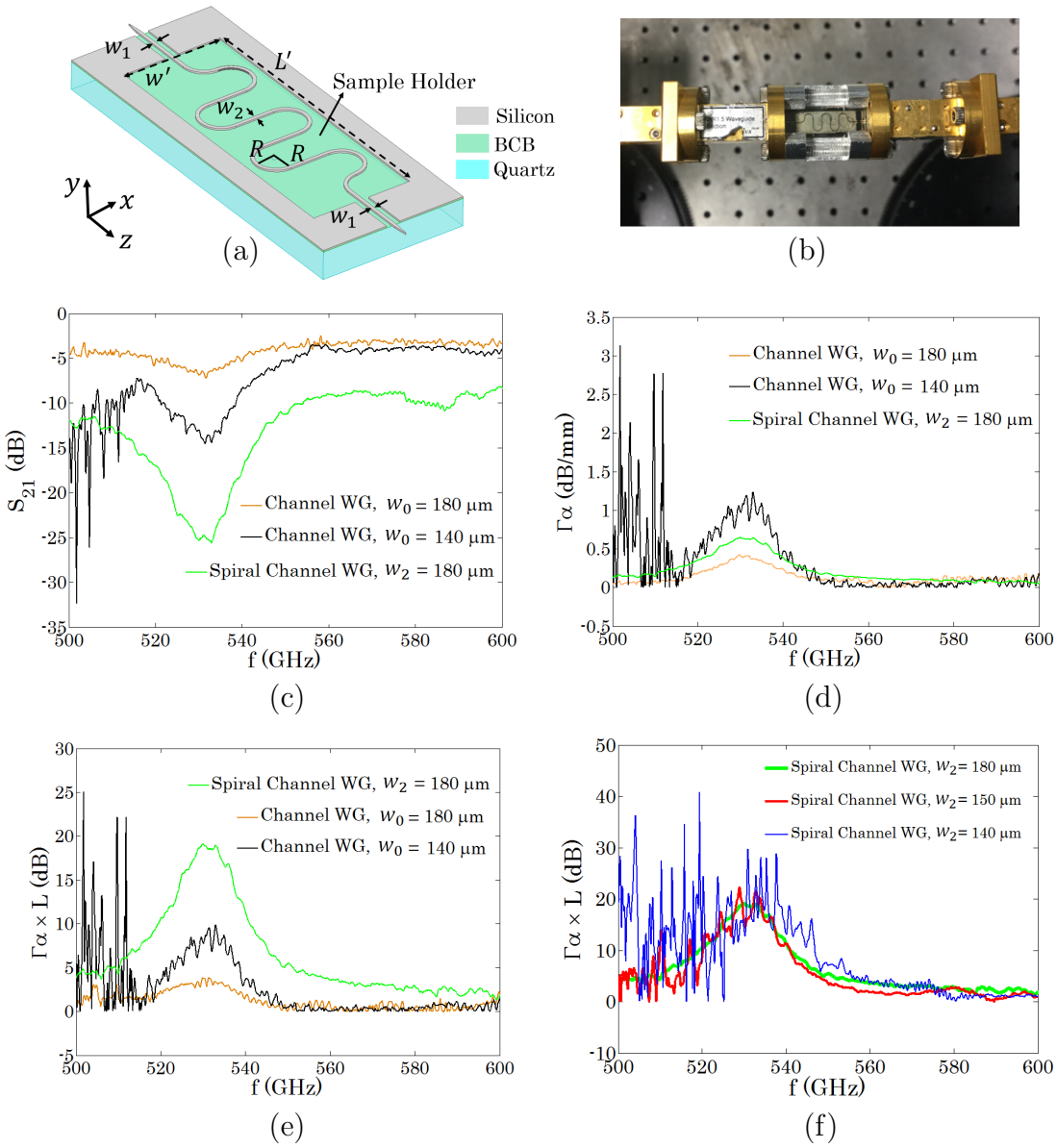

Figure 5.18: (a) Long spiral channel waveguide, total length of the waveguide inside the sample holder is 29.6 mm (w_1 = 180 μm, $L^{'}$ = 15.1 mm, $w^{'}$ = 5.54 mm, w_2 = 180 μm. All bends have angle of 90° and radius of R = 1 mm, silicon thickness is 100 μm). (b) Measurement setup. (c) Measured S_{21} when the sample holder is filled by lactose powder. (d) Extracted $\Gamma\alpha$ from the measurement. (e) Extracted $\Gamma\alpha \times$ Ł from the measurement. (f) Extracted $\Gamma\alpha$Ł from the measurement for spiral waveguides with widths of w_2 = 140, 150, and 180 μm.

5.4 Conclusions

5.4.1 Dielectric versus Metallic Waveguides: Performance Comparison

In this chapter, the application of THz dielectric waveguides for THz absorption spectroscopy has been proposed and investigated experimentally using SBQ platform. There have been several metallic waveguides used for the same application presented in the literature, as were reviewed in Section 5.1.2: parallel plate waveguides, single wire waveguides, microstrip lines, and coplanar waveguides. In each of these case studies, lactose powder was used as the test sample, but different methods for exposing the waveguide to this powder were used (In the single wire waveguide case, the powder was dispersed over the waveguide. In the microstrip line case, the powder was compressed and then cut into a cubic shape. In the coplanar waveguide case, the powder was dissolved in water. In the dielectric waveguide case, as presented in this thesis, the waveguides was immersed in the powder). Since the strength of the absorption signature of the powder depends on the sample preparation method, final results of these case studies can not be compared directly. However, a comparison based on the characteristics of each waveguide is presented here.

Single wire and parallel plate waveguides, although they have the greatest modal field in free space and high interaction between the waveguide mode and sample, are not easy to integrate with a source and detector. Moreover, parallel plate waveguides are closed waveguides so mounting the sample is more challenging than the other waveguides considered here, all of which are open waveguides.

Microstrip line and coplanar waveguides, shown in Fig. 5.19(a) and (b), are both planar open waveguides and integrable with a source and detector. The interaction factor (Γ), derived in Section 5.3.1, was calculated for these waveguides using HFSS simulation in the 500 to 550 GHz frequency range. It is presented in Fig. 5.19(e). The parameters and dimensions used for these waveguides in the simulations were extracted from [131] and [134], which proposed these waveguides for THz absorption spectroscopy applications. As shown in Fig. 5.19(e), the interaction factor of an SBQ channel waveguide is in between of that of a microstrip line and coplanar waveguide. The SBQ slot waveguide has the highest interaction factor among the examined waveguides.

Although microstrip lines and coplanar waveguides have interaction factors in the same range as those of the SBQ waveguides, these metallic waveguides suffer from high losses. In Table 5.2, the measured losses for each of these waveguides in the 500 to 570 GHz frequency range are shown. In addition, the value of the interaction factor at 530 GHz for each of

these waveguides is shown in the table. The high losses of these metallic waveguides limit the interaction length in absorption spectroscopy applications. Based on the values given in this table, the dielectric waveguides outperform the metallic waveguides, mainly due to their low-loss characteristic.

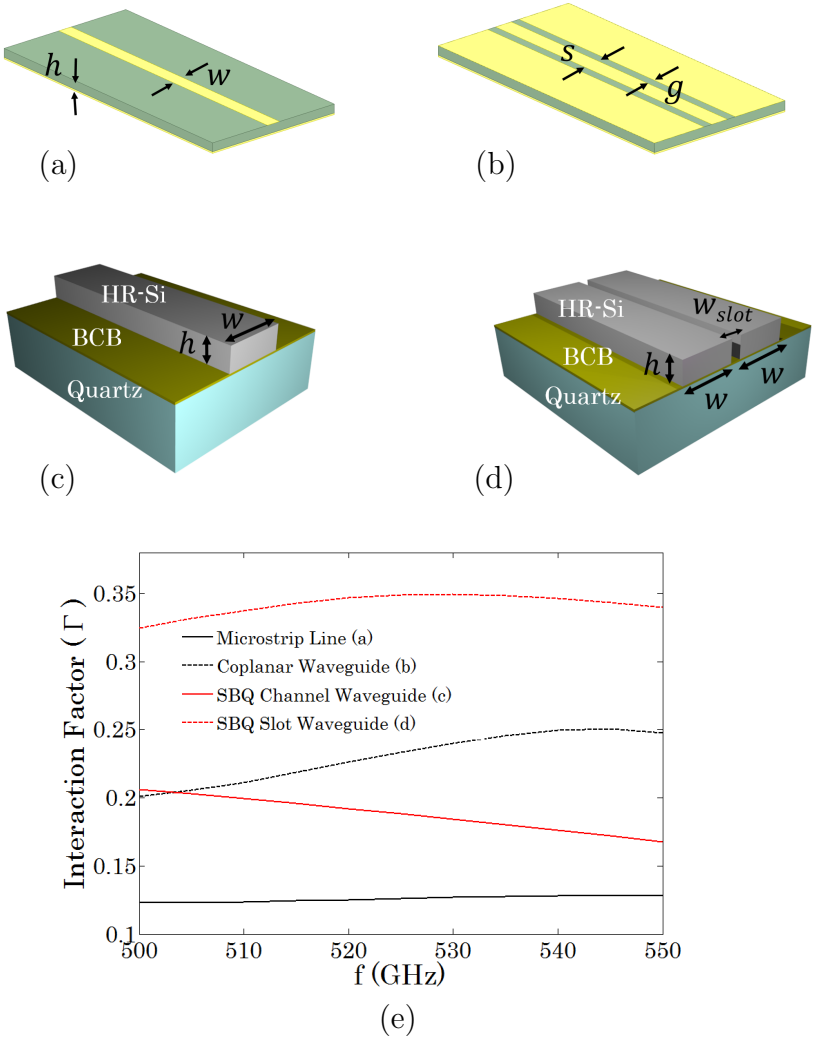

Figure 5.19: (a) Microstrip line, $w = 30$ μm, $h = 6$ μm [131], (b) Coplanar waveguide, $s = 20$ μm, $g = 10$ μm [134], (c) SBQ channel waveguide, $w = 140$ μm, $h = 100$ μm, (d) SBQ slot waveguide, $w_{slot} = 20$ μm, $w = 120$ μm, $h = 100$ μm, (e) Interaction factor for the waveguides shown in (a) to (d).

Table 5.2: Performance of THz waveguides for absorption spectroscopy

Waveguide Type	Loss ($\frac{dB}{mm}$)	Interaction Factor (Γ)
Microstrip line	> 3 [32]	0.13
Coplanar waveguide	> 4.2 [31, 134]	0.24
SBQ channel waveguide	0.046 (Chapter 3)	0.18
SBQ slot waveguide	0.16 (Chapter 4)	0.35

5.4.2 Sensitivity Estimation

Sensing of the concentration of a target material in a mixture based on sensing the changes in the mixture permittivity can be performed through sensing the changes in its real part or imaginary part (absorption). For sensing based on the real part of permittivity, various resonators with very high quality factor (Q-factor) have been used (such as whispering gallery mode resonator). A change in the permittivity of the mixture results in a shift in the very high-Q resonance. Although this method of sensing is very sensitive, it is not highly selective; since real part of the permittivity can be changed by many parameters not only the concentration of the target material. In contrast, sensing based on the absorption of the mixture when the target material has a frequency signature inside the measurement frequency range is a highly selective sensing method. Detecting an absorption peak at the frequency of the target material signature is an indicator of the presence of that material, and, strength of the absorption peak compared to the absorption value at frequencies far from the signature frequency is an indicator of the concentration of the target material.

To calculate the detection limit of concentration sensing of a material with an absorption signature in the THz gap using SBQ dielectric waveguide, several system parameters should be known: waveguide loss, sensitivity of the detector, dynamic range of the system, and the absorption peak of the target material. Using the measurement results for the SBQ channel waveguide immersed in the lactose powder and the system characteristics of the THz frequency extenders from Virginia Diodes Inc, this detection limit was calculated as following:

The parameters given in Table 5.3 were assumed for the calculations. The first three parameters are based on the parameters of the frequency extender modules from Virginia Diodes Inc. Parameters 4 to 7 are based on measurement results of the SBQ channel

waveguide presented in Chapter 3. Parameter 8 is from the measurement result of an SBQ channel waveguide immersed in lactose powder as was shown in Fig. 5.15(d). Consider a waveguide with a length of L contains N half-circle bends. Assume that S_{21}^{C} is the drop in the signal from the source to the detector when the waveguide is immersed in the sample. The sample is a mixture of a target material and a low-loss host material, and the concentration of the target material in the mixture is C. Then, using the parameters given in Table 5.3:

$$S_{21}^{C} = -(L - 1.5N\pi)0.05 - 0.75N - 2 - 0.41CL \quad \text{(dB)} \tag{5.44}$$

Defining C_{min} as the minimum detectable concentration, and C_{max} as the maximum concentration for which received signal will be above the noise floor, then:

$$S_{21}^{C_{min}} - S_{21}^{0} = -0.5 \quad \text{dB} \tag{5.45}$$

$$S_{21}^{C_{max}} = -100 \quad \text{dB} \tag{5.46}$$

An SBQ channel waveguide with a length of $L = 1$ m can be packed in a 5.4 cm by 5.4 cm area, as show schematically in Fig. 5.20, in which, there are $N = 18$ half-circle bends with radii of 1.5 mm. Substituting these values in Eq. 5.45 and Eq. 5.46, C_{min} and C_{max} would be 0.12 % and 9.5 %, respectively. As another example, an SBQ waveguide with a length of $L = 1.5$ m can be packed in a 6.7 cm by 6.7 cm area, in which, there are $N = 22$ half-circle bends with radius of 1.5 mm. Then, by substituting these values in Eq. 5.45 and Eq. 5.46, C_{min} and C_{max} would be 0.081 % (or 810 ppm) and 1.9 %. The interaction

Table 5.3: System parameters for sensitivity limits calculations

1. Source power	-25 dBm
2. System dynamic range	100 dB
3. Minimum detectable signal change	0.5 dB
4. Source-waveguide coupling loss	1 dB
5. Waveguide-detector coupling loss	1 dB
6. Waveguide loss	0.05 $\frac{\text{dB}}{\text{mm}}$
7. Loss of a half-circle bend (radius = 1.5 mm)	0.75 dB
8. Loss of an SBQ channel waveguide immersed in lactose	0.41 $\frac{\text{dB}}{\text{mm}}$

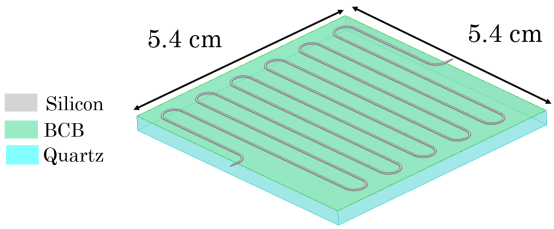

Figure 5.20: Schematic of an SBQ channel waveguide with total length of 1 m in a 5.4 cm $\times$ 5.4 cm area, using bends with radius of 1.5 mm.

factor in an SBQ channel waveguide increases by a factor of two when reducing its width from 180 μm to 140 μm, as was shown in the previous section in both simulation and measurement. Therefore, using the narrower waveguide, C_{min} reduces to 405 ppm.

It should be mentioned that in the presented calculations an increase in the interaction between the waveguide mode and the sample material in the bend sections compared to the straight sections of the waveguide has not been considered. The reason for not considering this effect in the calculations is that the measured value of the bending loss is available for a bend radius of $R = 1.5$ mm (which was presented in Chapter 3), but the measured effect of the bends in increasing the interaction is available for bend radius of $R = 1$ mm. Therefore, to consider the worst case, the mentioned effect is ignored in the presented calculations.

The mentioned sensitivity limits were calculated based on the strength of the signature at 532 GHz when an SBQ channel waveguide was immersed in the lactose powder, as measured and presented in the previous section. The minimum detectable concentration would be lower for a stronger signature, and would be higher for a weaker signature.

In terms of fabrication, the 5.4 cm by 5.4 cm and 6.7 cm by 6.7 cm devices can be fabricated using 4 inch wafers. The fabrication process presented for the SBQ platform is compatible with these large sizes. One challenge when fabricating such a large device is achieving a uniform coating of BCB in the bonding process, and a uniform photoresist in the optical lithography process.

It is worth mentioning that such long interaction lengths are impractical in a free space spectroscopy setup due to the huge amount of material under test required and the size of the setup. Also, it is impossible to achieve these long interaction lengths using a planar metallic waveguide, due to their high losses. However, by using a low-loss dielectric waveguide, a long interaction length is achievable in a few centimetres by few centimetres device.

Chapter 6

Conclusions and Future Work

6.1 Summary of Contributions

In this thesis, three new dielectric waveguide structures were been proposed and investigated theoretically and experimentally: a THz line–defect photonic crystal waveguide based on SOG (silicon-on-glass) technology, THz SBQ (silicon-BCB-quartz) waveguide, and a THz slot waveguide based on an SBQ platform. In addition, a new THz slot plasmonic waveguide based on doped-GaAs was investigated theoretically. Then, use of each of these waveguides within THz waveguide-based absorption spectroscopy was discussed and investigated theoretically. THz absorption spectroscopy was investigated experimentally based on the SBQ platform.

In Chapter 2, a novel THz line–defect photonic crystal waveguide based on SOG technology was proposed. The substrate in this waveguide is etched-pyrex, which has been bonded to the silicon guiding channel using anodic bonding. The design, fabrication, and measurement results for this waveguide were presented for the 500 to 700 GHz frequency range. The photonic crystal structure of the proposed waveguide provides a suspended platform via which other necessary components, such as resonators and couplers, can be integrated with the waveguide. Moreover, the presented structure has high mechanical stability and is scalable to other frequency ranges within the THz gap.

In Chapter 3, a new SBQ platform was proposed for THz low-loss integrated circuits, and a recipe for SBQ waveguide fabrication developed. Quartz is among the lowest-loss materials in the THz gap. However, it has a very different thermal expansion coefficient than HR-Si and; therefore, high temperature bonding processes, such as anodic boding,

are not applicable for bonding crystalline quartz and HR-Si. The bonding of the quartz substrate and silicon guiding channel was performed using a thin adhesive layer of BCB, at a lower temperature than is required by anodic bonding. The low thermal conductivity of the quartz and BCB created difficulties in achieving a photoresist mask for silicon etching. These fabrication challenges were resolved and fabrication and measurement results were presented. The measured average waveguide loss was as low as 0.026 $\frac{\text{dB}}{\lambda_0}$ for the fabricated SBQ samples, over the 500 to 580 GHz frequency range. A THz dielectric bend based on the SBQ platform was also fabricated and measured. In the presented SBQ structure, the quartz substrate provides a platform for other components to be integrated with the waveguide. The presented structure could easily be fabricated using basic cleanroom facilities. Through fabricated and measured samples, it was demonstrated that the new technology platform could be used to realize highly efficient and low-loss THz devices and systems.

In Chapter 4, two THz slot waveguides were investigated: a THz slot waveguide based on the SBQ platform, and a THz slot plasmonic waveguide using doped-GaAs. The deep-subwavelength mode sizes of these waveguides were studied, and compared ($\frac{\lambda_0}{6} \times \frac{\lambda_0}{28}$ and $\frac{\lambda_0}{19} \times \frac{\lambda_0}{19}$ for the SBQ slot waveguide and the plasmonic slot waveguide respectively, at 530 GHz). Fabrication and measurement results of the THz slot waveguide based on the SBQ platform for the 500 to 580 GHz frequency range was presented.

In Chapter 5, THz absorption spectroscopy based on dielectric waveguides was proposed and investigated. A free space measurement of a test sample (lactose powder) using a Network Analyzer and horn antennas was presented. Then, the interaction factor between a waveguide mode and a lossy material sample surrounding the waveguide was formulated. Several SBQ-based devices were fabricated and used within the waveguide-based absorption spectroscopy experiment. The performance of the dielectric waveguide within such an application was compared with that of metallic waveguides. The low-loss characteristics of the SBQ platform enables a very long interaction length between the waveguide mode and the sample (1 meter or more). The long interaction length opens the possibility of: compact and integrated waveguide-based THz spectroscopy for material characterization, and concentrations sensing of materials which have fingerprints within the THz gap. Through system calculations, it is shown that concentrations in the range of parts-per-million are detectable using such a long interaction length.

6.2 Outlook and Future

1. **Passive components based on the SBQ platform**: Several SBQ-based structures were investigated in this thesis (SBQ channel waveguide, SBQ bend, and SBQ

slot waveguide). Realizing compact THz systems based on the SBQ platform will require other passive components, such as couplers, power dividers, and resonators. The design and experimental study of these components would provide a deeper insight into SBQ-based THz systems.

2. **Measurement setup improvement**: One of the challenges of the measurement setup used for this thesis was inserting the taper of the dielectric waveguide into the rectangular waveguide (output of the frequency extender). Performing this step manually frequently resulted in the breakage of the waveguide taper. A motorized stage capable of scanning the position of the dielectric waveguide in three directions would improve the setup. Using such a setup would not only improve the safe insertion of the taper of the dielectric waveguide into the rectangular metallic waveguide, it would increase the accuracy of the waveguide.

3. **Integration of active components into the SBQ platform**: SBQ is a promising platform for hybrid integrated THz circuits that require a transition from a planar off-chip waveguide to a planar on-chip transmission line for active integration. One potential approach could be a transition between the SBQ dielectric waveguide and a short CPW trasnmission line and then a connection to the chip through the conventional flip-chip technique [150, 151]. These transitions have been studied at frequencies up to 200 GHz. The scaling of these transitions to the THz range is an area that needs to be explored further in the future.

4. **THz line–defect waveguide for THz sensing applications**: Highly sensitive devices based on photonic crystal structures have been studied in the optical range of frequencies. The slow wave characteristic of the THz line–defect waveguide close to its band-edge provides a possibility for realizing highly sensitive THz sensors based on this type of waveguide. Of particular relevance, this slow wave structure can provide an enhanced interaction factor for waveguide-based THz absorption spectroscopy.

5. **Improved characterization of the SBQ slot waveguide**: Two different lengths of the SBQ slot waveguide were used for characterizing this waveguide in this thesis. Due to the long transitions between the metallic rectangular waveguide and the SBQ slot waveguide in the test setup, and the fixed length of the metallic stages, the length difference between the two SBQ slot waveguides was quite short. It is suggested that future work be undertaken in which longer metallic stages are fabricated and a longer length difference is used between the two SBQ slot waveguides to characterize this type of waveguide more accurately.

6. **Waveguide-based absorption spectroscopy with long interaction length**: It was demonstrated that it is possible to use the SBQ low-loss platform for very long interaction length. Experimental verification of the ability to conduct absorption spectroscopy using a very long spiral SBQ waveguide would provide deeper insights into the operational characteristics and the performance of such structure and the resulting THz sensor.

References

[1] Y.-S. Lee, *Principles of terahertz science and technology.* Springer Science & Business Media, 2009, vol. 170.

[2] M. F. Kimmitt, "Restrahlen to t-rays–100 years of terahertz radiation," *Journal of Biological Physics*, vol. 29, no. 2, pp. 77–85, 2003.

[3] M. Leahy-Hoppa, M. Fitch, X. Zheng, L. Hayden, and R. Osiander, "Wideband terahertz spectroscopy of explosives," *Chemical Physics Letters*, vol. 434, no. 4, pp. 227–230, 2007.

[4] Y. Shen, a. T. Lo, P. Taday, B. Cole, W. Tribe, and M. Kemp, "Detection and identification of explosives using terahertz pulsed spectroscopic imaging," *Applied Physics Letters*, vol. 86, no. 24, p. 241116, 2005.

[5] A. G. Davies, A. D. Burnett, W. Fan, E. H. Linfield, and J. E. Cunningham, "Terahertz spectroscopy of explosives and drugs," *Materials Today*, vol. 11, no. 3, pp. 18–26, 2008.

[6] K. Yamamoto, M. Yamaguchi, F. Miyamaru, M. Tani, M. Hangyo, T. Ikeda, A. Matsushita, K. Koide, M. Tatsuno, and Y. Minami, "Noninvasive inspection of c-4 explosive in mails by terahertz time-domain spectroscopy," *Japanese Journal of Applied Physics*, vol. 43, no. 3B, p. L414, 2004.

[7] M. C. Kemp, P. Taday, B. E. Cole, J. Cluff, A. J. Fitzgerald, and W. R. Tribe, "Security applications of terahertz technology," in *Proc. SPIE*, vol. 5070, no. 6, 2003, pp. 44–52.

[8] Y. Hu, P. Huang, L. Guo, X. Wang, and C. Zhang, "Terahertz spectroscopic investigations of explosives," *Physics Letters A*, vol. 359, no. 6, pp. 728–732, 2006.

[9] R. H. Jacobsen, D. Mittleman, and M. Nuss, "Chemical recognition of gases and gas mixtures with terahertz waves," *Optics Letters*, vol. 21, no. 24, pp. 2011–2013, 1996.

[10] D. M. Mittleman, R. H. Jacobsen, R. Neelamani, R. G. Baraniuk, and M. C. Nuss, "Gas sensing using terahertz time-domain spectroscopy," *Applied Physics B: Lasers and Optics*, vol. 67, no. 3, pp. 379–390, 1998.

[11] C. F. Neese, I. R. Medvedev, G. M. Plummer, A. J. Frank, C. D. Ball, and F. C. De Lucia, "Compact submillimeter/terahertz gas sensor with efficient gas collection, preconcentration, and ppt sensitivity," *IEEE Sensors Journal*, vol. 12, no. 8, pp. 2565–2574, 2012.

[12] F. Hindle, A. Cuisset, R. Bocquet, and G. Mouret, "Continuous-wave terahertz by photomixing: applications to gas phase pollutant detection and quantification," *Comptes Rendus Physique*, vol. 9, no. 2, pp. 262–275, 2008.

[13] P.-X. Neumaier, K. Schmalz, J. Borngräber, R. Wylde, and H.-W. Hübers, "Terahertz gas-phase spectroscopy: chemometrics for security and medical applications," *Analyst*, vol. 140, no. 1, pp. 213–222, 2015.

[14] D. A. Crawley, C. Longbottom, B. E. Cole, C. M. Ciesla, D. Arnone, V. P. Wallace, and M. Pepper, "Terahertz pulse imaging: a pilot study of potential applications in dentistry," *Caries Research*, vol. 37, no. 5, pp. 352–359, 2003.

[15] D. Crawley, C. Longbottom, V. P. Wallace, B. Cole, D. Arnone, and M. Pepper, "Three-dimensional terahertz pulse imaging of dental tissue," *Journal of Biomedical Optics*, vol. 8, no. 2, pp. 303–307, 2003.

[16] C. M. Ciesla, D. D. Arnone, A. Corchia, D. Crawley, C. Longbottom, E. H. Linfield, and M. Pepper, "Biomedical applications of terahertz pulse imaging," in *Proc. SPIE*, vol. 3934, 2000, pp. 73–81.

[17] V. Wallace, A. Fitzgerald, S. Shankar, N. Flanagan, R. Pye, J. Cluff, and D. Arnone, "Terahertz pulsed imaging of basal cell carcinoma ex vivo and in vivo," *British Journal of Dermatology*, vol. 151, no. 2, pp. 424–432, 2004.

[18] A. J. Fitzgerald, V. P. Wallace, M. Jimenez-Linan, L. Bobrow, R. J. Pye, A. D. Purushotham, and D. D. Arnone, "Terahertz pulsed imaging of human breast tumors," *Radiology*, vol. 239, no. 2, pp. 533–540, 2006.

[19] R. M. Woodward, B. E. Cole, V. P. Wallace, R. J. Pye, D. D. Arnone, E. H. Linfield, and M. Pepper, "Terahertz pulse imaging in reflection geometry of human skin cancer and skin tissue," *Physics in Medicine and Biology*, vol. 47, no. 21, p. 3853, 2002.

[20] R. Woodward, V. Wallace, D. Arnone, E. Linfield, and M. Pepper, "Terahertz pulsed imaging of skin cancer in the time and frequency domain," *Journal of Biological Physics*, vol. 29, no. 2-3, pp. 257–259, 2003.

[21] C. Yu, S. Fan, Y. Sun, and E. Pickwell-MacPherson, "The potential of terahertz imaging for cancer diagnosis: A review of investigations to date," *Quantitative Imaging in Medicine and Surgery*, vol. 2, no. 1, p. 33, 2012.

[22] M. Tonouchi, "Cutting-edge terahertz technology," *Nature Photonics*, vol. 1, no. 2, pp. 97–105, 2007.

[23] G. Gallot, S. Jamison, R. McGowan, and D. Grischkowsky, "Terahertz waveguides," *JOSA B*, vol. 17, no. 5, pp. 851–863, 2000.

[24] P. Kirby, D. Pukala, H. Manohara, I. Mehdi, and J. Papapolymerou, "Characterization of micromachined silicon rectangular waveguide at 400 GHz," *IEEE Microwave and Wireless Components Letters*, vol. 16, no. 6, pp. 366–368, 2006.

[25] C. D. Nordquist, M. C. Wanke, A. M. Rowen, C. L. Arrington, A. D. Grine, and C. T. Fuller, "Properties of surface metal micromachined rectangular waveguide operating near 3 THz," *IEEE Journal of Selected Topics in Quantum Electronics*, vol. 17, no. 1, pp. 130–137, 2011.

[26] K. M. Leong, K. Hennig, C. Zhang, R. N. Elmadjian, Z. Zhou, B. S. Gorospe, P. P. Chang-Chien, V. Radisic, and W. R. Deal, "WR1. 5 silicon micromachined waveguide components and active circuit integration methodology," *IEEE Transactions on Microwave Theory and Techniques*, vol. 60, no. 4, pp. 998–1005, 2012.

[27] J. Hu, S. Xie, and Y. Zhang, "Micromachined terahertz rectangular waveguide bandpass filter on silicon-substrate," *IEEE Microwave and Wireless Components Letters*, vol. 22, no. 12, pp. 636–638, 2012.

[28] T. J. Reck, C. Jung-Kubiak, J. Gill, and G. Chattopadhyay, "Measurement of silicon micromachined waveguide components at 500–750 GHz," *IEEE Transactions on Terahertz Science and Technology*, vol. 4, no. 1, pp. 33–38, 2014.

[29] T. Reck, C. Jung-Kubiak, J. V. Siles, C. Lee, R. Lin, G. Chattopadhyay, I. Mehdi, and K. Cooper, "A silicon micromachined eight-pixel transceiver array for submillimeter-wave radar," *IEEE Transactions on Terahertz Science and Technology*, vol. 5, no. 2, pp. 197–206, 2015.

[30] C. Jung-Kubiak, T. J. Reck, J. V. Siles, R. Lin, C. Lee, J. Gill, K. Cooper, I. Mehdi, and G. Chattopadhyay, "A multistep DRIE process for complex terahertz waveguide components," *IEEE Transactions on Terahertz Science and Technology*, vol. 6, no. 5, pp. 690–695, 2016.

[31] M. Y. Frankel, S. Gupta, J. A. Valdmanis, and G. A. Mourou, "Terahertz attenuation and dispersion characteristics of coplanar transmission lines," *IEEE Transactions on Microwave Theory and Techniques*, vol. 39, no. 6, pp. 910–916, 1991.

[32] H.-M. Heiliger, M. Nagel, H. Roskos, H. Kurz, F. Schnieder, W. Heinrich, R. Hey, and K. Ploog, "Low-dispersion thin-film microstrip lines with cyclotene (benzocyclobutene) as dielectric medium," *Applied Physics Letters*, vol. 70, no. 17, pp. 2233–2235, 1997.

[33] R. Mendis and D. Grischkowsky, "THz interconnect with low-loss and low-group velocity dispersion," *IEEE Microwave and Wireless Components Letters*, vol. 11, no. 11, pp. 444–446, 2001.

[34] M. Ahmadi-Boroujeni, K. Altmann, B. Scherger, C. Jansen, M. Shahabadi, and M. Koch, "Terahertz parallel-plate ladder waveguide with highly confined guided modes," *IEEE Transactions on Terahertz Science and Technology*, vol. 3, no. 1, pp. 87–95, 2013.

[35] K. Wang and D. M. Mittleman, "Metal wires for terahertz wave guiding," *Nature*, vol. 432, no. 7015, pp. 376–379, 2004.

[36] T.-I. Jeon, J. Zhang, and D. Grischkowsky, "THz Sommerfeld wave propagation on a single metal wire," *Applied Physics Letters*, vol. 86, no. 16, p. 161904, 2005.

[37] A. G. Engel and L. P. Katehi, "Low-loss monolithic transmission lines for submillimeter and terahertz frequency applications," *IEEE Transactions on Microwave Theory and Techniques*, vol. 39, no. 11, pp. 1847–1854, 1991.

[38] N. Dib and L. P. Katehi, "Characterization of three-dimensional open dielectric structures using the finite-difference time-domain method," *IEEE Transactions on Microwave Theory and Techniques*, vol. 44, no. 4, pp. 513–518, 1996.

[39] N. Ranjkesh, M. Basha, A. Taeb, and S. Safavi-Naeini, "Silicon-on-glass dielectric waveguide, Part II: For THz applications," *IEEE Transactions on Terahertz Science and Technology*, vol. 5, no. 2, pp. 280–287, 2015.

[40] K. Tsuruda, M. Fujita, and T. Nagatsuma, "Extremely low-loss terahertz waveguide based on silicon photonic-crystal slab," *Optics Express*, vol. 23, no. 25, pp. 31 977–31 990, 2015.

[41] H.-T. Zhu, Q. Xue, J.-N. Hui, and S. W. Pang, "Design, fabrication, and measurement of the low-loss SOI-based dielectric microstrip line and its components," *IEEE Transactions on Terahertz Science and Technology*, vol. 6, no. 5, pp. 696–705, 2016.

[42] H. Amarloo and S. Safavi-Naeini, "Terahertz line-defect waveguide based on silicon-on-glass technology," *IEEE Transactions on Terahertz Science and Technology*, vol. 7, no. 4, pp. 433–439, 2017.

[43] N. Ranjkesh, "Si waveguide technology for high performance millimeter-wave/terahertz integrated systems," Ph.D. dissertation, University of Waterloo, 2015.

[44] A. Malekabadi, S. A. Charlebois, D. Deslandes, and F. Boone, "High-resistivity silicon dielectric ribbon waveguide for single-mode low-loss propagation at F/G-bands," *IEEE Transactions on Terahertz Science and Technology*, vol. 4, no. 4, pp. 447–453, 2014.

[45] N. Ranjkesh, M. Basha, A. Taeb, A. Zandieh, S. Gigoyan, and S. Safavi-Naeini, "Silicon-on-glass dielectric waveguide, Part I: For millimeter-wave integrated circuits," *IEEE Transactions on Terahertz Science and Technology*, vol. 5, no. 2, pp. 268–279, 2015.

[46] A. Cozma and B. Puers, "Characterization of the electrostatic bonding of silicon and pyrex glass," *Journal of Micromechanics and Microengineering*, vol. 5, no. 2, p. 98, 1995.

[47] K. B. Albaugh, P. E. Cade, and D. Rasmussen, "Mechanisms of anodic bonding of silicon to pyrex glass," in *Solid-State Sensor and Actuator Workshop, 1988. Technical Digest., IEEE.* IEEE, 1988, pp. 109–110.

[48] M. Naftaly and R. Miles, "Terahertz time-domain spectroscopy: A new tool for the study of glasses in the far infrared," *Journal of Non-crystalline Solids*, vol. 351, no. 40, pp. 3341–3346, 2005.

[49] G. Chattopadhyay, "Technology, capabilities, and performance of low power terahertz sources," *IEEE Transactions on Terahertz Science and Technology*, vol. 1, no. 1, pp. 33–53, 2011.

[50] J. Faist, F. Capasso, D. L. Sivco, C. Sirtori, A. L. Hutchinson, and A. Y. Cho, "Quantum cascade laser," *Science*, vol. 264, no. 5158, pp. 553–556, 1994.

[51] R. Köhler, A. Tredicucci, F. Beltram, H. E. Beere, E. H. Linfield, A. G. Davies, D. A. Ritchie, R. C. Iotti, and F. Rossi, "Terahertz semiconductor-heterostructure laser," *Nature*, vol. 417, no. 6885, pp. 156–159, 2002.

[52] G. Scalari, C. Walther, J. Faist, H. Beere, and D. Ritchie, "Electrically switchable, two-color quantum cascade laser emitting at 1.39 and 2.3thz," *Applied Physics Letters*, vol. 88, no. 14, p. 141102, 2006.

[53] G. Chattopadhyay, E. Schlecht, J. S. Ward, J. J. Gill, H. H. Javadi, F. Maiwald, and I. Mehdi, "An all-solid-state broad-band frequency multiplier chain at 1500 GHz," *IEEE Transactions on Microwave Theory and Techniques*, vol. 52, no. 5, pp. 1538–1547, 2004.

[54] J. D. Joannopoulos, S. G. Johnson, J. N. Winn, and R. D. Meade, *Photonic crystals: molding the flow of light*. Princeton University Press, 2011.

[55] S. G. Johnson, P. R. Villeneuve, S. Fan, and J. D. Joannopoulos, "Linear waveguides in photonic-crystal slabs," *Physical Review B*, vol. 62, no. 12, p. 8212, 2000.

[56] L. C. Andreani and M. Agio, "Intrinsic diffraction losses in photonic crystal waveguides with line defects," *Applied Physics Letters*, vol. 82, no. 13, pp. 2011–2013, 2003.

[57] C. Jamois, R. Wehrspohn, L. Andreani, C. Hermann, O. Hess, and U. Gösele, "Silicon-based two-dimensional photonic crystal waveguides," *Photonics and Nanostructures-Fundamentals and Applications*, vol. 1, no. 1, pp. 1–13, 2003.

[58] M. Lončar, D. Nedeljković, T. P. Pearsall, J. Vučković, A. Scherer, S. Kuchinsky, and D. C. Allan, "Experimental and theoretical confirmation of bloch-mode light propagation in planar photonic crystal waveguides," *Applied Physics Letters*, vol. 80, no. 10, pp. 1689–1691, 2002.

[59] J. Dai, J. Zhang, W. Zhang, and D. Grischkowsky, "Terahertz time-domain spectroscopy characterization of the far-infrared absorption and index of refraction of high-resistivity, float-zone silicon," *JOSA B*, vol. 21, no. 7, pp. 1379–1386, 2004.

[60] M. N. Afsar and K. J. Button, "Millimeter-wave dielectric measurement of materials," *Proceedings of the IEEE*, vol. 73, no. 1, pp. 131–153, 1985.

[61] P. H. Bolivar, M. Brucherseifer, J. G. Rivas, R. Gonzalo, I. Ederra, A. L. Reynolds, M. Holker, and P. de Maagt, "Measurement of the dielectric constant and loss tangent of high dielectric-constant materials at terahertz frequencies," *IEEE Transactions on Microwave Theory and Techniques*, vol. 51, no. 4, pp. 1062–1066, 2003.

[62] M. D. Janezic and J. A. Jargon, "Complex permittivity determination from propagation constant measurements," *IEEE Microwave and Guided Wave Letters*, vol. 9, no. 2, pp. 76–78, 1999.

[63] E. Tatar, M. Torunbalci, S. Alper, and T. Akin, "A method and electrical model for the anodic bonding of soi and glass wafers," in *Micro Electro Mechanical Systems (MEMS), 2012 IEEE 25th International Conference on.* IEEE, 2012, pp. 68–71.

[64] G. Wallis, "Field assisted glass sealing," *Active and Passive Electronic Components*, vol. 2, no. 1, pp. 45–53, 1975.

[65] T. Rogers and J. Kowal, "Selection of glass, anodic bonding conditions and material compatibility for silicon-glass capacitive sensors," *Sensors and Actuators A: Physical*, vol. 46, no. 1-3, pp. 113–120, 1995.

[66] D. Grischkowsky, S. Keiding, M. Van Exter, and C. Fattinger, "Far-infrared time-domain spectroscopy with terahertz beams of dielectrics and semiconductors," *JOSA B*, vol. 7, no. 10, pp. 2006–2015, 1990.

[67] F. Niklaus, G. Stemme, J.-Q. Lu, and R. Gutmann, "Adhesive wafer bonding," *Journal of Applied Physics*, vol. 99, no. 3, p. 2, 2006.

[68] S. Costanzo, I. Venneri, G. Di Massa, and A. Borgia, "Benzocyclobutene as substrate material for planar millimeter-wave structures: dielectric characterization and application," *Journal of Infrared, Millimeter, and Terahertz Waves*, vol. 31, no. 1, p. 66, 2010.

[69] M. C. Schaafsma, H. Starmans, A. Berrier, and J. G. Rivas, "Enhanced terahertz extinction of single plasmonic antennas with conically tapered waveguides," *New Journal of Physics*, vol. 15, no. 1, p. 015006, 2013.

[70] R. Degl'Innocenti, Y. D. Shah, R. Wallis, A. Klimont, Y. Ren, D. S. Jessop, H. E. Beere, and D. A. Ritchie, "A hybrid plasmonic waveguide terahertz quantum cascade laser," *Applied Physics Letters*, vol. 106, no. 8, p. 082101, 2015.

[71] H. Amarloo and S. Safavi-Naeini, "Slot plasmonic waveguide based on doped-GaAs for terahertz deep-subwavelength applications," *JOSA A*, vol. 32, no. 11, pp. 2189–2194, 2015.

[72] Z. Li, L. L. Wong, A. I. Chen, S. Na, J. Sun, and J. T. Yeow, "Fabrication of capacitive micromachined ultrasonic transducers based on adhesive wafer bonding technique," *Journal of Micromechanics and Microengineering*, vol. 26, no. 11, p. 115019, 2016.

[73] E. Perret, N. Zerounian, S. David, and F. Aniel, "Complex permittivity characterization of benzocyclobutene for terahertz applications," *Microelectronic Engineering*, vol. 85, no. 11, pp. 2276–2281, 2008.

[74] H. Amarloo, N. Ranjkesh, and S. A. Safavi-Naeini, "Terahertz silicon–BCB–quartz dielectric waveguide: an efficient platform for compact THz systems," *IEEE Transactions on Terahertz Science and Technology*, 2018.

[75] E. V. Loewenstein, D. R. Smith, and R. L. Morgan, "Optical constants of far infrared materials. 2: Crystalline solids," *Applied Optics*, vol. 12, no. 2, pp. 398–406, 1973.

[76] M. Despont, H. Gross, F. Arrouy, C. Stebler, and U. Staufer, "Fabrication of a silicon-pyrex-silicon stack by AC anodic bonding," *Sensors and Actuators A: Physical*, vol. 55, no. 2-3, pp. 219–224, 1996.

[77] T. Abe, K. Sunagawa, A. Uchiyama, K. Yoshizawa, and Y. Nakazato, "Fabrication and bonding strength of bonded silicon-quartz wafers," *Japanese Journal of Applied Physics*, vol. 32, no. 1S, p. 334, 1993.

[78] "http : //www.tydexoptics.com/materials," *TYDEX Research and Industrial Optics*.

[79] A. Sinha, H. Levinstein, and T. Smith, "Thermal Stresses and Cracking Resistance of Dielectric Films (SiN, Si_3N_4, and SiO_2) on Si Substrates," *Journal of applied physics*, vol. 49, no. 4, pp. 2423–2426, 1978.

[80] K. Sugii, H. Koizumi, and E. Kubota, "Precision lattice parameter measurements on doped indium phosphide single crystals," *Journal of Electronic Materials*, vol. 12, no. 4, pp. 701–712, 1983.

[81] R. Belford and S. Sood, "Surface activation using remote plasma for silicon to quartz wafer bonding," *Microsystem Technologies*, vol. 15, no. 3, pp. 407–412, 2009.

[82] A. Jourdain, P. De Moor, S. Pamidighantam, and H. Tilmans, "Investigation of the hermeticity of BCB-sealed cavities for housing (RF-) MEMS devices," in *Micro Electro Mechanical Systems, 2002. The Fifteenth IEEE International Conference on*. IEEE, 2002, pp. 677–680.

[83] T.-K. A. Chou and K. Najafi, "3D MEMS fabrication using low-temperature wafer bonding with benzocyclobutene (BCB)," in *Transducers 01 Eurosensors XV*. Springer, 2001, pp. 1542–1545.

[84] Z. Li, "Fabrication of capacitive micromachined ultrasonic transducers based on adhesive wafer bonding," Ph.D. dissertation, University of Waterloo, 2017.

[85] Z. Song, Z. Tan, L. Liu, and Z. Wang, "Void-free bcb adhesive wafer bonding with high alignment accuracy," *Microsystem Technologies*, vol. 21, no. 8, pp. 1633–1641, 2015.

[86] I. Christiaens, G. Roelkens, K. De Mesel, D. Van Thourhout, and R. Baets, "Thin-film devices fabricated with benzocyclobutene adhesive wafer bonding," *Journal of Lightwave Technology*, vol. 23, no. 2, p. 517, 2005.

[87] C. A. Barrios, K. B. Gylfason, B. Sánchez, A. Griol, H. Sohlström, M. Holgado, and R. Casquel, "Slot-waveguide biochemical sensor," *Optics Letters*, vol. 32, no. 21, pp. 3080–3082, 2007.

[88] C. A. Barrios, "Optical slot-waveguide based biochemical sensors," *Sensors*, vol. 9, no. 6, pp. 4751–4765, 2009.

[89] F. DellOlio and V. M. Passaro, "Optical sensing by optimized silicon slot waveguides," *Optics Express*, vol. 15, no. 8, pp. 4977–4993, 2007.

[90] M. Nagel, A. Marchewka, and H. Kurz, "Low-index discontinuity terahertz waveguides," *Optics Express*, vol. 14, no. 21, pp. 9944–9954, 2006.

[91] S. A. Maier, *Plasmonics: fundamentals and applications*. Springer Science & Business Media, 2007.

[92] J. Homola, S. S. Yee, and G. Gauglitz, "Surface plasmon resonance sensors: review," *Sensors and Actuators B: Chemical*, vol. 54, no. 1, pp. 3–15, 1999.

[93] M. Chamanzar, M. Soltani, B. Momeni, S. Yegnanarayanan, and A. Adibi, "Hybrid photonic surface-plasmon-polariton ring resonators for sensing applications," *Applied Physics B*, vol. 101, no. 1-2, pp. 263–271, 2010.

[94] J. Satija, N. S. Punjabi, V. Sai, and S. Mukherji, "Optimal design for U-bent fiber-optic LSPR sensor probes," *Plasmonics*, vol. 9, no. 2, pp. 251–260, 2014.

[95] P. L. Stiles, J. A. Dieringer, N. C. Shah, and R. P. Van Duyne, "Surface-enhanced raman spectroscopy," *Annu. Rev. Anal. Chem.*, vol. 1, pp. 601–626, 2008.

[96] A. G. Brolo, E. Arctander, R. Gordon, B. Leathem, and K. L. Kavanagh, "Nanohole-enhanced raman scattering," *Nano Letters*, vol. 4, no. 10, pp. 2015–2018, 2004.

[97] A. Ahmed and R. Gordon, "Single molecule directivity enhanced raman scattering using nanoantennas," *Nano Letters*, vol. 12, no. 5, pp. 2625–2630, 2012.

[98] D. Wang, W. Zhu, M. D. Best, J. P. Camden, and K. B. Crozier, "Directional raman scattering from single molecules in the feed gaps of optical antennas," *Nano Letters*, vol. 13, no. 5, pp. 2194–2198, 2013.

[99] E. J. Smythe, M. D. Dickey, J. Bao, G. M. Whitesides, and F. Capasso, "Optical antenna arrays on a fiber facet for in situ surface-enhanced raman scattering detection," *Nano Letters*, vol. 9, no. 3, pp. 1132–1138, 2009.

[100] V. J. Sorger, R. F. Oulton, R.-M. Ma, and X. Zhang, "Toward integrated plasmonic circuits," *MRS Bulletin*, vol. 37, no. 08, pp. 728–738, 2012.

[101] D. Dai and S. He, "A silicon-based hybrid plasmonic waveguide with a metal cap for a nano-scale light confinement," *Optics Express*, vol. 17, no. 19, pp. 16 646–16 653, 2009.

[102] J. Varsanik and J. Bernstein, "Integrated optic/nanofluidic fluorescent detection device with plasmonic excitation," *Journal of Micromechanics and Microengineering*, vol. 23, no. 9, p. 095017, 2013.

[103] M. Février, P. Gogol, A. Aassime, R. Mégy, C. Delacour, A. Chelnokov, A. Apuzzo, S. Blaize, J.-M. Lourtioz, and B. Dagens, "Giant coupling effect between metal nanoparticle chain and optical waveguide," *Nano Letters*, vol. 12, no. 2, pp. 1032–1037, 2012.

[104] B. Desiatov, I. Goykhman, and U. Levy, "Plasmonic nanofocusing of light in an integrated silicon photonics platform," *Optics Express*, vol. 19, no. 14, pp. 13 150–13 157, 2011.

[105] R. M. Dickson and L. A. Lyon, "Unidirectional plasmon propagation in metallic nanowires," *The Journal of Physical Chemistry B*, vol. 104, no. 26, pp. 6095–6098, 2000.

[106] S. A. Maier, P. G. Kik, and H. A. Atwater, "Optical pulse propagation in metal nanoparticle chain waveguides," *Physical Review B*, vol. 67, no. 20, p. 205402, 2003.

[107] B. Guo, G. Song, and L. Chen, "Numerical study of sub-wavelength plasmonic waveguide," *Optics Communications*, vol. 281, no. 5, pp. 1123–1128, 2008.

[108] S. I. Bozhevolnyi, V. S. Volkov, E. Devaux, J.-Y. Laluet, and T. W. Ebbesen, "Channel plasmon subwavelength waveguide components including interferometers and ring resonators," *Nature*, vol. 440, no. 7083, pp. 508–511, 2006.

[109] H. Amarloo, M. Neshat, and S. Safavi-Naeini, "Terahertz plasmonic-like waveguide for integrated sensing applications," *Electronics Letters*, vol. 49, no. 13, pp. 836–838, 2013.

[110] G. Veronis and S. Fan, "Modes of subwavelength plasmonic slot waveguides," *Journal of Lightwave Technology*, vol. 25, no. 9, pp. 2511–2521, 2007.

[111] ——, "Guided subwavelength plasmonic mode supported by a slot in a thin metal film," *Optics Letters*, vol. 30, no. 24, pp. 3359–3361, 2005.

[112] J. S. Ahn, T. Kang, D. K. Singh, Y.-M. Bahk, H. Lee, S. B. Choi, and D.-S. Kim, "Optical field enhancement of nanometer-sized gaps at near-infrared frequencies," *Optics Express*, vol. 23, no. 4, pp. 4897–4907, 2015.

[113] A. Berrier, R. Ulbricht, M. Bonn, and J. G. Rivas, "Ultrafast active control of localized surface plasmon resonances in silicon bowtie antennas," *Optics Express*, vol. 18, no. 22, pp. 23 226–23 235, 2010.

[114] A. Berrier, P. Albella, M. A. Poyli, R. Ulbricht, M. Bonn, J. Aizpurua, and J. G. Rivas, "Detection of deep-subwavelength dielectric layers at terahertz frequencies using semiconductor plasmonic resonators," *Optics Express*, vol. 20, no. 5, pp. 5052–5060, 2012.

[115] J. Jung and T. G. Pedersen, "Analysis of plasmonic properties of heavily doped semiconductors using full band structure calculations," *Journal of Applied Physics*, vol. 113, no. 11, p. 114904, 2013.

[116] G. Garcia, R. Buonsanti, E. L. Runnerstrom, R. J. Mendelsberg, A. Llordes, A. Anders, T. J. Richardson, and D. J. Milliron, "Dynamically modulating the surface plasmon resonance of doped semiconductor nanocrystals," *Nano Letters*, vol. 11, no. 10, pp. 4415–4420, 2011.

[117] J. G. Rivas, M. Kuttge, P. H. Bolivar, H. Kurz, and J. Sánchez-Gil, "Propagation of surface plasmon polaritons on semiconductor gratings," *Physical Review Letters*, vol. 93, no. 25, p. 256804, 2004.

[118] M. Kuttge, H. Kurz, J. G. Rivas, J. Sánchez-Gil, and P. H. Bolivar, "Analysis of the propagation of terahertz surface plasmon polaritons on semiconductor groove gratings," *Journal of Applied Physics*, vol. 101, no. 2, p. 023707, 2007.

[119] M. C. Schaafsma and J. G. Rivas, "Semiconductor plasmonic crystals: active control of thz extinction," *Semiconductor Science and Technology*, vol. 28, no. 12, p. 124003, 2013.

[120] S. Adachi, *Handbook on Physical Properties of Semiconductors*, ser. Handbook on Physical Properties of Semiconductors. Kluwer Academic Publishers, 2004, no. v. 2.

[121] N. W. Ashcroft, N. D. Mermin, and S. Rodriguez, *Solid state physicsy.* American Association of Physics Teachers, 1998.

[122] C. Hilsum, "Simple empirical relationship between mobility and carrier concentration," *Electronics Letters*, vol. 10, no. 13, pp. 259–260, 1974.

[123] B. Stuart, *Biological applications of infrared spectroscopy.* John Wiley & Sons, 2008.

[124] N. Nagai, R. Kumazawa, and R. Fukasawa, "Direct evidence of inter-molecular vibrations by THz spectroscopy," *Chemical Physics Letters*, vol. 413, no. 4, pp. 495–500, 2005.

[125] P. F. Taday, I. Bradley, D. Arnone, and M. Pepper, "Using terahertz pulse spectroscopy to study the crystalline structure of a drug: A case study of the polymorphs of ranitidine hydrochloride," *Journal of Pharmaceutical Sciences*, vol. 92, no. 4, pp. 831–838, 2003.

[126] D. J. Cook, B. K. Decker, and M. G. Allen, "Quantitative THz spectroscopy of explosive materials," in *Optical Terahertz Science and Technology.* Optical Society of America, 2005, p. MA6.

[127] H.-B. Liu, Y. Chen, G. J. Bastiaans, and X.-C. Zhang, "Detection and identification of explosive RDX by THz diffuse reflection spectroscopy," *Optics Express*, vol. 14, no. 1, pp. 415–423, 2006.

[128] N. Palka, "THz reflection spectroscopy of explosives measured by time domain spectroscopy," *Acta Physica Polonica A*, vol. 120, no. 4, pp. 713–715, 2011.

[129] M. Walther, M. R. Freeman, and F. A. Hegmann, "Metal-wire terahertz time-domain spectroscopy," *Applied Physics Letters*, vol. 87, no. 26, p. 261107, 2005.

[130] S. Yamauchi, S. Hatakeyam, Y. Imai, and M. Tonouchi, "Terahertz time-domain spectroscopy to identify and evaluate anomer in lactose," *American Journal of Analytical Chemistry*, vol. 4, no. 12, p. 756, 2013.

[131] M. Byrne, J. Cunningham, K. Tych, A. Burnett, M. Stringer, C. Wood, L. Dazhang, M. Lachab, E. Linfield, and A. Davies, "Terahertz vibrational absorption spectroscopy using microstrip-line waveguides," *Applied Physics Letters*, vol. 93, no. 18, p. 182904, 2008.

[132] S. H. Srikantaiah, "Engineering metal parallel plate waveguides as a 2-D plane for high resolution THz time domain spectroscopy," Ph.D. dissertation, Oklahoma State University, 2011.

[133] M. Theuer and J. S. Melinger, "High resolution waveguide terahertz time-domain spectroscopy," *Journal of Infrared, Millimeter, and Terahertz Waves*, vol. 32, no. 11, pp. 1267–1284, 2011.

[134] M. Kumar, "The development of on-Chip THz time-domain spectroscopy," Ph.D. dissertation, University of Leeds, 2016.

[135] T. Tosaka, K. Fujii, K. Fukunaga, and A. Kasamatsu, "Development of complex relative permittivity measurement system based on free-space in 220–330-GHz range," *IEEE Transactions on Terahertz science and Technology*, vol. 5, no. 1, pp. 102–109, 2015.

[136] J. Hammler, A. J. Gallant, and C. Balocco, "Free-space permittivity measurement at terahertz frequencies with a vector network analyzer," *IEEE Transactions on Terahertz Science and Technology*, vol. 6, no. 6, pp. 817–823, 2016.

[137] M. C. Teich and B. Saleh, "Fundamentals of photonics," *Canada, Wiley Interscience*, vol. 3, 1991.

[138] S. Withington and J. A. Murphy, "Analysis of diagonal horns through gaussian-hermite modes," *IEEE Transactions on Antennas and Propagation*, vol. 40, no. 2, pp. 198–206, 1992.

[139] J. F. Johansson and N. D. Whyborn, "The diagonal horn as a sub-millimeter wave antenna," *IEEE Transactions on Microwave Theory and Techniques*, vol. 40, no. 5, pp. 795–800, 1992.

[140] P. D. Cunningham, N. N. Valdes, F. A. Vallejo, L. M. Hayden, B. Polishak, X.-H. Zhou, J. Luo, A. K.-Y. Jen, J. C. Williams, and R. J. Twieg, "Broadband terahertz characterization of the refractive index and absorption of some important polymeric and organic electro-optic materials," *Journal of Applied Physics*, vol. 109, no. 4, pp. 043 505–043 505, 2011.

[141] E. Brown, J. Bjarnason, A. Fedor, and T. Korter, "On the strong and narrow absorption signature in lactose at 0.53 THz," *Applied Physics Letters*, vol. 90, no. 6, p. 061908, 2007.

[142] G. M. Png, B. M. Fischer, D. Appadoo, R. Plathe, and D. Abbott, "Double-layered nitrocellulose membrane sample holding technique for THz and FIR spectroscopic measurements," *Optics Express*, vol. 23, no. 4, pp. 4997–5013, 2015.

[143] Y. Kawada, T. Yasuda, A. Nakanishi, K. Akiyama, and H. Takahashi, "Single-shot terahertz spectroscopy using pulse-front tilting of an ultra-short probe pulse," *Optics Express*, vol. 19, no. 12, pp. 11 228–11 235, 2011.

[144] A. Nitkowski, L. Chen, and M. Lipson, "Cavity-enhanced on-chip absorption spectroscopy using microring resonators," *Optics Express*, vol. 16, no. 16, pp. 11 930–11 936, 2008.

[145] N. A. Mortensen and S. Xiao, "Slow-light enhancement of beer-lambert-bouguer absorption," *Applied Physics Letters*, vol. 90, no. 14, p. 141108, 2007.

[146] W.-C. Lai, S. Chakravarty, X. Wang, C. Lin, and R. T. Chen, "On-chip methane sensing by near-IR absorption signatures in a photonic crystal slot waveguide," *Optics Letters*, vol. 36, no. 6, pp. 984–986, 2011.

[147] Y. Zou, S. Chakravarty, P. Wray, and R. T. Chen, "Mid-infrared holey and slotted photonic crystal waveguides in silicon-on-sapphire for chemical warfare simulant detection," *Sensors and Actuators B: Chemical*, vol. 221, pp. 1094–1103, 2015.

[148] S. J. Orfanidis, *Electromagnetic waves and antennas*. Rutgers University New Brunswick, NJ, 2002.

[149] A. Roggenbuck, H. Schmitz, A. Deninger, I. C. Mayorga, J. Hemberger, R. Güsten, and M. Grüninger, "Coherent broadband continuous-wave terahertz spectroscopy on solid-state samples," *New Journal of Physics*, vol. 12, no. 4, p. 043017, 2010.

[150] H.-C. Lu, C.-C. Kuo, P.-A. Lin, C.-F. Tai, Y.-L. Chang, Y.-S. Jiang, J.-H. Tsai, Y.-M. Hsin, and H. Wang, "Flip-chip-assembled W-band CMOS chip modules on ceramic integrated passive device with transition compensation for millimeter-wave system-in-package integration," *IEEE Transactions on Microwave Theory and Techniques*, vol. 60, no. 3, pp. 766–777, 2012.

[151] B. Yu, Y. Liu, Y. Ye, X. Liu, and Q. J. Gu, "Low-loss and broadband g-band dielectric interconnect for chip-to-chip communication," *IEEE Microwave and Wireless Components Letters*, vol. 26, no. 7, pp. 478–480, 2016.